

# Magnetism and metal-organic self-assembly of rare-earth atoms on decoupling layers

Présentée le 30 juin 2022

Faculté des sciences de base  
IPHYS - Gestion  
Programme doctoral en physique

pour l'obtention du grade de Docteur ès Sciences

par

**Sébastien REYNAUD**

Acceptée sur proposition du jury

Prof. O. Yazyev, président du jury  
Prof. H. Brune, Dr M. Pivetta, directeurs de thèse  
Prof. J. Barth, rapporteur  
Dr A. Barla, rapporteur  
Prof. H. Dil, rapporteur



# Acknowledgements

First, I want to thank Harald Brune for the opportunity of working in his group. I learned a lot from my time in LNS, thank you. I also want to express my deep gratitude to Marina Pivetta, who spent so much time patiently guiding me during these four years. I sincerely appreciated.

I would like to thank Alessandro Barla, Hugo Dil, Johannes Barth and Oleg Yazyev for serving as jury members at my oral exam.

Many thanks also go to François Patthey for his availability and experience with the STM and Stefano Rusponi for sharing so much knowledge for the magnetism and x-ray parts of this work.

I want to thank Darius, Anna, Boris, Clément, Fabian, Dante, Johannes, Jean-Guillaume, Hao, Edgar, Alberto, Tobias, Aparajita, Romana, Fabio, Simone and Oreste. I enjoyed the lunch and the time spent with you. I am happy to have had you as colleagues.

I also would like to thank all the people at the technical workshops, Nathalie and Carole at the secretariat.

Enfin, je tiens à remercier, mes amis, mes parents, mon frère et Maëlle pour leur soutien tout au long de ma thèse.

*Lausanne, May 26, 2022*

Sébastien Reynaud





# Abstract

This thesis presents investigations of magnetic and structural properties of two dimensional metal-organic frameworks and of single atoms, both adsorbed on decoupling layers grown on metal surfaces, with focus on rare earth elements.

We first report on a series of attempts at realizing self-assembled metal-organic networks on different decoupling layers, probed by scanning tunneling microscopy. The aim is to produce regular structures with high surface filling factors such that the magnetic properties of the rare earth atoms in the metal-organic networks can be investigated by X-ray ensemble measurements. The combinations of three molecular ligands (QDC, BDA, ZnTPyP) on three insulating layers (MgO, NaCl, graphene) with Tb as rare earth are reported. Of the three decoupling layers, only graphene is found to allow the synthesis of metal-organic structures. We successfully synthesized large islands of a rare earth-QDC coordination complex, with a majority of fivefold coordination of the rare earth atoms. The same structure is reproduced with Dy and Er.

X-ray absorption spectroscopy, X-ray magnetic circular and linear dichroism measurements are then carried out on the Dy- and Er-QDC/gr/Ir(111) networks. Compared to single atoms on gr/Ir(111), both Dy and Er change their  $4f$  occupancy from  $4f^n$  to  $4f^{n-1}$  and change their easy axis of magnetization. Both species are paramagnetic when incorporated into the metal-organic structure.

The last part of the thesis is devoted to the study of Dy, Ho, and Gd on NaCl thin films. All three atoms display  $4f$  occupancy of the gas phase. The top-Cl adsorption site is determined with scanning tunneling microscopy. The magnetic properties are probed with X-ray absorption spectroscopy, X-ray magnetic circular and linear dichroism. Ho and Gd are paramagnetic. Dy has out-of-plane anisotropy with open hysteresis at non zero magnetic field. However, thermally assisted quantum tunneling of the magnetization prevents remanence at zero field.

**Keywords:** Magnetism, rare earth, lanthanide, self-assembly, metal-organic networks, coordination, scanning tunneling microscopy, X-ray absorption spectroscopy, multiplet calculations, decoupling layer, graphene, NaCl, MgO, thin films, single atom magnets, single ion magnets.



## Résumé

Cette thèse présente l'étude des propriétés magnétiques et structurales de réseaux organo-métalliques et d'atomes isolés, adsorbés sur des couches découplantes, formées sur des surfaces métalliques, avec une attention ciblée sur les terres rares.

Nous présentons d'abord un compte-rendu détaillé de tentatives de réalisation de réseaux organo-métalliques auto-assemblés sur différentes couches découplantes, investigués au moyen de la microscopie à balayage à effet tunnel. L'objectif est d'atteindre un haut recouvrement de la surface par des structures organo-métalliques régulières, de sorte que les propriétés magnétiques des terres rares dans le réseau soient mesurables par des techniques d'ensemble aux rayons X. Les combinaisons de trois molécules (QDC, BDA, ZnTPyP) avec trois couches isolantes (MgO, NaCl, graphène) avec Tb comme métal sont étudiées. Des trois couches découplantes, seul le graphène semble permettre l'auto-assemblage de réseaux organo-métalliques. Nous avons réussi à synthétiser de grands îlots d'un réseau de terres rares - QDC sur gr/Ir(111), avec une majorité des atomes liés à cinq molécules. Le même réseau est reproduit avec Dy et Er.

Les réseaux organo-métalliques Dy- et Er-QDC/gr/Ir(111) sont ensuite investigués par spectroscopie d'absorption des rayons X, ainsi que par dichroïsme circulaire et linéaire. Par rapport aux atomes isolés sur gr/Ir(111), Dy et Er changent l'occupation de leur orbitale  $4f$  de  $4f^n$  à  $4f^{n-1}$  dans le réseau, ainsi que la direction de leur axe facile de magnétisation. Les deux espèces atomiques sont paramagnétiques dans la structure organo-métallique.

La dernière partie de cette thèse est dédiée à l'étude des propriétés magnétiques du Dy, Ho et Gd sur une couche mince de NaCl par spectroscopie des rayons X, ainsi que dichroïsme linéaire et circulaire. Les trois types d'atomes gardent la valence de la phase gazeuse. Le site d'adsorption top-Cl est déterminé au microscope à balayage à effet tunnel. Ho et Gd sont paramagnétiques. Dy présente une courbe d'hystérèse de type 'papillon' ouverte à champs magnétiques non-nuls. Cependant l'inversion de la magnétisation par effet tunnel thermiquement assisté empêche la préservation de l'état magnétique à champ magnétique nul.

**Mots-clés :** Magnétisme, terres rares, lanthanides, auto-assemblage, réseaux organo-métalliques, coordination, microscopie à balayage à effet tunnel, spectroscopie d'absorption des rayons X,

## Résumé

---

couche découplante, graphène, NaCl, MgO, films fins, simulations multiplet, aimants d'atome unique, aimants mono-ioniques.

# Contents

<b>Acknowledgements</b>	<b>i</b>
<b>Abstract (English/Français/Deutsch)</b>	<b>iii</b>
<b>1 Introduction</b>	<b>1</b>
<b>2 Methods</b>	<b>5</b>
2.1 Scanning tunneling microscopy . . . . .	5
2.1.1 Working principle . . . . .	5
2.1.2 EPFL experimental setup . . . . .	8
2.2 X-ray magnetic circular dichroism . . . . .	8
2.2.1 Working principle . . . . .	9
2.2.2 X-Treme end-station . . . . .	13
2.3 Magnetism of a single atom on a surface . . . . .	13
2.3.1 Rare earths . . . . .	15
2.3.2 Spin Hamiltonian model . . . . .	16
2.3.3 Point charge model . . . . .	18
2.3.4 Magnetic relaxation . . . . .	18
2.4 Self assembly . . . . .	20
2.4.1 Overview . . . . .	21
2.4.2 Metal-organic coordination complexes . . . . .	21
<b>3 Self-assembly of metal-organic frameworks on decoupling layers</b>	<b>23</b>
3.1 Overview of the ligands used . . . . .	24
3.1.1 BDA . . . . .	25
3.1.2 QDC . . . . .	27
3.1.3 ZnTPyP . . . . .	28
3.2 MgO/Ag(100) . . . . .	29
3.2.1 BDA . . . . .	30
3.2.2 QDC . . . . .	32
3.2.3 ZnTPyP . . . . .	33
3.3 NaCl/Ag(100) . . . . .	34
3.3.1 BDA . . . . .	35
3.3.2 QDC . . . . .	36

## Contents

---

3.4	Graphene/Ir(111)	37
3.4.1	BDA	38
3.4.2	QDC	39
3.4.3	ZnTPyP	43
3.5	Summary	44
<b>4</b>	<b>Magnetic properties of metal-organic coordination complexes</b>	<b>47</b>
4.1	Experimental	48
4.2	Dy-QDC network	49
4.2.1	Dysprosium on surfaces	49
4.2.2	Results	50
4.3	Er-QDC network	52
4.3.1	Erbium on surfaces	52
4.3.2	Results	52
4.3.3	Note on the point charges	53
4.4	Discussion	55
<b>5</b>	<b>Magnetic properties of rare-earth adatoms on NaCl thin films</b>	<b>59</b>
5.1	Introduction	59
5.2	Results	60
5.3	Conclusions	69
5.4	Methods	69
5.5	Identifying the species observed as a protrusion in atomically-resolved STM images on NaCl thin films	71
5.6	Additional DFT results	72
5.7	Calibration of the NaCl film thickness	73
5.8	Crystal fields of holmium and dysprosium on NaCl/Cu(111)	74
<b>6</b>	<b>Conclusion</b>	<b>75</b>
<b>A</b>	<b>Inelastic electron tunneling spectroscopy on Dy-QDC</b>	<b>77</b>
<b>B</b>	<b>Tables of spectra for the simulations of Dy- and Er-QDC/gr/Ir(111)</b>	<b>79</b>
<b>C</b>	<b>Determination of the ground state of Dy/NaCl/Cu(111)</b>	<b>85</b>
<b>D</b>	<b>Gd/NaCl/Ag(111)</b>	<b>87</b>
	<b>Bibliography</b>	<b>89</b>
	<b>Curriculum Vitae</b>	<b>109</b>

# 1 Introduction

Magnetic moments have their origin in angular momentum, intrinsic or orbital. The smallest known objects within which electrons can maintain angular momentum are single atoms. They can be used to explore atomic scale interactions and understand magnetism at a fundamental level. If atoms manage to preserve the orientation of their magnetic moment against external perturbations for a detectable time, they are referred to as single atom magnets [1], or single ion magnets [2] in the field of molecular magnets. Single atom magnets represent the ultimate size limit for applications in spintronics [3], as well as in classical [4] and quantum [5] information processing. While it is possible to manipulate single free atoms with optical tweezers [6], by far the most convenient strategy for applications and atomic-level investigations is to have them on a supporting surface. The chemical environment of a magnetic element, either in a given adsorption site or in a molecular scaffold is called crystal field, or ligand field. It is responsible for the anisotropic behavior of magnets at the quantum level. Without crystal field, magnetic energy levels are degenerate. The crystal field breaks the symmetry and induces spin anisotropy via spin-orbit coupling. The surface therefore participates in the determination of the system's properties and provides additional degrees of freedom to tune them. Scanning tunneling microscopy allows for direct observation and manipulation of such systems [7–9].

Lanthanides are the series of elements given in figure 1.1. Lanthanides have been thoroughly investigated in the field of single molecule magnets [10]. Member of the family of rare earths, most lanthanides are magnetic and enter into the composition of some of the strongest known magnets today. They also found application in optics and as catalysts. Lanthanide-based single atom and single ion molecular magnets are now an active field of research: the most stable single molecule magnets have a dysprosium ion at their core [11], dysprosium and holmium are the only known cases of single atom magnets [1, 12, 13] and the best single ion molecular magnets on surfaces are terbium-based [14]. The search for single ion molecular magnets and single atom magnets on surfaces also highlighted the need of a decoupling layer to prevent hybridization with the substrate and reduce electron and phonon scattering events that reverse the spin of the magnetic element.

57 <b>La</b> Lanthanum [Xe]5d <sup>1</sup> 6s <sup>2</sup>	58 <b>Ce</b> Cerium [Xe]4f <sup>1</sup> 5d <sup>1</sup> 6s <sup>2</sup>	59 <b>Pr</b> Praseodymium [Xe]4f <sup>3</sup> 6s <sup>2</sup>	60 <b>Nd</b> Neodymium [Xe]4f <sup>4</sup> 6s <sup>2</sup>	61 <b>Pm</b> Promethium [Xe]4f <sup>5</sup> 6s <sup>2</sup>	62 <b>Sm</b> Samarium [Xe]4f <sup>6</sup> 6s <sup>2</sup>	63 <b>Eu</b> Europium [Xe]4f <sup>7</sup> 6s <sup>2</sup>
64 <b>Gd</b> Gadolinium [Xe]4f <sup>7</sup> 5d <sup>1</sup> 6s <sup>2</sup>	65 <b>Tb</b> Terbium [Xe]4f <sup>9</sup> 6s <sup>2</sup>	66 <b>Dy</b> Dysprosium [Xe]4f <sup>10</sup> 6s <sup>2</sup>	67 <b>Ho</b> Holmium [Xe]4f <sup>11</sup> 6s <sup>2</sup>	68 <b>Er</b> Erbium [Xe]4f <sup>12</sup> 6s <sup>2</sup>	69 <b>Tm</b> Thulium [Xe]4f <sup>13</sup> 6s <sup>2</sup>	70 <b>Yb</b> Ytterbium [Xe]4f <sup>14</sup> 6s <sup>2</sup>

Figure 1.1: Extract of the lanthanides series from the periodic table. Data are taken from [15]. Lutetium is omitted (atomic number 71).

Two dimensional metal-organic self-assembly is a technique that can bridge the gap between surface supported single atoms and single molecule magnets [16]. Single atoms tend to diffuse when the temperature is increased and not all single molecule magnets can be evaporated on surfaces. For example Ho/MgO/Ag(100) has a stable magnetization up to 50 K, but starts to diffuse at higher temperature [17]. A possible strategy to overcome this limitation is to embed single rare earth atoms in molecular scaffolds that can prevent diffusion. In order to have thermally stable ordered rare earths atoms on surface, that can potentially exhibit magnetic stability, we try to grow two-dimensional self-assembled metal-organic networks on decoupling layers. In the self-assembly approach, the molecular ligands, that tune the structure of the network and the magnetic properties of metal ions, are deposited on the surface together with the magnetic atoms and a coordination complex is formed on-surface. Lanthanides (or other metal atoms) in the resulting structure are prevented to thermally diffuse with increasing temperature, at least up to the temperature at which the metal-organic structure is stable. The metal-organic self-assembly approach offers great modularity. The coordination number and symmetry of the crystal field can be tuned with appropriate metal-ligand combination. The ligands' backbone also determines the intermetallic distance, allowing for the investigation of the interaction between neighboring metal centers. The ligand's termination and the surface induce the magnetic anisotropy of the metal ions, required to stabilize their magnetic states. Last but not least, in optimal self-assembled structures all the metal centers possess the same environment, an ideal situation for ensemble measurements with space averaging techniques. Today metal-organic frameworks are routinely obtained on metal surfaces with a variety of ligands and metal atoms [18]. However, the growth of metal-organic structures on decoupling layers remains challenging as catalytic properties of metal surfaces can play a role in the formation of coordination structures.

The problem of structural instability of single atom magnets can also be addressed by providing a decoupling substrate on which the adatoms do not diffuse as easily. If the diffusion barrier is high enough and a single adsorption site is favored, single atom magnets could exhibit bistability at even higher temperature than what was observed on MgO. Here we also aim at



---

applying this strategy by investigating the properties of rare earth single atoms adsorbed on a different decoupling substrate. In the following paragraphs we outline the structure and content of this thesis, in which the metal-organic coordination and the change of substrate for single rare earth atoms are explored.

In chapter 2, we briefly describe the methods used in this work, and introduce the fundamentals of atomic magnetism and of self-assembly at surfaces.

In chapter 3, we describe the exploratory attempts carried out using different combinations of molecular ligands and decoupling layers. We chose three representative ligands: quaterphenyl-dicarbonitrile (QDC), biphenyl-dicarboxylic acid (BDA), and zinc-tetrapyrrolyl-porphyrin (ZnTPyP), possessing different symmetry and termination groups. We also picked three decoupling substrates that can be grown as thin layers: NaCl, MgO, and graphene. The self-assembly of the combinations rare earth - ligand - substrate is then investigated by scanning tunneling microscopy. Most of the experiments were carried out using terbium, but we also used dysprosium and erbium.

In chapter 4 we report on the x-ray absorption investigations of the magnetic properties of erbium and dysprosium atoms in the metal-organic structures formed by coordination with QDC ligands on graphene/Ir(111). We try to describe the effect of the coordination with the molecular ligands with a qualitative approach comparing the asphericity of the different magnetic states of erbium and dysprosium.

Chapter 5 describes the magnetic properties of dysprosium and holmium adatoms on NaCl(100)/Cu(111). The NaCl decoupling substrate for single atoms has not been investigated yet. It could provide key informations on the required features of single atom magnets, especially in relation to the Dy and Ho/MgO/Ag(100) system that demonstrated impressive stability. The adsorption site is found with scanning tunneling microscopy and corroborated by density functional theory. Dy atoms exhibits an open butterfly hysteresis loop, evidence of long spin relaxation times at non-zero magnetic field. This chapter is based on a manuscript in preparation.



## 2 Methods

### 2.1 Scanning tunneling microscopy

The tunneling of electrons is a quantum effect first described by Hund in 1927 for the case of a double well potential: particles with small mass can move between regions separated by a classically forbidden energy barrier [19]. One year later, three types of experiments were successfully described with this effect: i) the artificial  $\alpha$ -decay of light elements, ii) the ionization of hydrogen in electric fields, and iii) the high field emission of electrons from cold metals [20]. The tunneling effect found application for the measurement of the energy gap of superconductors in 1960 [21, 22]. In 1982 scanning tunneling microscopy (STM) was invented by Binnig and Rohrer and was used to image surfaces down to atomic resolution in real space for the first time [7–9]. This opened a whole new field of research: the first manipulations of single atoms and molecules followed shortly after [23–25].

Figure 2.1 presents a sketch of the working principle of the STM: the tip, moved by the piezo-tube, scans the sample surface. To obtain the surface's topography, an image can be generated by recording the tip vertical displacement required to maintain constant tunnel current while scanning.

#### 2.1.1 Working principle

In 1961, Bardeen set the basis for the theoretical description of this effect in superconductors separated by an insulating barrier [26]. He demonstrated the independence of the matrix elements (see equation 2.2) from the energy of the states in the electrodes. Tersoff and Hamann adapted the description to scanning tunneling microscopy experiment after Binnig's work [27–29]. A review of modern tools for simulations of STM data that includes the image potential neglected by Tersoff and Hamann [30, 31], along with a summary of the STM theory can be found in reference [32]. Drawing mostly from references [26, 27, 29, 33, 34] we briefly present a simplified description of the tunneling current.

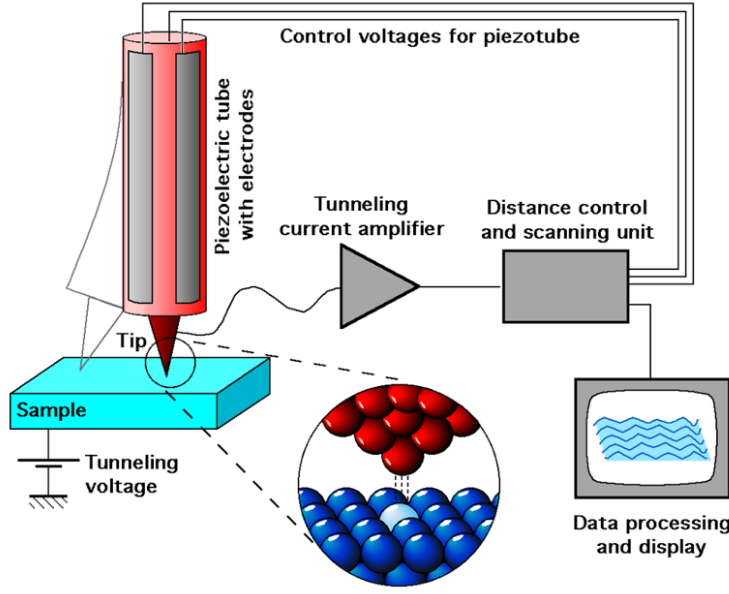


Figure 2.1: Scheme of the functioning of a scanning tunnelling microscope. Image by Michael Schmid and Grzegorz Pietrzak, distributed under a CC-BY 2.0 license.

An electron of mass  $m$  and charge  $-e$  in an initial state within the tip  $|\psi_\mu\rangle$  with energy  $E_\mu$  will move to a final state  $|\psi_\nu\rangle$  with energy  $E_\nu$  with a rate  $W_{\mu\rightarrow\nu}$  that can be described by an expression very similar to Fermi's golden rule:

$$W_{\mu\rightarrow\nu} = \frac{2\pi}{\hbar} |\langle\psi_\mu|O_{ts}|\psi_\nu\rangle|^2 \delta(E_\nu - E_\mu) \quad (2.1)$$

where  $O_{ts}$  is the interaction operator between the tip and the sample,  $\hbar$  is Planck's reduced constant and  $\delta(E_\nu - E_\mu)$  is the Dirac-delta function forcing energy conservation (see figure 2.2). Note that, for this to be the first order perturbation theory leading to the use of Fermi's golden rule, the states  $|\psi_\mu\rangle$  and  $|\psi_\nu\rangle$  should be orthogonal eigenstates of one single Hamiltonian, see reference [35] setting Bardeen's theory in the usual perturbation theory frame. Here we assume that any bias applied to the sample would implicitly be taken in account with a shift in the  $E_\nu$  values. The matrix element  $\langle\psi_\mu|O_{ts}|\psi_\nu\rangle$  has the form of a current density integrated over the surface  $\Sigma$  separating the tip and the sample:

$$\langle\psi_\mu|O_{ts}|\psi_\nu\rangle = \frac{\hbar^2}{2m} \int_{\Sigma} (\psi_\nu(\mathbf{x}) \nabla \psi_\mu^*(\mathbf{x}) - \psi_\mu(\mathbf{x}) \nabla \psi_\nu^*(\mathbf{x})) d\sigma \quad (2.2)$$

where  $\psi(\mathbf{x}) = \langle\psi|\mathbf{x}\rangle$  represents the usual spatial wavefunction. The electrons in the conducting medium populate the states of energy  $E$  with probability given by the Fermi-Dirac distribution:

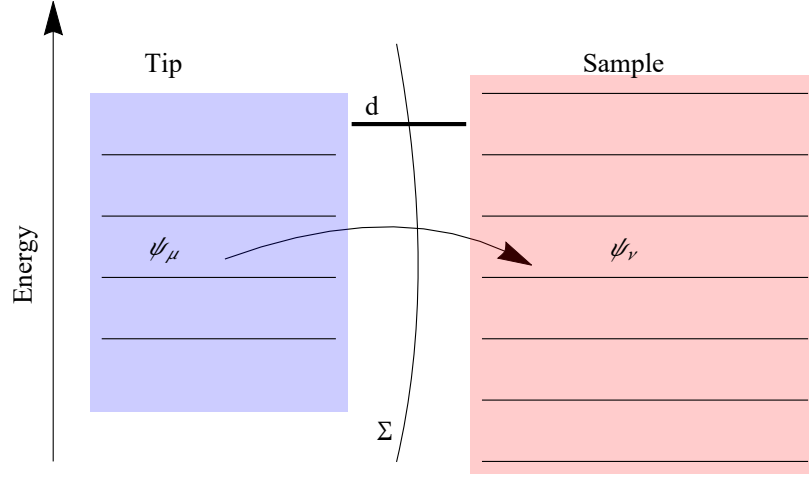


Figure 2.2: Sketch of the tunneling current determination problem. The blue rectangle represents the tip apex and the red rectangle represents the sample surface. The states (horizontal black lines) height represent their energy levels. The horizontal lines in the tip and the sample only represent the states disregarding their occupation.  $\Sigma$  represents the surface between the apex of the tip and the sample and  $d$  is the tip height corresponding to the barrier width.

$$f(E) = \frac{1}{1 + e^{(E-E_F)/k_B T}} \quad (2.3)$$

where  $E_F$  is the Fermi energy,  $T$  the temperature and  $k_B$  Boltzmann's constant. To determine an electron's contribution to the current we need to compute the probability to jump from  $|\psi_\mu\rangle$  to  $|\psi_\nu\rangle$  per unit time. An electron needs to actually be in the initial state and the final state has to be unoccupied, resulting in a probability  $f(E_\mu)(1 - f(E_\nu))$ . Moreover, an electron going from the sample to the tip would contribute negatively to the current, with probability  $f(E_\nu)(1 - f(E_\mu))$ . The resulting current taking into account all states is then:

$$I_{\text{sample-tip}} = -2e \sum_{\mu, \nu} W_{\mu \rightarrow \nu} [f(E_\mu)(1 - f(E_\nu)) - f(E_\nu)(1 - f(E_\mu))] \quad (2.4)$$

where the factor 2 takes into account the spin  $\frac{1}{2}$  degeneracy of the electron. Starting from equation 2.4 we can proceed further and consider different approximations to make the expression more computable or more intelligible. We can use the low temperature approximation and consider the Fermi-Dirac distributions step functions having 0 or 1-values, the low bias approximation (i.e. energy from bias  $eV$  is close to the Fermi energy  $E_F$ ), the localized single tip wave function approximation ( $\mu = 0$ ,  $\psi_\mu(\mathbf{x}) = \delta(\mathbf{x} - \mathbf{r}_0)$ ) where  $\mathbf{r}_0$  is the tip's position), and assume a semi-classical-like exponential decay of the surface's wave functions in the tunnel junction to obtain the following proportionality relation for the tunneling current:

$$I_{\text{sample-tip}} \propto \sum_{\nu} |\psi_{\nu}(\mathbf{r}_0)|^2 \delta(E_{\nu} - E_F) \quad (2.5)$$

where  $|\psi_{\nu}(\mathbf{r}_0)|^2$  is the local density of the state  $|\psi_{\nu}\rangle$  at tip's position  $\mathbf{r}_0$ . This expression tells us that under specific (idealised) conditions the tunneling current is directly proportional to the sum of the local density of states at the tip's position. Alternatively we can assume a spherical tip with  $s$ -like states with exponential spatial decay, replace the sum with a continuum approximation, and ignore anisotropic properties of the  $W_{\mu \rightarrow \nu}$  rates to obtain the following expression:

$$I \propto e^{-2d\sqrt{\frac{m}{\hbar^2}(\phi+E_F)}} \int_{E_F}^{E_F+eV} \rho_T(E - eV) \rho_S(E) dE \quad (2.6)$$

where  $\rho_S$  and  $\rho_T$  are the sample and tip's density of states, respectively,  $d$  is the tunnel junction width,  $\phi = \frac{1}{2}(\phi_T + \phi_S)$  is average of the the work functions of the tip and the sample and we moved to the continuum notation for the energy levels. The exponential factor highlights the sensitivity with respect to the tip-sample distance of such a device.

### 2.1.2 EPFL experimental setup

The setup used for the present thesis at the École Polytechnique Fédérale de Lausanne is shown in figure 2.3 [36]. The ultra-high vacuum (UHV) preparation chamber allows for in-situ preparation with sputtering/annealing tools, evaporators and gas dosing inlets. The gas dosing inlets provide entrance for oxygen for MgO growth and ethylene for growth of graphene by chemical vapor deposition. Evaporators are either effusion cell type for the Mg, NaCl, and molecules, or electron-beam type with high purity rods for the evaporation of elements with a high melting temperature. Here the  $e$ -beam evaporator is used to deposit lanthanides. An additional  $e$ -beam evaporator is installed in the STM chamber for the deposition of adatoms onto the sample at low temperature. The cryogenic temperature of the STM is maintained thanks to one inner cryostat for liquid helium and one outer for liquid nitrogen. The vibrational decoupling is achieved via two stages of pneumatic isolators: the first one decouples the whole UHV chamber from the floor, the second one isolates the inner cryostat, to which the STM is attached, from the rest of the chamber.

## 2.2 X-ray magnetic circular dichroism

In this thesis the X-ray experiments consist of measurement of X-ray absorption spectra (XAS) [37], with circularly or linearly polarized photons produced in synchrotron facilities. The term dichroism refers to the difference in absorption when changing the polarization. The absorption spectra of atoms, their magnetic linear dichroism (XMLD), and their magnetic circular dichroism (XMCD) give precious information about their electronic and magnetic

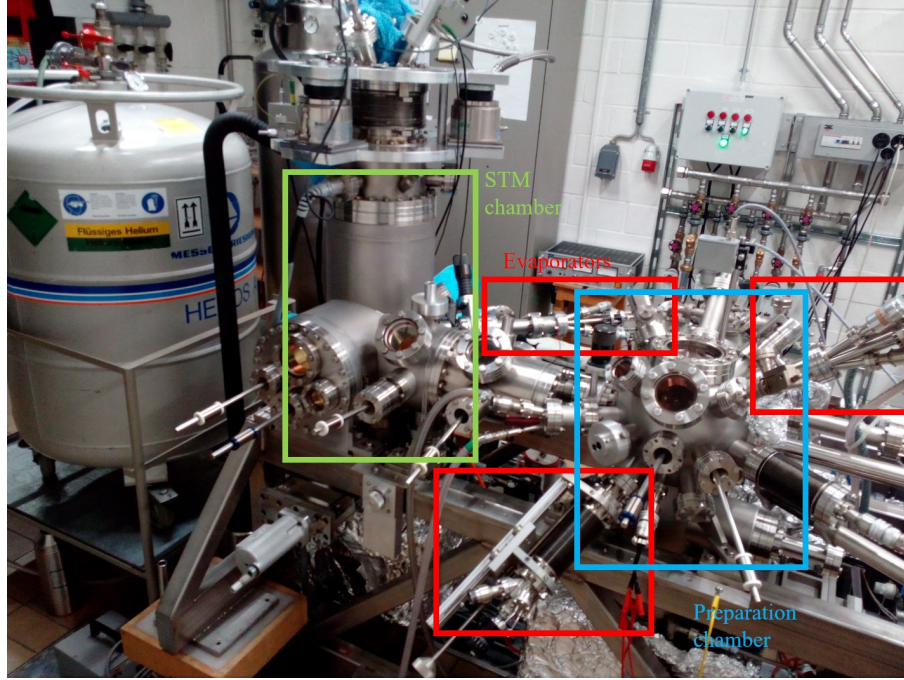


Figure 2.3: Photography of the EPFL STM setup. The STM chamber, the evaporators (on the preparation chamber and on the STM chamber) and the preparation chamber are indicated by green/red/blue rectangles, respectively.

properties. Those dichroic effects were first predicted in 1986 [38] and experimentally observed in 1990 [39–41] in parallel with further theoretical developments [42–47].

### 2.2.1 Working principle

An in-depth description of the electronic transitions in rare earths is out of the scope of this thesis. In order to get a simplified picture of the physics involved, we will consider the simplest possible system of an electron in a spherical potential absorbing a photon.

The starting point of our discussion is the interaction Hamiltonian of the electron in an electromagnetic field  $H_{int} = -\frac{e}{m}\mathbf{p} \cdot \mathbf{A}$ , where  $\mathbf{p}$  is the canonical momentum and  $\mathbf{A}$  is the vector potential of the field. Using as basis the eigenstates of the unperturbed Hamiltonian  $H_0$  of the atom, the first-order transition rate from initial state  $|i\rangle$  to final state  $|f\rangle$  is given by Fermi's golden rule [48, 49]:

$$W_{i \rightarrow f} = \frac{2\pi}{\hbar} |\langle i | H_{int} | f \rangle|^2 \delta(E_f - E_i - \hbar\omega) \quad (2.7)$$

where the  $\delta(E_f - E_i - \hbar\omega)$  function ensures that the energy of the final state  $E_f$  matches the energy of the initial state  $E_i$  plus the energy  $\hbar\omega$  of the absorbed photon. Next we take the dipolar approximation, which is equivalent to assuming that the system feels a uniform electric

field, leading to the expression  $H_{int} = -A_0 \frac{e}{m} \mathbf{p} \cdot \boldsymbol{\varepsilon}$ .  $A_0$  is the amplitude of the vector potential and  $\boldsymbol{\varepsilon}$  can be represented as a complex unit vector indicating the polarization of the electric field. Then we use the commutation relation  $[\mathbf{r}, H_0] = \frac{i\hbar}{m} \mathbf{p}$ , where  $H_0$  is the atomic Hamiltonian without the interaction term  $H_{int}$ . We deduce the following proportionality relation for the transition rate:

$$W_{i \rightarrow f} \propto |\langle i | \mathbf{r} \cdot \boldsymbol{\varepsilon} | f \rangle|^2. \quad (2.8)$$

It is useful to write the operator  $\mathbf{r} \cdot \boldsymbol{\varepsilon}$  in terms of the usual spherical harmonics  $Y_{l,m_l}(\theta, \phi)$  and radius  $r$  in spherical coordinates:

$$\begin{aligned} -\frac{1}{\sqrt{2}}(x + iy) &= \sqrt{\frac{4\pi}{3}} r Y_{1,1} && \text{Right-handed photon} \\ z &= \sqrt{\frac{4\pi}{3}} r Y_{1,0} && \text{Linear photon} \\ \frac{1}{\sqrt{2}}(x - iy) &= \sqrt{\frac{4\pi}{3}} r Y_{1,-1} && \text{Left-handed photon} \end{aligned} \quad (2.9)$$

where we note that only the  $z$  component of a linearly polarized photon has an effect on the interaction Hamiltonian.

In this work we probe the  $M_{4,5}$  absorption edges of rare earths: this means that with the X-rays we excite electrons from the  $3d$  to the  $4f$  shell. Figure 2.4 shows a simplified sketch of the situation with the corresponding XAS for a hypothetical  $4f^{12}$  ground state atom. The  $3d^9$  is split in two multiplets  $3d_{3/2}$  and  $3d_{5/2}$ . The transitions of electrons going from the  $3d_{5/2}$  and  $3d_{3/2}$  produce the  $M_5$  and  $M_4$  absorption edge respectively. Reference [50] lists the XAS of various rare earths on the  $M_{4,5}$  edges. Table 2.1 shows the angular component of the transition matrix elements  $|\langle i | \mathbf{r} \cdot \boldsymbol{\varepsilon} | f \rangle|^2$  for  $M_{4,5}$  transition to the  $4f$  shell. To compute these numbers, the two  $3d$  multiplets with  $J = 5/2$  and  $J = 3/2$  resulting from one unpaired electron in the  $3d$  shell were projected on the  $|3, 2, m_L\rangle |1/2, m_S\rangle$ ,  $m_L = \{-2, -1, 0, 1, 2\}$   $m_S = \{-1/2, 1/2\}$  basis using the Clebsch-Gordan coefficients. The table reflects the selection rules ( $\Delta m_L = \{-1, 0, 1\}$ ,  $\Delta m_S = 0$ ) and we see that the absorption depends on the polarization of the photons and on the occupation (undiscriminated by spin-orbit split) of the  $|4, 3, m_L\rangle$   $m_L = \{-3, -2, \dots, 2, 3\}$  basis elements of the  $4f$  shell. This difference in absorption is the basis for measurements of the dichroism (difference with respect to polarization) of the elements.

A more in-depth analysis of the dichroism between left and right handed polarizations leads to the so called sum rules [44, 45]. For a lanthanide with  $4f^n$  shell occupancy, these relations allow, under specific circumstances [51], to extract the orbital momentum  $\langle L_z \rangle$  and effective spin  $\langle S_{eff} \rangle$  from the integral of the circular dichroism spectrum under the  $M_5$  edge  $X_5$ , the total integral of the dichroism  $X_{4,5}$ , and the total XAS absorption integral  $I$ :



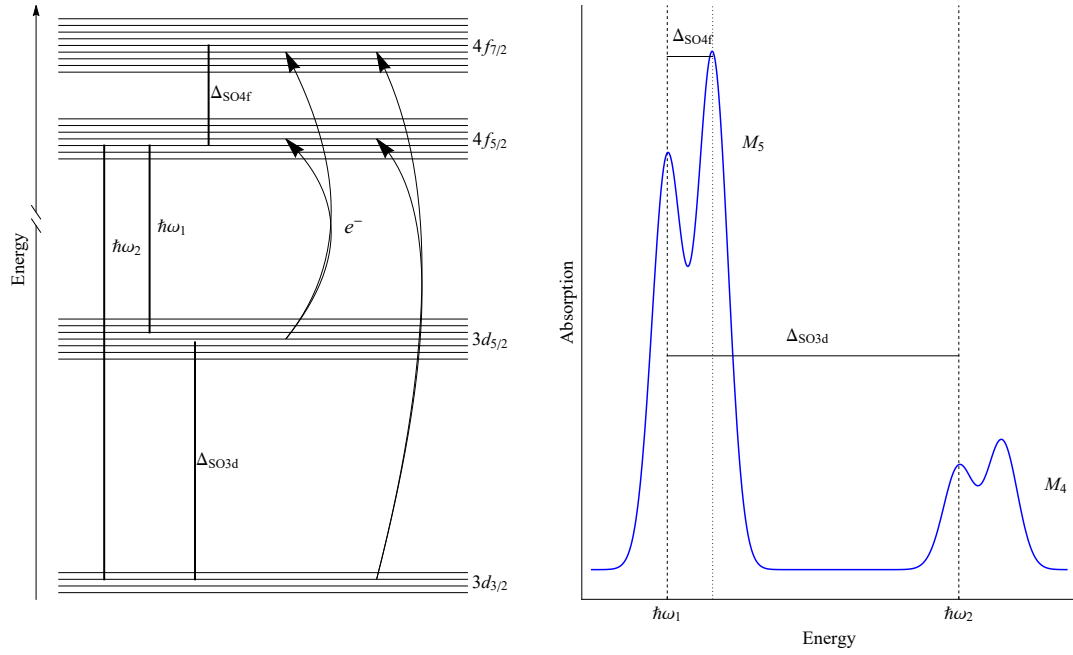


Figure 2.4: Left: Simplified sketch of the energy level scheme of  $3d$  and  $4f$  electronic orbitals where we assume only two multiplets per orbital, split by an energy  $\Delta_{SO}$ . The photon of energy  $\hbar\omega$  is absorbed by one electron in the two  $3d$  multiplets and this electron is promoted to one of the  $4f$  multiplets following one of the four arrows. The energy axis is broken as typically  $\hbar\omega \sim 1000$  eV and  $\Delta_{SO3d} \sim 50$  eV. We ignore the energy splitting within the multiplets in this simple picture, i.e.  $\Delta_{SO3d}$  for example represents the energy splitting between the two  $3d$  multiplets independently of the states within a given multiplets. Right: Sketch of the resulting XAS spectrum (all polarizations). The energies shown on the left panel are displayed on the spectrum. Each of the four peaks corresponds to a transition indicated by an arrow on the left panel.

Table 2.1: Angular transition probability of an electron between the  $3d$  shell (initial state  $|J, m_J\rangle$ ,  $J = \{5/2, 3/2\}$ ) and the  $4f$  shell (final state  $|3, m_L\rangle |1/2, +1/2\rangle$ ) for a right (left) handed polarized photon at the  $M_{4,5}$  absorption edges of a  $4f$  element.

	$ 3, -3\rangle$	$ 3, -2\rangle$	$ 3, -1\rangle$	$ 3, 0\rangle$	$ 3, 1\rangle$	$ 3, 2\rangle$	$ 3, -3\rangle$
$ \frac{5}{2}, \frac{5}{2}\rangle$	0	0	0	0	$\frac{1}{35}$	0	$(\frac{3}{7})$
$ \frac{5}{2}, \frac{3}{2}\rangle$	0	0	0	$\frac{12}{175}$	0	$(\frac{8}{35})$	0
$ \frac{5}{2}, \frac{1}{2}\rangle$	0	0	$\frac{18}{175}$	0	$(\frac{18}{175})$	0	0
$ \frac{5}{2}, -\frac{1}{2}\rangle$	0	$\frac{4}{35}$	0	$(\frac{6}{175})$	0	0	0
$ \frac{5}{2}, -\frac{3}{2}\rangle$	$\frac{3}{35}$	0	$(\frac{1}{175})$	0	0	0	0
$ \frac{5}{2}, -\frac{5}{2}\rangle$	0	0	0	0	0	0	0
$ \frac{3}{2}, \frac{3}{2}\rangle$	0	0	0	$\frac{3}{70}$	0	$(\frac{1}{7})$	0
$ \frac{3}{2}, \frac{1}{2}\rangle$	0	0	$\frac{12}{175}$	0	$(\frac{12}{175})$	0	0
$ \frac{3}{2}, -\frac{1}{2}\rangle$	0	$\frac{6}{35}$	0	$(\frac{9}{175})$	0	0	0
$ \frac{3}{2}, -\frac{3}{2}\rangle$	$\frac{12}{35}$	0	$(\frac{4}{175})$	0	0	0	0

$$\begin{aligned} \langle L_z \rangle &= -3 \frac{h_n X_{4,5}}{I} \\ \langle S_{eff} \rangle &= 2 \langle S_z \rangle + 6 \langle T_z \rangle = \frac{3}{2} h_n \frac{5X_5 - 3X_{4,5}}{I} \end{aligned} \quad (2.10)$$

where  $h_n = 14 - n$  is the number of holes in the  $4f$  shell of the element under consideration and  $\langle T_z \rangle$  the magnetic quadrupole.

Taking into account the strong spin-orbit coupling and neglecting  $\langle T_z \rangle$ , we can infer that the atom's magnetization follows the same dependence on the magnetic field as  $X_5$ :

$$\frac{X_5 h_n}{I} = \frac{1}{5} \langle L_z \rangle + \frac{4}{15} \langle S_z \rangle. \quad (2.11)$$

Even though the right-hand side of the equation is not directly the magnetization, the strong spin-orbit coupling insures that the projection  $\langle S_z \rangle$  follows  $\langle L_z \rangle$ . Further, if we assume that the XMCD spectrum only varies in amplitude and not in shape, we can record the maximum of the XMCD signal as a proxy for the adatom magnetization. Recording the XMCD signal at different magnetic field and angle of incidence will therefore provide valuable information about the anisotropy and magnetization of adatoms.

As could be seen in equation 2.9, a linearly polarized photon only has a  $z$  component in action. This means that the XMLD signal is appropriate to extract geometrical information about the electronic states. Indeed, only orbital extension in the  $z$  direction will absorb linearly polarized

photons, therefore looking at absorption with the two orthogonal linear polarizations and comparing them will highlight specific spatial directions of the orbitals.

### 2.2.2 X-Treme end-station

All X-ray measurements presented in this thesis were performed at the EPFL/PSI X-Treme beamline [52] at the Swiss Light Source synchrotron of the Paul Scherrer Institute in Villigen. Figure 2.5 shows a photograph of the setup and a drawing of it. The end-station is equipped with a preparation chamber for in-situ preparation with UHV evaporators and effusion cells, sputtering and annealing instruments, a room temperature STM and a LEED. Decoupling layers such as graphene or NaCl are grown in the preparation chamber. The sample is then transferred into the cryostat on which several electron-beam evaporators are installed, allowing for the deposition of atoms at room temperature or at cryogenic temperature. The cryostat is equipped with a superconducting magnet which can generate a magnetic field parallel to the direction of the X-rays up to  $B = 6.8$  T. The variable temperature insert on which the samples are fixed for the measurements allows to reach  $T = 2.5$  K.

In our experiments, the X-ray absorption signal is measured using the total electron yield method: the sample is connected to virtual ground via a current amplifier measuring the number of secondary electrons leaving the sample per unit time. The measurements are surface sensitive owing to the limited mean free path of the photo-electrons at the used X-ray energies [53].

## 2.3 Magnetism of a single atom on a surface

One of the themes of this work is the question 'What are the minimal ingredients required to have a magnetic bistable system?'. Now that it is known that single atom magnets are possible, how do we improve their stability?

The magnetic properties of a single atom/ion are determined by its electronic structure, more specifically its unpaired electrons. In free space an atom can have a magnetic moment and be paramagnetic at best, but on a surface the surrounding crystal field can induce magnetic anisotropy in the system: although an electric field does not directly affect the spin, the spin-orbit coupling allows effects on the total angular momentum  $\mathbf{J}$  for which we also use the term spin from now on. Figure 2.6 schematizes the lifting of the degeneracy of the  $m_J$  eigenstates by a surface (i.e. crystal field) introduced below a free-standing magnetic atom. In this example, the atom acquires an out-of-plane easy axis as the two  $m_J = \pm 3$  become the most energetically favorable. However, the crystal field cannot break the time reversal symmetry meaning that energy eigenstates of the atom are either doubly degenerate or form a split doublet with  $\langle J_z \rangle = 0$  with symmetric and antisymmetric combination of the  $J_z$  eigenstates.

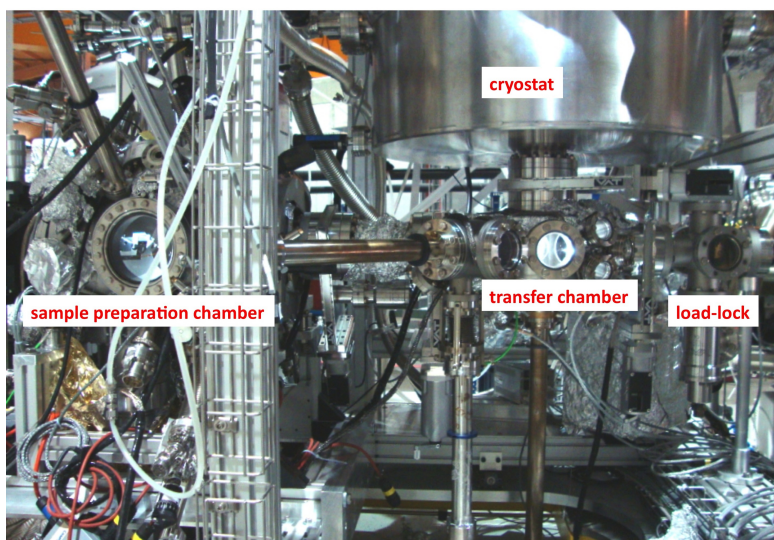
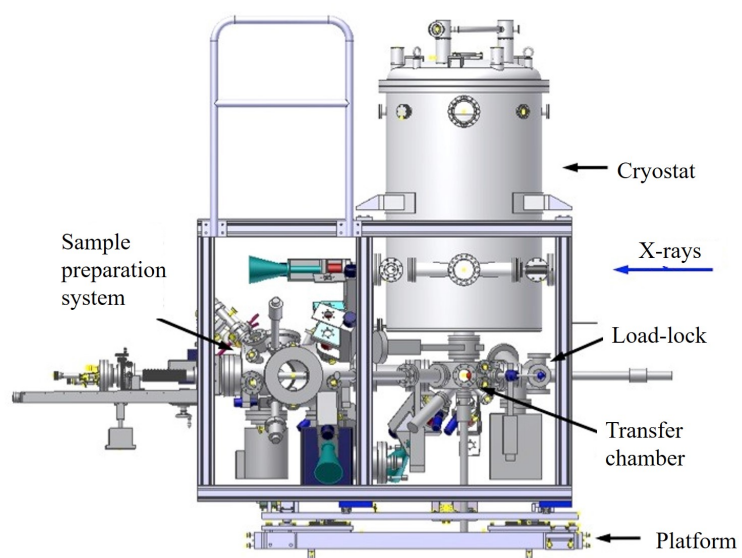


Figure 2.5: Top: Scheme of the X-Treme end station. Bottom: Photograph of the end station [52].

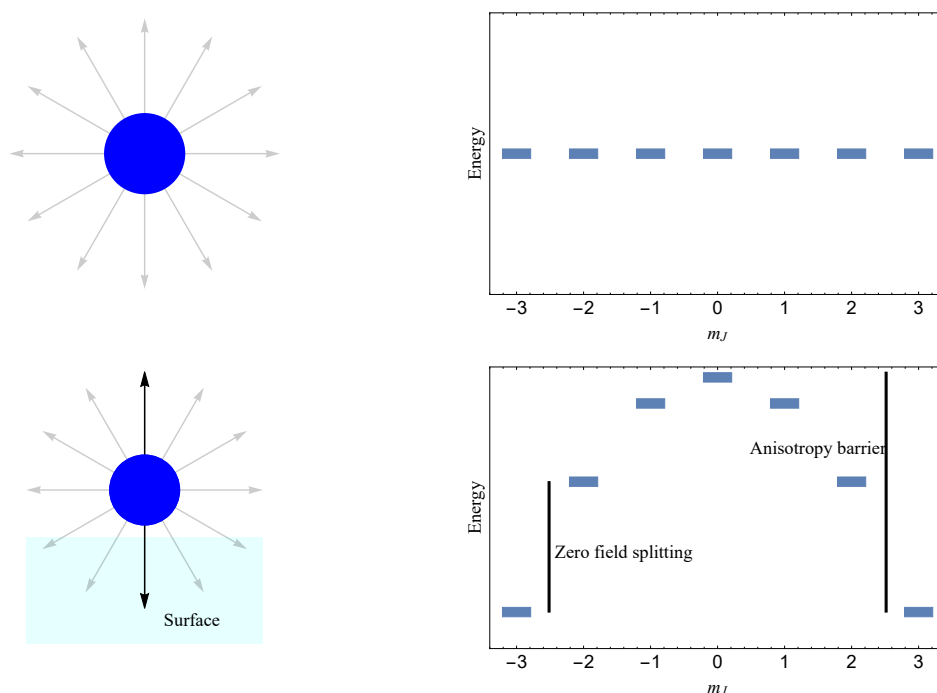


Figure 2.6: Effect of a surface on a  $J = 3$  atom. Top: free atom, all  $m_J$  states are degenerate. Bottom: The introduction of a surface induces the out-of-plane anisotropy of the magnetic moment.

### 2.3.1 Rare earths

The search for the smallest permanent magnets started with single molecule magnets [54]. The first single molecule magnet discovered was the  $\text{Mn}_{12}$  complex [55]. Early work focused on maximizing the total spin of molecular magnets [56]. As the field matured, it was found that it might not be the optimal strategy: the orbital moment in  $3d$  transition metals is usually quenched [57, 58], the polynuclear nature of high-spin molecular magnets makes it hard to obtain global uniaxial anisotropy and the dependence of the anisotropy on the total spin is actually small [59].

Ten years after, the first single ion molecular magnets were discovered with lanthanide complexes [60] and sparked interest in these elements, leading to the discovery of many lanthanide-based single ion magnets [10, 61, 62]. Figure 2.7 shows the radial distribution (spherical potential) of the  $4f$  and  $6s$  shells in an atom with atomic number  $Z = 65$ . Compared to  $3d$  transition metals, the  $4f$  shell of rare earths is buried within the external shells, responsible for binding with the environment, and is therefore protected from quenching [63]. In  $4f$  elements, the strong spin-orbit coupling guarantees that the spin follows the angular momentum affected by the crystal field. Moreover, a single ion being responsible for the magnetism makes it easier to tune the specific crystal field at the quantum level. The molecular structure surrounding the magnetic ion induces anisotropy of the ion mainly through electrostatic interaction [64]. The strong spin-orbit coupling provides a mechanism of action of the crystal field on the atom's

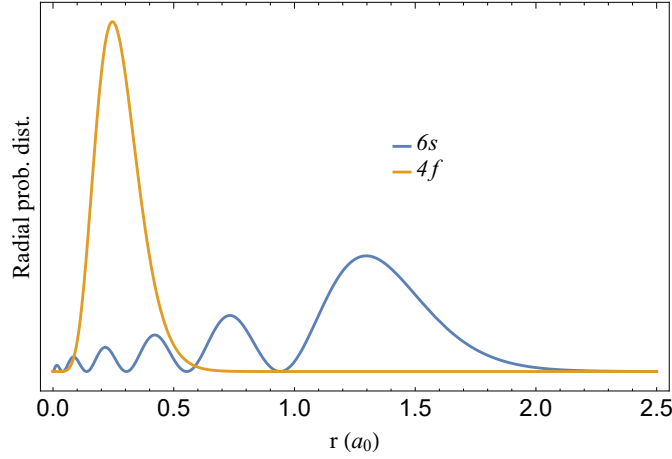


Figure 2.7: 4f and 6s radial distribution of eigenstates of an electron in an ideal hydrogen potential with atomic number  $Z = 65$  in atomic units ( $a_0 = 5.29 \cdot 10^{-11}$  m).

magnetic properties.

In 2016 the first single atom magnet was discovered: Ho adatoms on an ultrathin layer of magnesium oxide grown on Ag(100) exhibit an open hysteresis loop in XMCD measurements up to 30 K [1], followed closely by another open XMCD hysteresis loop demonstrated with Dy adatoms on graphene/Ir(111) [12], and in 2021 the magnetic stability of Dy/MgO/Ag(100) [13] was demonstrated. Around the same time, lanthanide-based single molecule magnets also showed impressive magnetic bistability [11, 14, 65], making rare earths the elements of focus for our work.

### 2.3.2 Spin Hamiltonian model

A useful model when dealing with quantum magnets is the so-called 'spin-Hamiltonian model'. The time independent Hamiltonian describing a rare earth atom in a weak (with respect to spin-orbit splitting) magnetic field can be written as [66] (in order of significance):

$$H_{atom} = H_{coulomb} + H_{SO} + H_{CF} + H_Z \quad (2.12)$$

where  $H_{coulomb}$  is the sum of all Coulomb interactions between electrons and nucleus,  $H_{SO}$  is the spin-orbit coupling,  $H_{CF}$  is the electrostatic interaction between the crystal field (also called ligand field in single molecule magnets) and electrons, and  $H_Z$  is the Zeeman term coming from the interaction of the atom's magnetic dipole with the external magnetic field. While smaller than  $H_{CF}$ ,  $H_Z$  can still induce level crossing of the order of the zero field splitting. Note that  $H_{coulomb}$  and  $H_{SO}$  are approximately spherically symmetric.  $H_{CF}$  represents the effect of the surrounding charges, it is intuitively given in 'cartesian' coordinates.  $H_Z$  is an axial term.

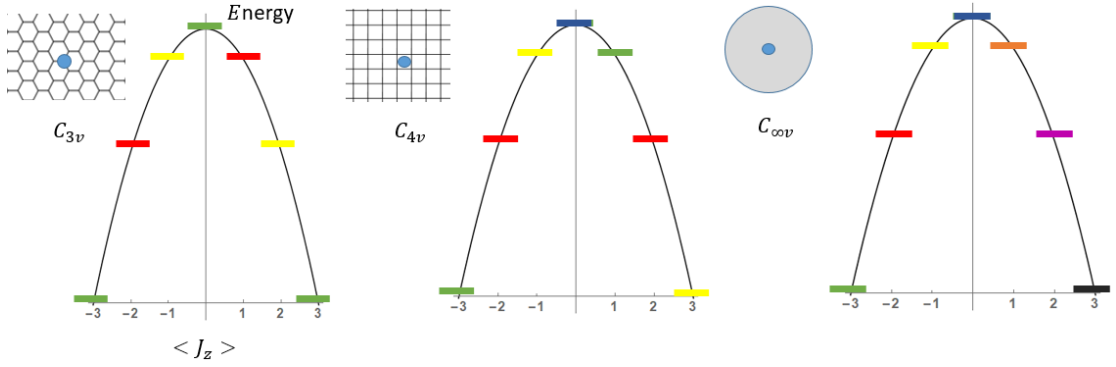


Figure 2.8: Sketch of the energy and spin expectation of the eigenstates of a system with  $J = 3$  for threefold (left), fourfold (middle) and axial (right) symmetry. States of the same color represent states that are connected by the crystal field and the pure  $m_J$  state is not an eigenstate of the Hamiltonian anymore.

This asks for a common representation of the eigenstates of the atom. Stevens [67] offered a way to write the  $H_{CF}$  in the  $|J, m_J\rangle$  basis. He used the Wigner-Eckart theorem after having expanded  $H_{CF}$  on a spherical basis and defined the so called Stevens operators  $O_m^p \propto (\alpha J_+^m + \beta J_-^m)$ , where  $\alpha$  and  $\beta$  are coefficients,  $m$  and  $p$  ( $m \leq p$ ) are integers and  $J_{\pm}$  are the usual ladder operators of the spin- $J$  representation. The Hamiltonian  $H_{CF}$  can then conveniently be written as:

$$H_{CF} = \sum_p \sum_m B_m^p O_m^p \quad (2.13)$$

where  $B_m^p$  are the Stevens coefficients. Such operators have been used in single molecule magnets modelling [2, 68–70]. The  $4f$  shell has angular momentum number  $l = 3$  such that only terms with  $p = 0, 2, 4, 6$  don't vanish. Note that  $O_m^p$  only contains terms proportional to the  $m^{\text{th}}$  power of the ladder operators, and will therefore only mix states with difference  $\Delta m_J = km$ ,  $k \in \mathbb{Z}$ . For a single atom on a surface, a symmetry  $C_{nv}$  will only contain terms with  $m = 0, n, 2n, 3n, \dots$  [71–73]. This gives rise to a nice picture of the effects of the surface's crystal field on the adatom as can be seen in figure 2.8. The threefold symmetry (left) is bad for the bistability of a  $J = 3$  system as the ground states  $\langle J_z \rangle = \pm 3$  are connected and the spin can flip through quantum tunneling of the magnetization. The fourfold symmetry (middle) is more likely to give a bistable magnetic system as the  $m_J = \pm 3$  states are not connected by the crystal field, but tunneling could occur in case of scattering event (see section 2.3.4) changing the state to one of the  $m_J = \pm 2$  that are connected. Finally, in the case of a fully axial field (right), the atom would have to go through the whole anisotropy barrier in order flip its spin as all states are separated. As a general rule, one expects a high symmetry adsorption site with the appropriate value of  $J$  to offer better protection from relaxation of the magnetization by tunneling.

### 2.3.3 Point charge model

$H_{CF}$  of equation 2.12 can also be treated directly in real space. In this approach the total electrostatic interaction between point charges representing the crystal field around the magnetic atom is computed [74–76]. A list of effective point charges is estimated, for instance with Mulliken analysis [77]. The definition of the point charges is however a tricky task and their position and value (beyond the symmetry) must be interpreted with caution. The multiplet computations can then be performed with the help of dedicated tools, in this thesis such computations are performed using the multiX software [78]. From multiplet computation of the 'one electron excited states' we have access to the spectroscopic properties of the atom.

Given a series of point charges, Hutchings [79] showed how to obtain the Stevens coefficients. The steps are spelled out in the appendix of reference [80]: one has to expand the Coulomb's potential of each point charge on the real (also called 'tesseral') spherical harmonics and apply the operator equivalent method of Stevens. The resulting equations, providing the bridge from the point charge model to spin Hamiltonian formalism can be found in reference [81].

### 2.3.4 Magnetic relaxation

A notable distinction to be done for magnetic rare earths on surfaces is the difference between half-integer and integer  $J$  adatoms at zero external magnetic field (therefore in a time-reversal symmetric state). Indeed the action of the time-reversal operator on a system with odd number of electrons cannot return the same state. This forces all half-integer spin systems to be at least doubly degenerate at zero magnetic field and is the result of Kramers theorem [82]. In contrast, systems with even number of electrons can form a split doublet resulting in states with  $m_J = 0$  both, typically from symmetric/antisymmetric combination of the original  $m_J = \pm k$  states. Figure 2.9 shows the  $C_{4v}$  with  $J = 3$  from figure 2.8 (middle) with a split doublet. For the split doublet, the overlap between the  $m_J = \pm 2$  is much greater than for the separated states. It provides a pathway for thermally assisted quantum tunneling of the magnetization, where a phonon or an electron changes the spin of the atom from the  $m_J = -3$  state to  $m_J = -2$ . The large mixing between the two  $m_J = \pm 2$  increases the probability of relaxation toward the  $m_J = +3$  state, meaning that the spin flipped.

Once the system's static properties are set, we have a basis for the out of equilibrium description of the magnetization. In general the dynamics must be treated in a full quantum rate equation [83]. The rate (master) equation allows to take the real time evolution of a system out of the thermodynamic equilibrium into account, in particular it allows the modeling of the magnetic hysteresis at a given field sweep-rate. Typically, in the cases of interest in this thesis, we can use classical rate equations to track the relaxation of any magnetic state toward a Boltzmann distribution of quantum states. The characteristic time to reach that equilibrium is called the lifetime  $\tau$  of the system. Given a set of states (eigenstates of any quantum operator)  $\{|\psi_1\rangle, \dots, |\psi_n\rangle\}$ , and their respective population  $\{P_1, \dots, P_n\}$  the rate equation is written:



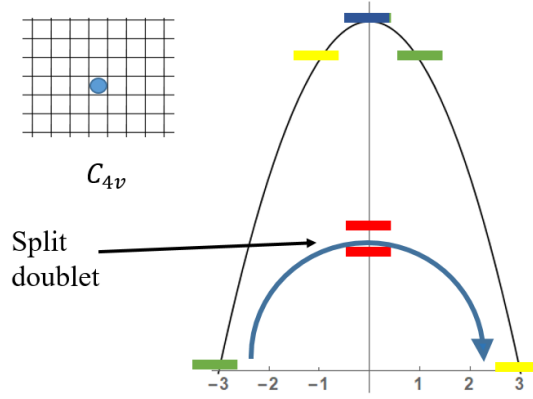


Figure 2.9: Scheme of the reversal of a  $m_J = -3$  to  $m_J = +3$  by tunneling through the split doublet (red).

$$\dot{P}_i = \sum_{j=1}^n v_{ij} P_j - v_{ji} P_i \quad (2.14)$$

where the  $v_{ij}$  have the unit of a frequency and represents the strength of the dynamic coupling between states  $\psi_j$  and  $\psi_i$ . The equilibrium magnetization  $m_{eq}$  of the thermalized system is given by :

$$m_{eq} = \sum_j \langle \psi_j | g \mu_B \mathbf{J} | \psi_j \rangle \exp \left( -\frac{E_j}{k_B T} \right) \quad (2.15)$$

where  $\mu_B$  is Bohr's magneton,  $E_j$  is the energy of  $|\psi_j\rangle$ , and  $g$  is the Landé factor. From equation 2.14 we can usually extract the global  $\tau$  as the characteristic time for convergence toward  $m_{eq}$  in the absence of external forcing.

The determination of the coupling rates  $v_{ij}$  is not an easy task: for single ion magnets on a non magnetic surface, the relaxation occurs via spin-electron [84] or spin-phonon scattering [85, 86]. Figure 2.10 shows sketches of two scattering processes. Spin-electron scattering is caused in unperturbed systems by substrate electrons. This relaxation process typically accounts for a constant independent of the temperature since the Fermi-Dirac distribution of electrons remains unchanged in the temperature range considered (typical Fermi temperature of metals  $> 10^4$  K). In order to determine its strength, the electron density of states of the surface needs to be investigated. Electrons used to probe the magnetic quantum state, such as secondary electrons in XMCD measurement and tunneling electrons in STM, can also play a role and lead to spin reversal [87]. In the case of single molecule magnets the main relaxation pathway is spin-phonon scattering as the magnetic ion is often in a molecular cage and shielded from spin-electron scattering processes [88, 89]. Phonons can also induce change in the angular momentum of magnetic elements [90–92]. Spin-phonon scattering is a bit more complex than spin-electron. Several processes, allowing for different relaxation pathways are conceivable

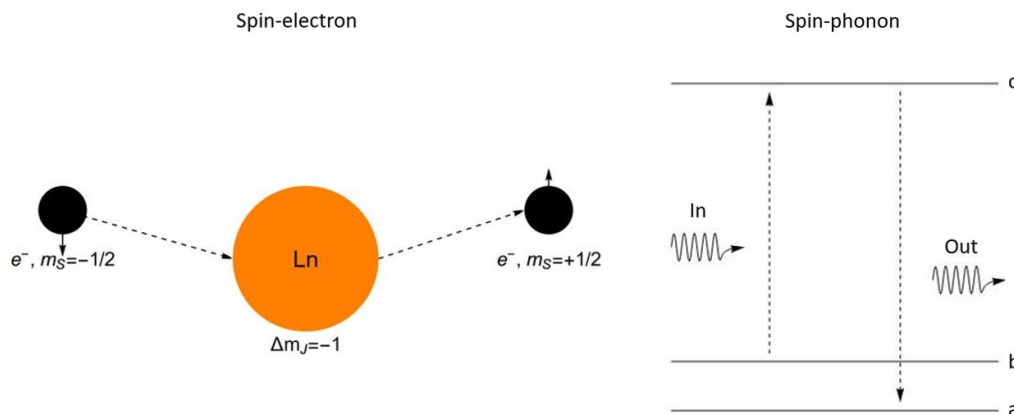


Figure 2.10: Sketches of scattering events. Left: spin-electron scattering, the electron changes its spin by  $\Delta m_S = +1$  and thereby decrements the total angular momentum of the magnetic lanthanide atom (orange disk) by  $\Delta m_J = -1$ . Right: two-phonon scattering event, where the system relaxes to state *a* from *b* through an intermediate state *c* (Orbach process).

with first and second order perturbation approaches [93, 94]. Their most noticeable feature is their temperature dependence, which allows discriminating between the different processes [95–97].

## 2.4 Self assembly

The limiting factor in studying the thermal stability of Ho single atom magnets is the spatial diffusion [98]. On the other hand the hysteresis of Dy single atom magnets on graphene/Ir(111) closes at 12 K due to insufficiently large energy barriers to prevent spin reversal [12]. A path to improve both these limiting factors is to embed the rare earth atoms in a molecular superstructure. The resulting framework can prevent diffusion of the rare earths. In addition, the metal-molecule bound could play a role similar to that of molecular cage in single ion magnets and provide a new way of tuning the crystal field. In this work, we try to synthesize such coordination structures through self-assembly at surface.

Self-assembly is the spontaneous association of subunits into a larger ordered structure, interacting in such a way that the thermodynamic equilibrium is reached. In the self-assembly approach, one chooses the ingredients and the thermodynamic 'macro' variables ensuring that the desired nanoscale structure will build itself bottom-up. Self-assembly on surfaces involves complex interplay of substrate-adsorbate and adsorbate-adsorbate interactions.

### 2.4.1 Overview

Several strategies are available to obtain nanostructures or atoms organized into patterns at surfaces. When structures self-assemble on a surface, the coverage can reach mesoscopic scale in contrast to the highly unscalable path of building of a structure with an STM tip. The first surface self-assembled structure used the dislocation networks formed by thin metal films grown on fcc(111) metal surfaces (Ag/Pt(111) and Cu/Pt(111)) as nucleation templates for Ag and Fe nanoclusters [99]. Superlattices of single atoms can form taking advantage of long range surface-state mediated interactions [100]. The Moiré pattern of graphene on hexagonal metal surfaces can also be used as template for creation of lattices of clusters [101] or single atoms [102].

Molecules' geometry and chemistry constrain the coordination with neighboring molecules. Therefore, allowing molecules to diffuse on the surface [103, 104] can result in the formation of ordered self-assembled supramolecular structures [105–110]. Note that the molecules themselves can also undergo polymerization [111] and conformational change on the surface [112].

### 2.4.2 Metal-organic coordination complexes

Metals and molecules combined on surfaces constitute a vast playground. Some molecules accept in-situ insertion of a metal atom [113, 114]. Alternatively, the metal atom can act as coordination center with the molecular ligands stabilizing the structure as shown in figure 2.11: this is the focus of our work.

Pioneering works in this field in 2003 displayed coordination complexes of Fe with a variety of organic ligands [115–119]. Transition metal were used at first, exhibiting two to four coordination [120–122]. A proper combination of ligand and metal centers lead to the impressive self-assembly of Sierpinski-like triangles [123]. Later, lanthanides were also used for synthesis of metal-organic coordination complexes, exhibiting in general higher number of possible coordinations, especially with nitrogen terminated ligands [18, 124–127]. Note also that metal-organic frameworks can in turn be used as template to grow superlattices of adatoms [128, 129].

As seen in the previous section, the ligand field greatly influences the electronic state and therefore the magnetism of the metal atom. Putting together these techniques provides new strategies to possibly stabilize the structure and the spin of lanthanides in a variety of 2D geometries.

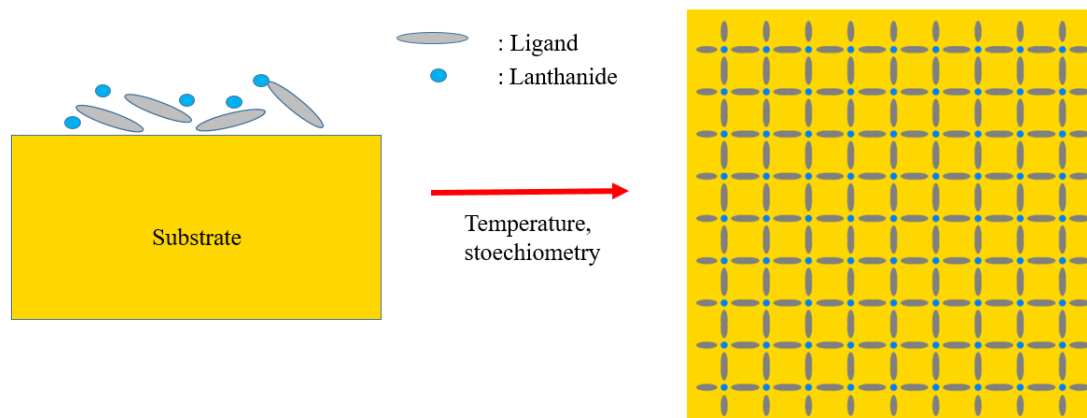


Figure 2.11: Scheme of synthesis of a 2D self assembled metal-organic structure. We adjust the substrate temperature of deposition or annealing to promote diffusion and reactivity of the adsorbate. Tuning the stoichiometry can lead to different types of structures.

### 3 Self-assembly of metal-organic frameworks on decoupling layers

As highlighted at the end of the previous chapter (section 2.4.2), metal-organic frameworks on a surface offer several advantages over isolated surface adsorbed magnetic atoms. The molecular ligands are composed of two parts. The first is an inactive backbone that determines the geometric properties of the resulting framework and can be changed to tune the size and the symmetry of the structure. The second is the active part that binds to the rare earth and must be considered in the understanding and modeling of the ligand field surrounding the rare earth atoms. The possibility to change those two features opens the road for the design of robust magnetic metal-organic networks with structural stability up to room temperature.

From the magnetism standpoint, the need for a decoupling layer is motivated by the absence of magnetic remanence for single atoms on a metallic surface. Magnetic remanence in nanoscale structures on metal surfaces was observed at sub-kelvin temperature [130–132] but reducing the system's size greatly reduced lifetimes. The smallest systems exhibiting bistability are trimers [132, 133]. Also for single molecule magnets, magnetic stability on metallic surfaces was difficult to demonstrate [134–138] until the impressive magnetic bistability of  $\text{TbPc}_2/\text{MgO}/\text{Ag}(100)$  was found [14]. The decoupling layer helps the magnetic ions to keep their remanence as scattering events with substrate electrons and phonons are largely reduced. Only recently there has been an effort to produce metal-organic frameworks on metal-supported insulating layers [139–142], but the process is very challenging as decoupling layers can interfere with the catalytic effect that metal surfaces may have in the formation of the networks.

This chapter presents exploratory work in the synthesis of metal-organic coordination complexes on decoupling layers. For these investigations, we aimed at finding robust growth protocols, that one can easily reproduce on different experimental setups, especially in view of ensemble measurements at synchrotron radiation facilities. In fact, reproducibility of growth protocols working in a very narrow range of parameters is very delicate. In this respect, room temperature preparations are ideal.

A good decoupling substrate is insulating (or at least has low density of states at the Fermi

level) and has a low phonon density of modes, both features help reduce the probability of a scattering event that would reverse the spin of the single ion magnet. The decoupling layer also helps protecting the magnetic elements from hybridization with the metallic substrate. Common ultrathin layers reported in the literature are magnesium oxide (MgO) and other metal oxides, sodium chloride (NaCl), graphene and hexagonal boron nitride (h-BN). In this work we used MgO, NaCl and graphene. These three decoupling layers have allowed lanthanide single atoms to exhibit open hysteresis loops [1, 12] (see chapter 5 for the case of NaCl) and are therefore a good starting point for our investigations.

## 3.1 Overview of the ligands used

Most common molecular active terminations used to grow metallo-organic two dimensional structures are nitrile (CN), pyridine ( $C_5H_5N$ ) and carboxylate ( $COO^-$ ) groups. Other less common terminations include phenolate ( $C_6H_5O^-$ ) [122] and thiolate ( $S^-$ ) [143] moieties. The nitrile and pyridine groups tend to form planar flexible bonds with metals on metal surfaces [124, 144] and the carboxyl one forms robust planar ionic bonds with lanthanides following deprotonation into a carboxylate anion [127]. Rare earths are reported to behave as hard Lewis acids and therefore display strong affinity with the three aforementioned terminations [126, 145]. Three ligands have been chosen for this work: quaterphenyl-dicarbonitrile (QDC), biphenyl-dicarboxylic acid (BDA) and zinc-tetrapyridyl-porphyrin (ZnTPyP). The carboxylate moiety was chosen as it proved to form robust bonds with lanthanides on metals [127, 146] and some studies of magnetic properties of coordinated metals on surfaces bound to carboxylate moieties were already performed [119, 142]. The carbonitrile moiety provides 'ready to self-assemble' linkers that don't require to be transformed on the surface and produces coordination complexes at room temperatures [124]. The ZnTPyP pyridine terminated linkers might require some annealing [139] to incorporate metal atoms but their shape can induces stronger symmetry constraints on the resulting network. The three linker's respective structures are depicted in figure 3.1. The results are thought to be generalizable to any molecular backbone with the same binding groups, provided the molecular diffusion takes place and sufficient space around the rare earth atom is available. In the following sections we describe the ligands and their self-assembly on Ag(100).

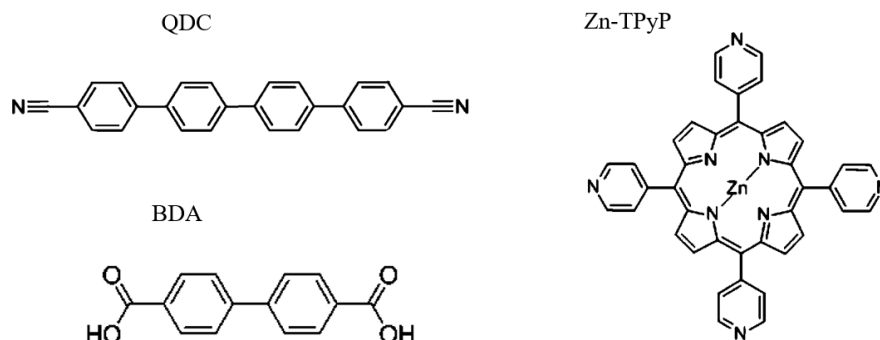


Figure 3.1: Sketch of the molecular ligands used in this work.

### 3.1.1 BDA

This linear molecule presents two phenyl rings as backbone and is terminated by two carboxylates. The version with one phenyl ring, terephthalic acid (TPA) is more studied in the literature. In the absence of metal atoms, these molecules self-assemble in two types of molecular networks. The structure depends on the protonation status of the carboxyl groups [147–150]. When the hydrogen at the extremity is bound to the molecule, it will form hydrogen bridges with neighboring carboxylate leading to molecules binding along their axis, as reported in reference [151]. This can also make it difficult to create metal-organic structures on decoupling layers with intrinsically reduced catalytic activity as the deprotonated molecules are necessary to form robust bonds with metals [116, 117]. Coordinated to Fe single atoms, only four oxygen bind to the metal [119], but thanks to the generally higher coordination number of lanthanides the coordination of TPA with Ho atoms exhibits eightfold coordination [146], which could be relevant for symmetry consideration of the magnetic states.

Motivated by the work of reference [146] that presents coordination of TPA with holmium atoms on Ag(100), we started with TPA. Unfortunately annealing to 440 K is needed on Ag(100) for the surface to catalyze the deprotonation reaction and the desorption temperature of TPA was below experimental accuracy of our setup (temperature measured with a pyrometer). This led us to favor BDA for which we expect very similar chemistry, but a higher binding energy to the surface.

The BDA molecules were evaporated on a Ag(100) surface from powder heated in an effusion cell at 470 K. The silver surface was previously cleaned with cycles of sputtering (800 eV, 4  $\mu$ A current on the sample) and annealing at 770 K. Figure 3.2 shows STM images of two structures, one obtained after deposition at room temperature, and one after annealing at 440 K. Upon room temperature deposition, the molecules self-assemble into compact islands stabilized by linear hydrogen bonds of the carboxyl groups resulting in a periodicity of approximately 1.5 nm along a given row. Upon annealing to 440 K, we obtain a precursor phase comparable

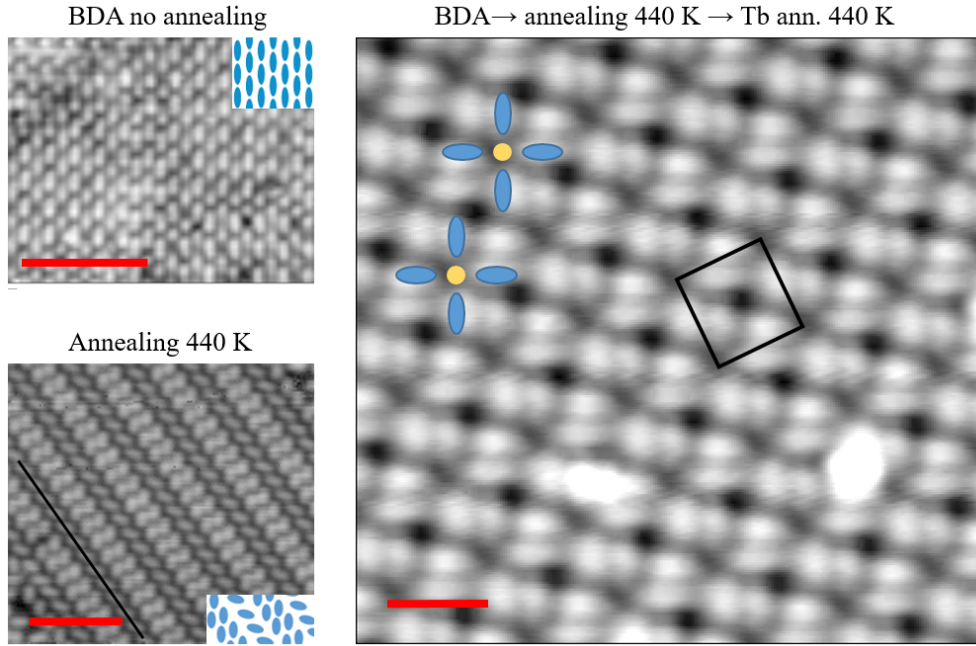


Figure 3.2: STM images of the deposition of BDA on Ag(100). The blue ellipsoid and yellow disks as insets represent the BDA molecules and the Tb atoms respectively. Left: BDA deposited at room temperature (tunneling conditions:  $V_t = 500$  mV,  $I_t = 100$  pA, 50 K, scalebar is 10 nm) and BDA/Ag(100) deposited at 440 K (tunneling conditions:  $V_t = 1$  V,  $I_t = 100$  pA, 5 K, scalebar is 10 nm). The black line indicates a row of fully deprotonated BDA molecules. Right: BDA deposited on Ag(100) at room temperature followed by annealing at 440 K, addition of Tb at 440 K. The black square highlights the unit cell with a 2 nm size. Tunneling conditions:  $V_t = 1$  V,  $I_t = 100$  pA, 5 K, scalebar is 2 nm.

to the II phase of reference [150], where partial deprotonation of the BDA molecules induces repulsion between deprotonated carboxylate groups and formation of hydrogen bonds with the hydrogen atoms of the phenyl rings. The molecules indicated by a black line on the figure are thought to be fully deprotonated as they do not form linear bonds with neighboring molecules. Upon addition of Tb at 440 K on the precursor phase, followed by 5 minutes of annealing at 440 K, we obtain large islands of a periodic cloverleaf structure, see right panel in figure 3.2, comparable with the one reported in reference [146] for Ho and TPA. The Tb atoms at the center of the cloverleaf appear as depressions, however, with an apparent height significantly above the one of the substrate. For  $\text{Ho}(\text{TPA})_4$  cloverleaf metal-organic structure, the Ho-Ho distance representing the lattice parameter of the quadratic superstructure, is 1.5 nm [146]. This is consistent with the observed 2 nm Tb-Tb distance in our  $\text{Tb}(\text{BDA})_4$  network, as indicated by the black square with each corner on a Tb atom highlighting the unit cell.



### 3.1.2 QDC

This molecule and similar ligands with variation of the backbone phenyl ring number have been widely used in the synthesis of two dimensional metal-organic networks on surfaces. Alone on a metal surface, it already exhibits several self-assembled structures [152–154]. In the absence of coordinating metal atoms on the surface, the self-assembly happens through the attractive interaction of the nitrogen termination with the hydrogen atoms on the sides of the phenyl rings of the neighbors and the repulsive interaction between charged nitrogen atoms. The resulting superstructures can form a densely packed chevron layer, as well as triangular, rhombic or kagomé structures. The carbonitrile groups have consistent affinity with metal atoms on the surface, be they codeposited or coming from the substrate [154–158]. With 3d metals the carbonitrile terminated linkers will favor three/fourfold symmetric coordination around the metal centers. One can choose the length of the ligands by adjusting the number of phenyl rings of the backbone [155, 156] or choose a non linear backbone to change the geometric constraints on the metal-organic structures [159]. The self-assembly of a densely packed layer of the hexaphenyl version of the molecule was studied on graphene/Cu(111) [160]. The sexiphenyl version is also reported to form an hexagonal metal-organic network with copper coordination centers on graphene/Ir(111) [140].

Figure 3.3 shows an STM image acquired after deposition of the molecules on a Ag(100) substrate kept at room temperature, from an effusion cell evaporator heated at 450 K. The molecules do not diffuse to form islands at room temperature, and small cross-shaped structures are visible. In the absence of coordinating metal atoms on the surface, we expect the relative orientation of the neighboring QDC molecules to be either similar to the chevron-like packing observed on gr/Ir(111) (see figure 3.16) or to the chiral rhombic structure that QDC forms on Ag(111) [152] depicted in the lower scheme of figure 3.3. The upper scheme instead displays a model of the structure visible in the STM image: the nitrogen groups point toward each other, indicating the presence of a metal atom in the center of the complexes (black disks). We deduce that surface Ag adatoms are used to form small coordinated structures. The absence of compact islands of coordination complexes indicates low mobility at room temperature. The ligands appear to favor two orthogonal directions, reminiscent of the (100) surface orientation of the Ag substrate.

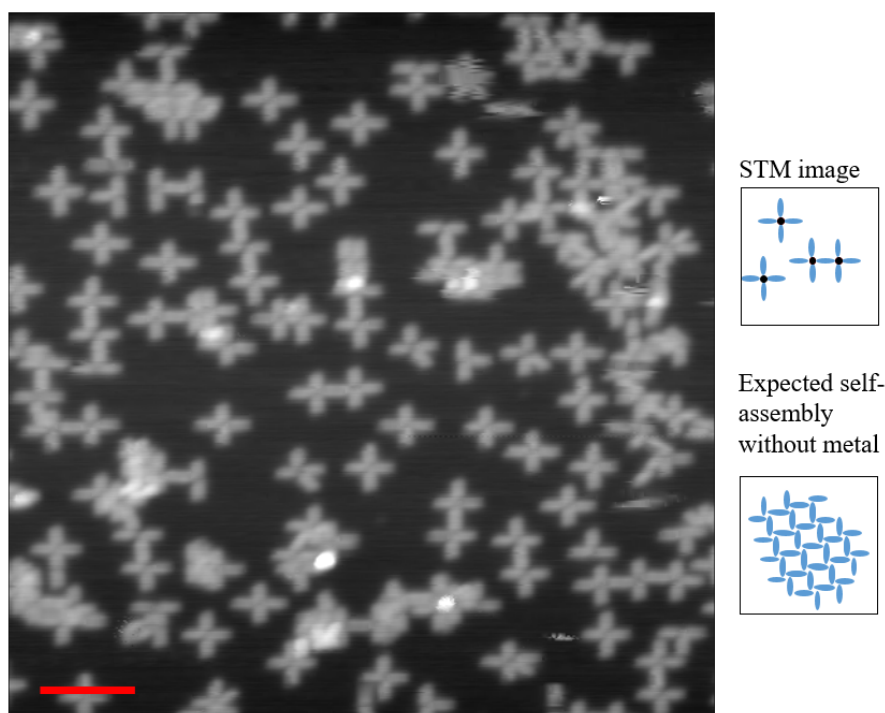


Figure 3.3: STM image of QDC deposited on Ag(100). Upper inset: model of the STM image with the black disks representing a metal coordination center and the blue ellipsoid representing the QDC linkers. Lower inset: depiction of the self-assembly at room temperature of QDC/Ag(111) without metal atoms. Tunneling conditions:  $V_t = -500$  mV,  $I_t = 100$  pA, 5 K, scalebar is 10 nm.

### 3.1.3 ZnTPyP

The core of this molecule is a porphyrin, known in biology for being a precursor to heme and chlorophyll. Literature on porphyrin on metal surfaces is rich and a review can be found in reference [161]. Legs can be added to the porphyrin core such as phenyl rings (or pyridine in our case) and the center can host a metal atom (Zn in our case). The self-assembly properties at room temperature can depend on the presence or not of the metal atom in the center as the non metalated version tends to interact more strongly with the substrate [162–164]. The metalated version of the molecule appears to be more prone to self assembly and the zinc ion also prevents metalation of the porphyrin with rare earths during deposition, that would complicate the analysis of XMCD ensemble measurements. Self assembly of the TPyP version was reported in references [165, 166] and in reference [144] for the ZnTPyP metalated type, where coordination with Cu atoms is also reported.

Figure 3.4 shows an STM image of ZnTPyP molecules on Ag(100). The molecules were deposited on the substrate held at room temperature from an effusion cell heating the powder at 670 K for 7 min. They form a compact structure similar to the one reported in reference [166], characterized by a distance of approximately 1.5 nm along rows (indicated by a black line) in

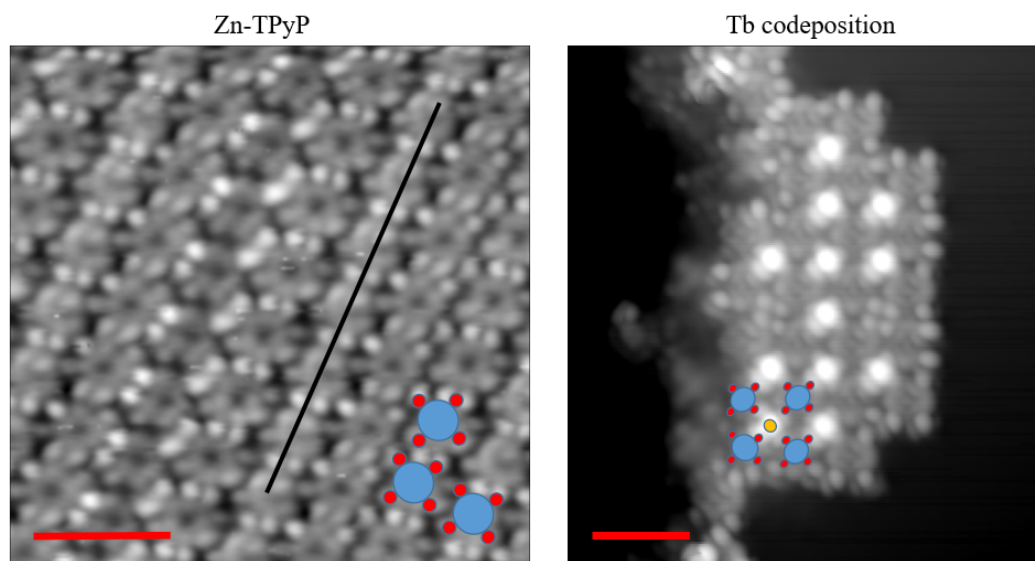


Figure 3.4: STM images of ZnTPyP on Ag(100). Overlaid model where red, blue and yellow disks represent, respectively, the pyridyl legs, the porphyrin macrocycles, and the Tb atoms. Left : ZnTPyP deposited on Ag(100), tunneling conditions:  $V_t = -2$  V,  $I_t = 50$  pA, 77 K, scalebar is 4 nm. The black line highlights the row of molecules. Right: Coordination structure with Tb atoms, tunneling conditions:  $V_t = -2.5$  V,  $I_t = 80$  pA, 5 K, scalebar is 4 nm.

which all molecules have the same orientation. When terbium is added on the molecules, followed by annealing at 400 K, we observe formation of an almost square coordination structure similar to the rhombic lattice described in reference [144] (see also figure 3.9) with a distance of approximately 2 nm between two nearest Tb atoms.

### 3.2 MgO/Ag(100)

Magnesium oxide (MgO) is an insulating ionic crystal with  $\text{Mg}^{2+}$  and  $\text{O}^{2-}$  ions. Bulk MgO has a bandgap of 7.8 eV [167]. The (100) surface of bulk MgO displays a 6.2 eV gap [168] and was shown to approximately preserve its gap down to three monolayers [169]. DFT investigation of free standing monolayers still predict a bandgap of 3-4 eV. Overall, ultrathin layers of MgO maintain a phonon density of states similar to the bulk one with few modes below 30 meV [1, 170]. Ho/MgO/Ag(100) was shown to relax via a local vibration mode at 4.7 meV, unaffected by the delocalized substrate phonons [97]. The growth on Ag(100) is not straightforward as depending on deposition/cooling conditions multiple layer islands start to form before the silver surface is fully covered [171]. The number of layers can be discriminated with field emission resonance spectroscopy to detect image potential states due to variation of the work function [172]. The MgO layer thickness is known to impact the electronic properties of single atom magnets [173].

MgO proved useful in improving magnetic properties of single atoms and single molecule

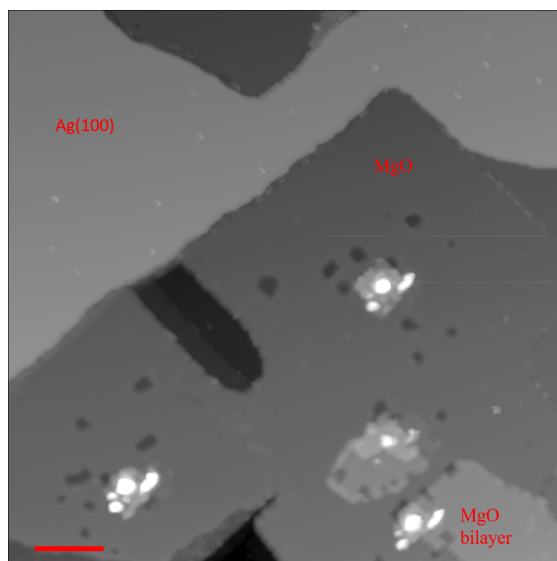


Figure 3.5: STM image of MgO islands on Ag(100), 40% of the overall silver surface is covered. Tunneling conditions:  $V_t = 1$  V,  $I_t = 100$  pA, 77 K, scalebar is 20 nm.

magnets [1, 13, 14, 174, 175]. Therefore, it is a promising material to decouple quantum magnets from electron and phonon originating from the underlying metallic substrate.

Starting with a clean Ag(100) surface, we heat it to 750 K and expose it to a pressure of  $5 \cdot 10^{-7}$  mbar of  $O_2$ . We then expose the hot sample to an Mg evaporation cell at 670 K for 10 min followed by a 20 min slow cooldown to reach a 40% MgO coverage with mostly monolayer and some MgO bilayer islands. Figure 3.5 shows the Ag(100) surface, covered by a large one monolayer thick MgO island and a few small bilayer islands. The higher terrace in the upper part of the image is silver. The lower part of the image is the MgO, identified with spectroscopy.

#### 3.2.1 BDA

An STM image of BDA deposited on MgO/Ag(100) is shown in figure 3.6. BDA molecules exhibit very low mobility, even after annealing at 440 K, as concluded from the fact that small areas of MgO are not covered. In fact, we interpret the grey, irregular areas with homogeneous apparent height as uncovered MgO (see area delimited by the black curve). Figure 3.6 seems to indicate that deprotonation occurs more uniformly on the MgO monolayer as most molecules are perpendicular to their neighbors. On the contrary, on the bilayer many molecules appear hydrogen bonded (aligned with their axial neighbors). If deprotonation is leveraging electrons from the metal to happen, this effect could be due to the decoupling effect of the MgO that increases with the number of layers, as the silver surface used as catalyst for deprotonation is closer to the molecules on the monolayer.

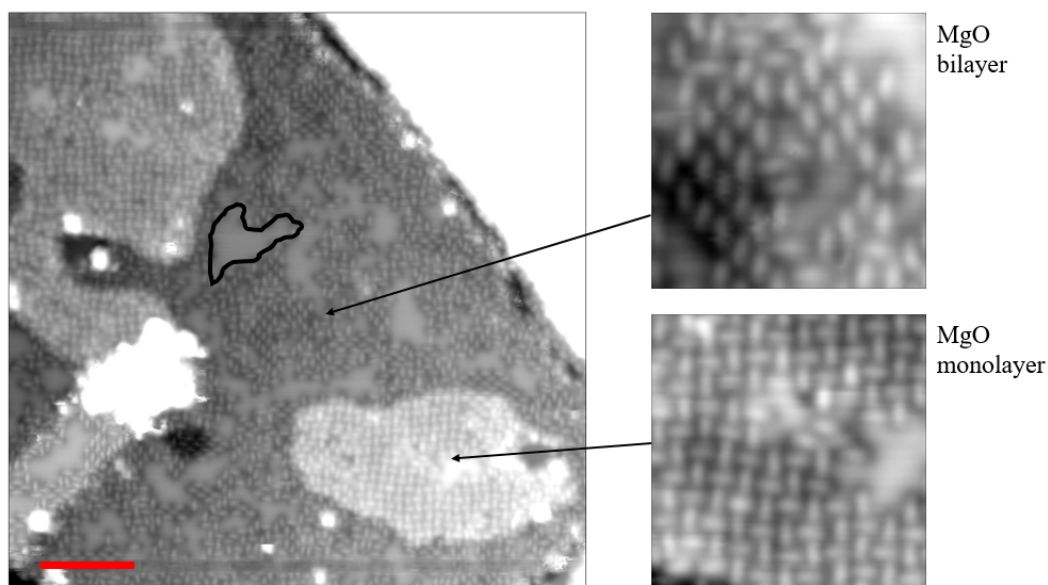


Figure 3.6: STM image of BDA deposited on MgO/Ag(100) followed by an annealing at 440 K. The area delimited by a black curve indicates one of the areas of clear MgO. Tunneling conditions:  $V_t = 1$  V,  $I_t = 100$  pA, 5 K, scalebar is 10 nm.

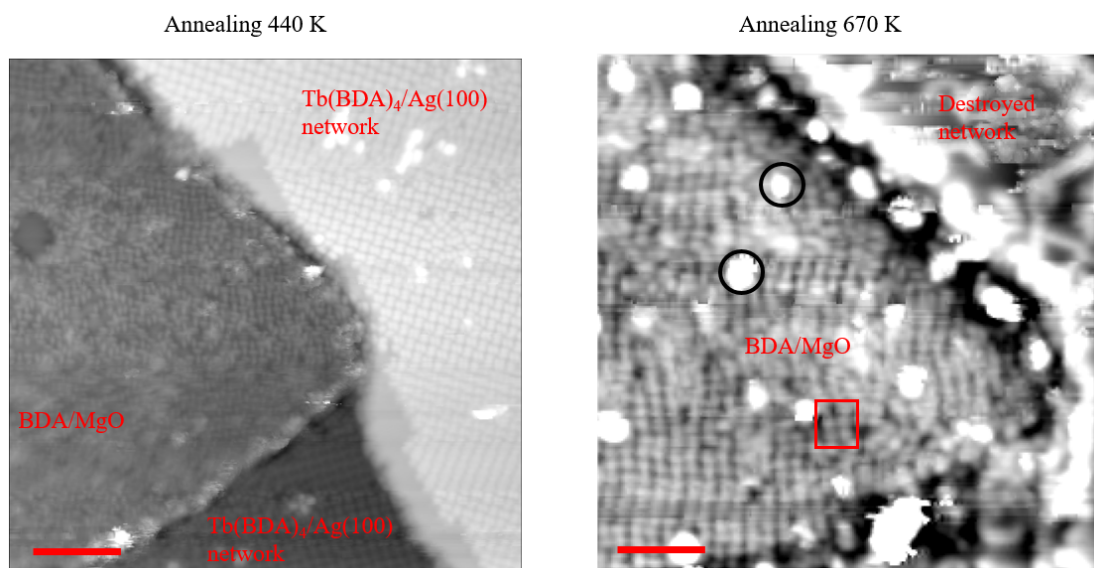


Figure 3.7: Left: STM image of BDA deposited on MgO/Ag(100) followed by an annealing at 440 K and Tb addition, tunneling conditions:  $V_t = 500$  mV,  $I_t = 200$  pA, 5 K, scalebar is 10 nm. Right: Same preparation as for previous image, followed this time by annealing to 670 K after Tb deposition. Tunneling conditions:  $V_t = 1$  V,  $I_t = 50$  pA, 5 K, scalebar is 5 nm.

Subsequent deposition of terbium with annealing at 440 K produces the coordination complex on Ag(100) terraces, as seen in figure 3.7. However little change on the MgO monolayer islands

was observed. Progressively rising the annealing temperature to 670 K destroyed the structure on Ag(100) but the molecular network does not incorporate the Tb atoms on MgO, except maybe for a few isolated units (see red rectangle), where, although the orientation of the molecules is not easy to determine, the appearance of a cloverleaf unit is indicative of Tb incorporation. This is in accordance with the low amount of coordinated  $\text{Ho}(\text{TPA})_4$  complexes found on MgO/Ag(100) in reference [176]. We rather observed the formation of large undefined clusters (denoted by black circles), probably made of Tb. This indicates a strong interaction of the molecules with the MgO surface leaving almost no room for additional coordinating metal adatoms. No significant difference was observed between the mono and bilayers of MgO.

#### 3.2.2 QDC

Deposition of QDC on MgO/Ag(100) produces a surface where all silver terraces are covered by molecules but the MgO islands are entirely void, as seen in figure 3.8. The affinity of QDC with MgO is not sufficient to cover its surface, in stark contrast with the BDA/MgO system. This could be due to the lower electronegativity of the single nitrogen atom compared to the two oxygens of the carboxyl group that can interact with the Mg atoms of the MgO surface, but further DFT investigations should be performed to clarify this point. Presence of a two-dimensional molecular gas on MgO that does not appear in the STM image is not excluded, but the increase in molecule density on silver (compared to figure 3.3, where the same quantity of QDC was deposited) indicates that the molecules diffuse on MgO toward the Ag terraces. Codeposition of QDC and Tb also left the MgO terraces clear of molecules. In the future one could try to deposit the molecules at cryogenic temperature to verify if the QDC molecules can stick on MgO. However, even if successful, further steps would be needed to obtain the metal-organic complexes. During this work we did not investigate this system further.

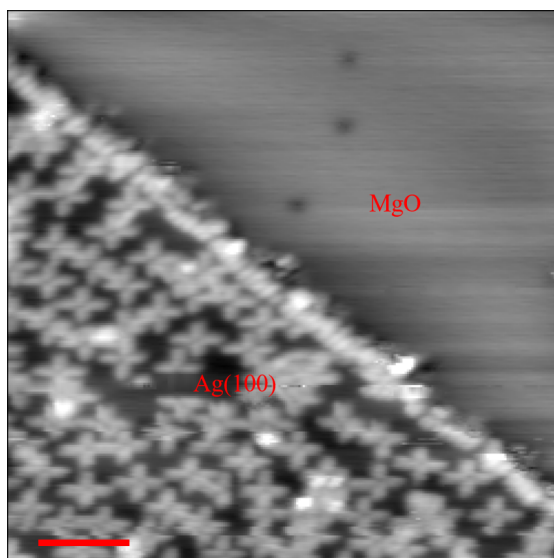


Figure 3.8: STM image of QDC deposited on MgO/Ag(100), tunneling conditions:  $V_t = -1$  V,  $I_t = 175$  pA, 77 K, scalebar is 8 nm.

### 3.2.3 ZnTPyP

The deposition of ZnTPyP on MgO/Ag(100) seems to suffer from the same low/no adsorption on MgO as the QDC molecules, as can be seen in figure 3.9. The coordination structure forms large patches on the silver surface (see figure 3.4), but molecules are absent on the MgO islands. We did not investigate this system further.

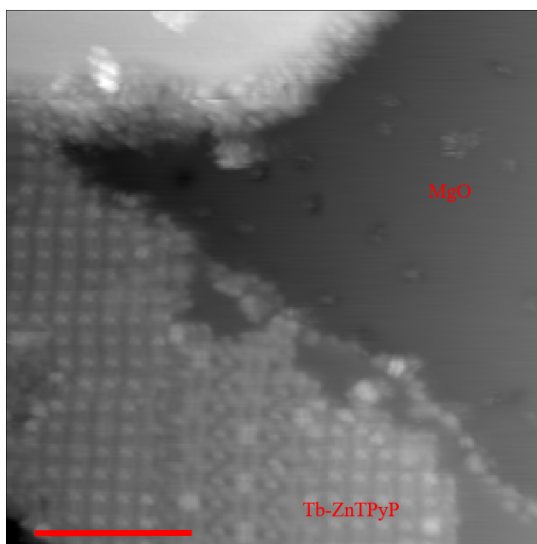


Figure 3.9: STM image of Tb and ZnTPyP deposited on MgO/Ag(100), after annealing at 400 K. Tunneling conditions:  $V_t = -2.5$  V,  $I_t = 80$  pA, 77 K, scalebar is 12 nm. The coordination complex is only present on the Ag(100) terrace while the MgO layer is empty.



### 3.3 NaCl/Ag(100)

Sodium chloride (NaCl) is an ionic crystal and has  $\text{Na}^+$  and  $\text{Cl}^-$  atoms bound together in the same crystal structure as MgO. In bulk the bandgap is 8.7 eV and the low-energy phonon density of states is slightly higher than for MgO, as NaCl is softer [177, 178]. The growth of ultrathin films on metallic surfaces is less tricky than the one of MgO, since the film grows in extended islands simply from room temperature deposition of the NaCl from effusion cells [179–181]. The thickness of the NaCl islands can also be discriminated with field emission resonance spectroscopy [182].

Ultrathin NaCl films were used since 2004 to decouple molecules from metallic substrates in STM experiments and to demonstrate charging of single adatoms [183–185]. While they proved useful for decoupling, it is worth noting that some organic molecules tend to dissolve the NaCl thin films [186–190]. As we require a decoupling effect from the NaCl layer, we will look only for systems that leave the NaCl island intact.

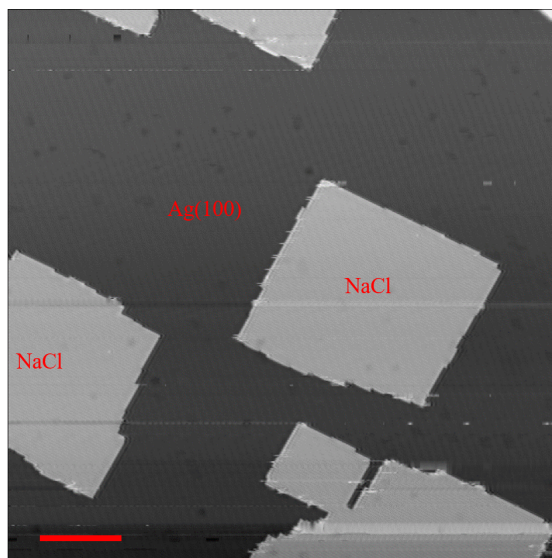


Figure 3.10: STM image of NaCl bilayer islands on Ag(100). Tunneling conditions:  $V_t = -2$  V,  $I_t = 70$  pA, 77 K, scalebar is 30 nm

The preparation of NaCl/Ag(100) goes as follows: first the silver single-crystal is cleaned by sputtering and annealing cycles. We then let the sample cool down for 15 min and expose it at 300 K to a NaCl evaporation cell heated at 720 K for 25 min. Figure 3.10 shows an STM image of the resulting surface. Under these conditions, a Ag(100) surface 40% covered by NaCl islands is obtained.



### 3.3.1 BDA

Figure 3.11 (left) shows sample after the deposition of one monolayer of BDA on NaCl/Ag(100) at room temperature. Approximately 50 % of the surface was covered by NaCl islands before deposition of BDA. The most important change of the surface is that the NaCl islands have disappeared. In addition, a new unknown structure, hard to characterize, is observed and covers most of the sample. Annealing to 420 K produces ordered patches of an unreported phase of BDA (figure 3.11 right). The protrusions visible on the latter image, interpreted as molecules, are shorter than the BDA/Ag(100), possibly due to deprotonation that is known to reduce molecular apparent length to sub-nanometer [150]. A tentative model of the molecular arrangement is proposed. The ordered phase resembles the protonated phase on Ag(100) but here the molecules are aligned laterally to form the rows visible on the image. The dissolution of the NaCl islands can be rationalized by considering that the carboxyl group was reported to react with NaCl at room temperature via metalation with Na and chlorine evaporation [187, 188], this could be part of an explanation for the appearance of the novel molecular phase, although no obvious coordination structure was observed in our experiments. Na and TPA both appear as protrusion in reference [187] but only molecules seem to be resolved in our system. A possible position for the Na atoms is proposed in the sketch in the right inset (black disks), provided the deprotonation happens, since alignment of the carboxylate moieties is unlikely. Since we aim for a system that leaves the decoupling layer intact, this makes BDA/NaCl an unsuitable candidate for the formation of rare-earth-based coordination structures.

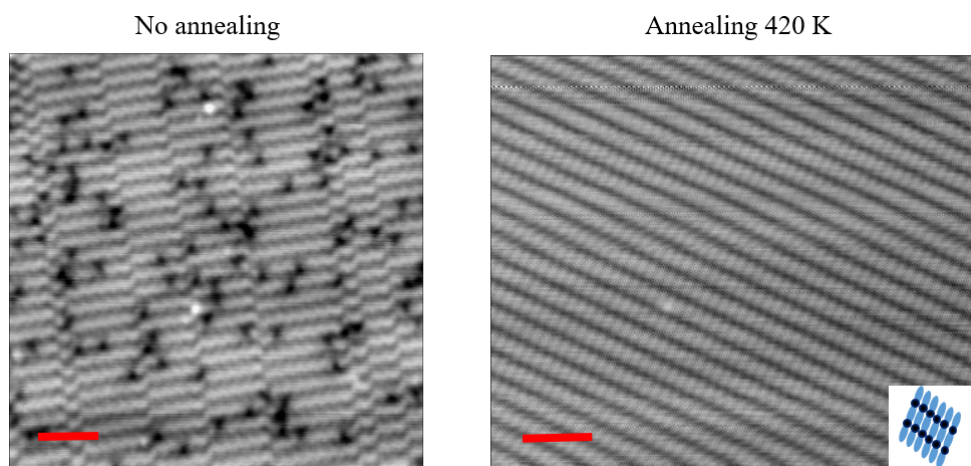


Figure 3.11: Left: STM image of BDA deposited on NaCl/Ag(100). Tunneling conditions:  $V_t = 50$  mV,  $I_t = 100$  pA, 50 K, scalebar is 4 nm. The inset represents a very approximate tentative model of the arrangement. Right: STM image of BDA deposited on NaCl/Ag(100) after annealing to 420 K. Tunneling conditions:  $V_t = 50$  mV,  $I_t = 100$  pA, 50 K, scalebar is 3 nm. The inset represents a tentative model of the positions of the molecules (blue ellipsoid), with a black disk indicating a probable position of the Na atoms.

We tried the codeposition of BDA and Tb on the sample at 440 K, with slightly lower (0.7 ML) BDA coverage to have some adsorbate-free terraces to help understanding the systems. As expected, the cloverleaf structure of figure 3.2 is found on the Ag(100) terraces (not shown). Figure 3.12 shows an STM image of an NaCl island (lower right part of the image) adjacent to a molecular island (upper left part). Single Tb adatoms are visible as protrusions on the NaCl island, meaning that they did not diffuse during the annealing, possibly due to insertion of the Tb atom at the Na sites. The molecules seem to assemble in the same phase as the one shown in figure 3.11 (right), this time however islands of second layer on top of the first one are visible. In particular, an extended second layer molecular island follows the edge of the NaCl island. This seems to indicate that the BDA molecules start to dissociate the NaCl island from the edges. Note that in reference [187], the Na-TPA metal-organic structures are reported to form independently of whether NaCl or TPA is deposited first.

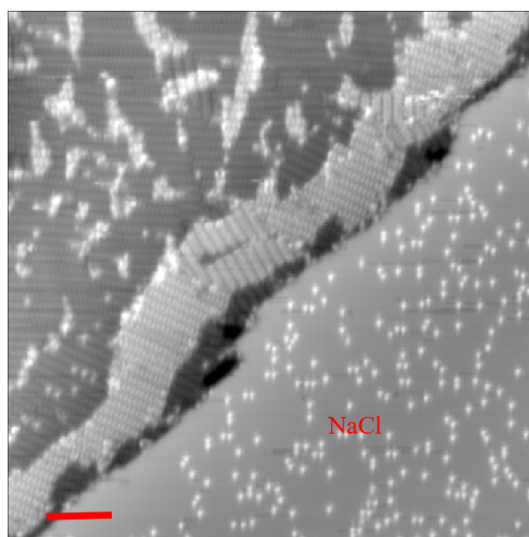


Figure 3.12: STM image of BDA deposited on NaCl/Ag(100) after annealing to 440 K and Tb addition at 440 K. Tunneling conditions:  $V_t = 50$  mV,  $I_t = 80$  pA, 50 K, scalebar is 10 nm.

#### 3.3.2 QDC

Figure 3.13 shows the sample after deposition of QDC at room temperature (covering approximately 70% of the surface) on an Ag(100) surface preemptively 40 % covered by NaCl. We observe the formation of a nicely ordered lattice with square symmetry with a periodicity of  $\sim 4$  nm. This new phase is not observed on silver alone with similar molecular coverage. Also in this case, the NaCl islands have entirely disappeared, indicating that also these molecules dissolve the NaCl islands such that we did not investigate the QDC on NaCl system further. As for the carboxyl group, the cyano group was reported to break the NaCl ionic bond to form a Na-molecule complex [190]. In figure 3.13 we propose a model for the observed structure, see inset.

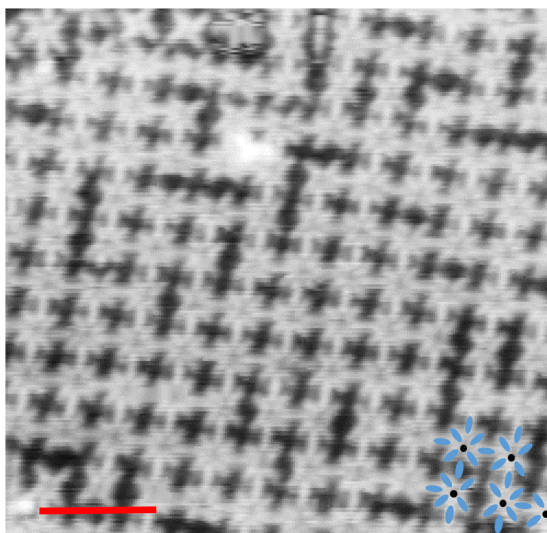


Figure 3.13: STM image of QDC deposited on NaCl/Ag(100). Tunneling conditions:  $V_t = 50$  mV,  $I_t = 100$  pA, 5 K, scalebar is 9 nm. Inset: blue ellipsoids represents the molecules and the black disks represent the proposed Na atoms positions.

### 3.4 Graphene/Ir(111)

Graphene, the 2D honeycomb lattice made of carbon atoms, is famous today in nanosciences. Graphene is a conductor along its plane but a good insulator in the direction perpendicular to it. It shows a Dirac cone in its band structure in the freestanding or graphite form [191]. It is a very stiff material with little vibrational modes in the few meV range in graphite or in graphene grown on Ir(111) [192, 193]. Its properties on metal surfaces are reviewed in reference [194]. Its electronic properties depend on the supporting metal [195], on Ir(111) (the substrate we used in this work) it exhibits a small gap but is closer to free standing compared to Ru(0001) for instance [196]. Typically on a hexagonal metallic surface with similar lattice parameter, the lattice mismatch induces a Moiré pattern that can be used as a template [101].

Graphene was proven to decouple molecules from the substrate [197], preserve the magnetic properties of single molecule magnets [198], protect single atom magnets from electron and phonon scattering events [12], and allow large magnetic anisotropy in Co adatoms [199]. Graphene also provides a layer to facilitate the formation of ordered molecular structures [200]. A review of the self-assembly of molecules on graphene can be found in reference [201].

Graphene on Ir(111) is grown by chemical vapor deposition. The iridium single crystal is first cleaned with repeated cycles of sputtering at 1200 eV followed by flash annealing (<2 minutes) at 1500 K. The sample is then heated at 1300 K and exposed to a pressure of  $5 \cdot 10^{-7}$  mbar of ethylene for 100 s and then progressively cooled down for 5 min. The surface ends up fully covered by high quality graphene. The Moiré pattern of gr/Ir(111) and the resolved atomic structure are visible in the STM image shown in figure 3.14.

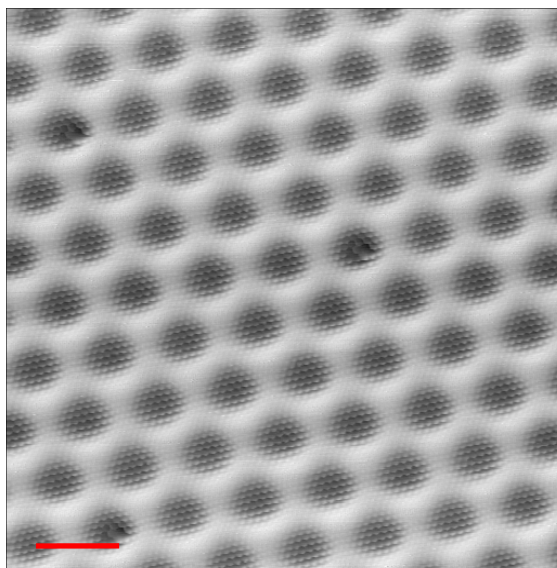


Figure 3.14: STM image of graphene grown on Ir(111). Tunneling conditions:  $V_t = -2$  V,  $I_t = 1$  nA, 5 K, scalebar is 2.5 nm.

#### 3.4.1 BDA

After exposing the gr/Ir(111) sample to a flux of BDA as used in section 3.3.1, several attempts were made at obtaining a clear image of the resulting surface, without success. Reducing the deposition time, and thereby the molecular coverage, resulted in zones of empty graphene with visible Moiré pattern (see upper part of figure 3.15 left), but the tip seemed to frequently drag objects at the surface. The lower part of the left-hand-side of figure 3.15 shows an island of molecules, whose relative orientation appears to be dominated by hydrogen bridges formation. The network is shown in a zoom on the right-hand side of figure 3.15. It is less regular than on Ag(100) (see figure 3.2 upper-left) and tunneling conditions were highly unstable, possibly due to reduced interaction of the molecules with the substrate, meaning that a lot of changes can happen to the junction while imaging. This indicates that deprotonation did not happen, possibly preventing the formation of coordination complexes. This is in agreement with the absence of deprotonation of TPA observed on gr/Ni(111) using XPS [202]. Annealing the sample post deposition to 400 K resulted in the absence of molecules on the surface. We made several attempts to adsorb Tb and BDA onto graphene but all of them led to similar results as in figure 3.15. We conclude that the molecules do not deprotonate up to the desorption temperature, impeding the formation of the intended metal-organic structures. This also indicates that the single Tb adatoms do not deprotonate the carboxyl groups. The fact that deprotonation is inhibited on graphene is attributed to the chemical inertness of graphene compared to the metal substrate.

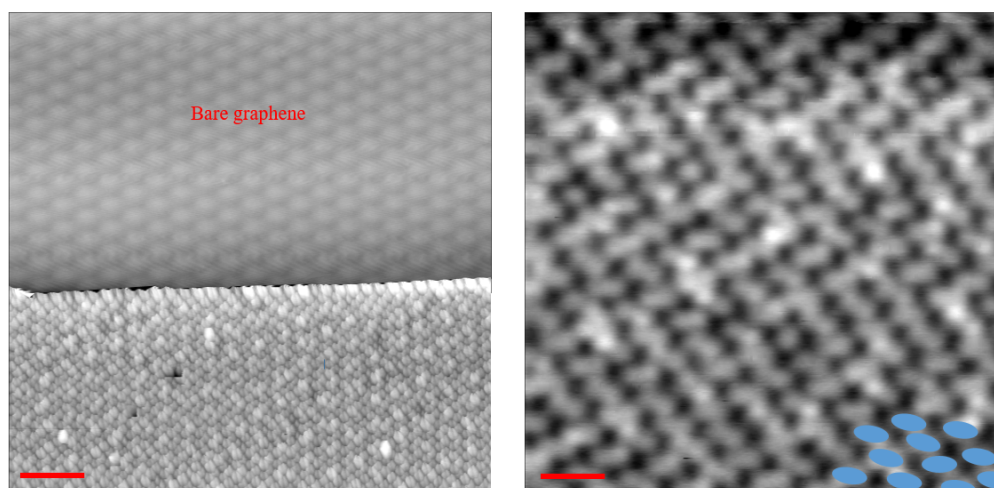


Figure 3.15: Left: STM image of BDA deposited on gr/Ir(111). Tunneling conditions:  $V_t = -1$  V,  $I_t = 40$  pA, 5 K, scalebar is 6 nm. Right: Close up on the BDA network on graphene. Tunneling conditions:  $V_t = -2$  V,  $I_t = 45$  pA, 5 K, scalebar is 3 nm. The blue ellipsoid in inset represent the molecular units.

### 3.4.2 QDC

Figure 3.16 shows a gr/Ir(111) sample exposed to a flux of QDC. A network of molecules appearing as a sort of mixture of the chevron packing of terphenyl-dicarbonitrile on Ag(111) [152] and the close-packing of sexiphenyl-dicarbonitrile on gr/Cu(111) [160] is visible (the two structures are shown schematically on the right-hand-side of figure 3.16). The observed structure is not periodic, since the alternation of double and single rows is irregular. The molecular units are shown on the overlay in the lower right corner of the image. Note that each phenyl ring is distinguishable in the STM image. Generally the tunneling conditions are unstable again possibly due to the low interaction between molecules and graphene surface, meaning that the molecules are moving with the tip and that imaging without changing the surface can be tricky.

The codeposition of Tb and QDC on graphene/Ir(111) produced a metal-organic structure, as seen on figure 3.17. In order to compare the different samples, we define 1 ML of QDC to be the molecular coverage corresponding to the whole surface covered by the structure of figure 3.16 (approximately  $0.75$  molecules/nm<sup>2</sup>). 1 ML of Tb is defined as one Tb atom per graphene unit cell (approximately  $20$  atoms/nm<sup>2</sup>). The left image of figure 3.17 shows an STM image of the codeposition of  $\sim 0.3$  ML of QDC and  $\sim 0.001$  ML of Tb on gr/Ir(111) at room temperature. The right image shows the codeposition of  $\sim 0.15$  ML of QDC and  $\sim 0.001$  ML of Tb at room temperature. These experiments demonstrate that an excess of molecular ligands (left) hinders the formation of more regular structures (right).

We then proceeded to explore the formation of metal-organic structures with other rare earth atoms, improve the coverage and adjust the rare earth atoms to QDC ratio. Figure 3.18 shows



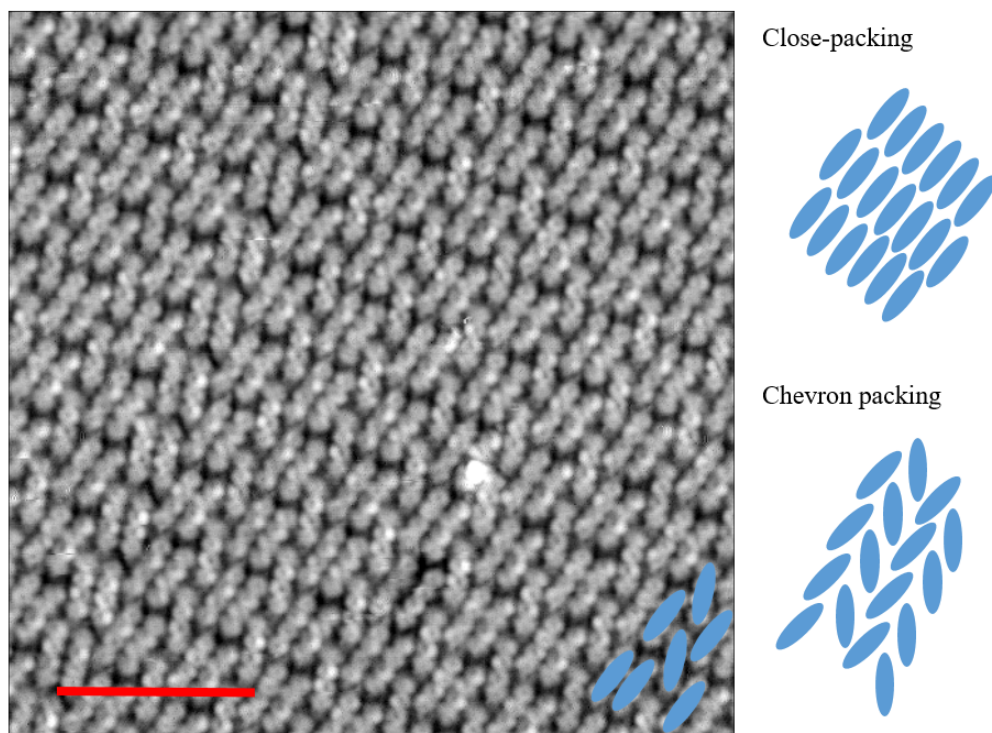


Figure 3.16: STM image of QDC deposited on gr/Ir(111). Tunneling conditions:  $V_t = -100$  mV,  $I_t = 25$  pA, 5 K, scalebar is 6 nm. The insets shows the positions of the molecular units. The side models depict the regular chevron and close packing.

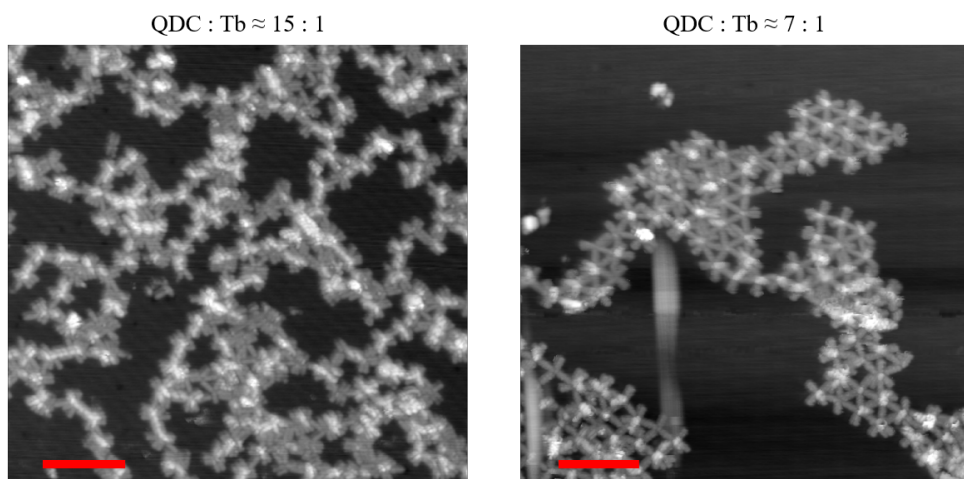


Figure 3.17: STM images of Tb and QDC deposited on gr/Ir(111). Left: 0.3 ML of QDC and 0.001 ML of Tb. Tunneling conditions:  $V_t = -2$  V,  $I_t = 10$  pA, 5 K, scalebar is 11 nm. Right: 0.15 ML of QDC and 0.001 ML of Tb. Tunneling conditions:  $V_t = -2$  V,  $I_t = 50$  pA, 5 K, scalebar is 9 nm.

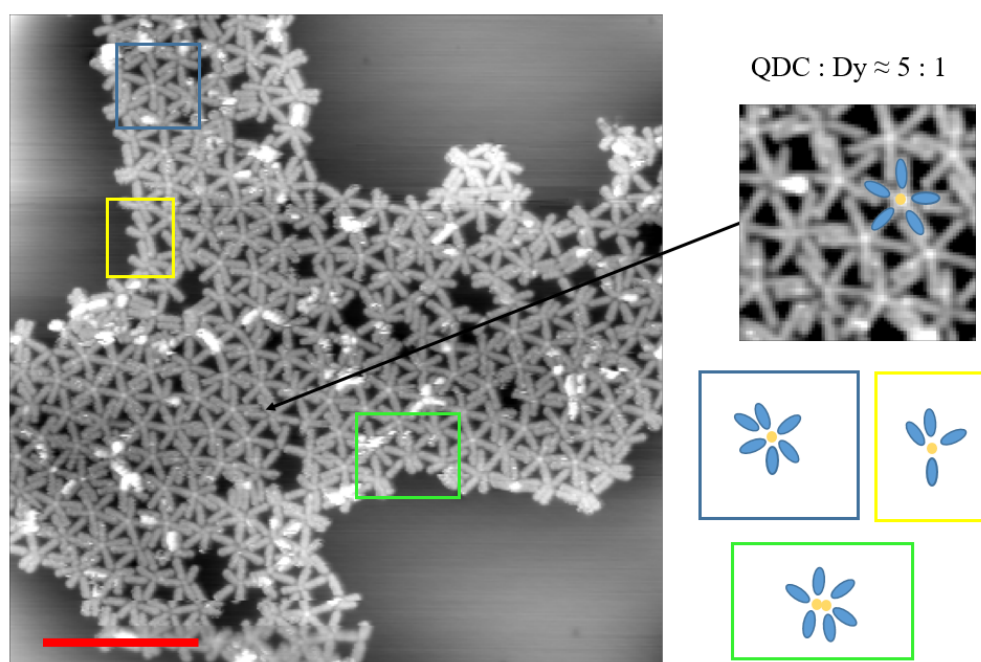


Figure 3.18: STM image of 0.0015 ML of Dy and 0.15 ML of QDC deposited on gr/Ir(111) at room temperature. 30 % of the surface is covered by the metal-organic network. Tunneling conditions:  $V_t = -3.3$  V,  $I_t = 50$  pA, 5 K, scalebar is 12 nm.

a large island of a regular Dy-QDC network. A majority of Dy atoms are coordinated to 5 ligands, with variations being a ligand bound to two Dy atoms, one Dy atom bound to 4 ligands (yellow square), or a binuclear metal node surrounded by six ligands (green square). A sixth molecule (blue square) can also be close to the metal centers, but actually does not bind to the Dy atoms. All these minority configurations are depicted on the side of the image. The binuclear complex and presence of the sixth, detached carbonitrile ligand are also reported for Dy-BCNB/gr/Ir(111) in reference [142]. In the ideal situation, where 100 % of the surface is covered by such islands, one would reach 0.5 ML of QDC and 0.005 ML of Dy. Here approximately 30 % of the surface is covered.

On one of the samples, during the preparation of which the 5:1 ratio was approximately conserved, another coordination complex was observed, shown in figure 3.19. In this structure there seem to be 6 ligands per Dy but only four really bind to the rare earth. We did not manage to reproduce the structure by adjusting the metal:molecule ratio. The island is trapped between two ascending steps. It could be that the presence of steps modified locally the self-assembly process.

The 5:1 network was also synthesized with Er coordination centers. The coverage was increased to approximately 70 % of the surface. A large scale image of the network is shown in figure 3.20. The magnetic properties of Er- and Dy-QDC/gr/Ir(111) are analyzed with X-ray synchrotron experiments in the next chapter of this thesis.

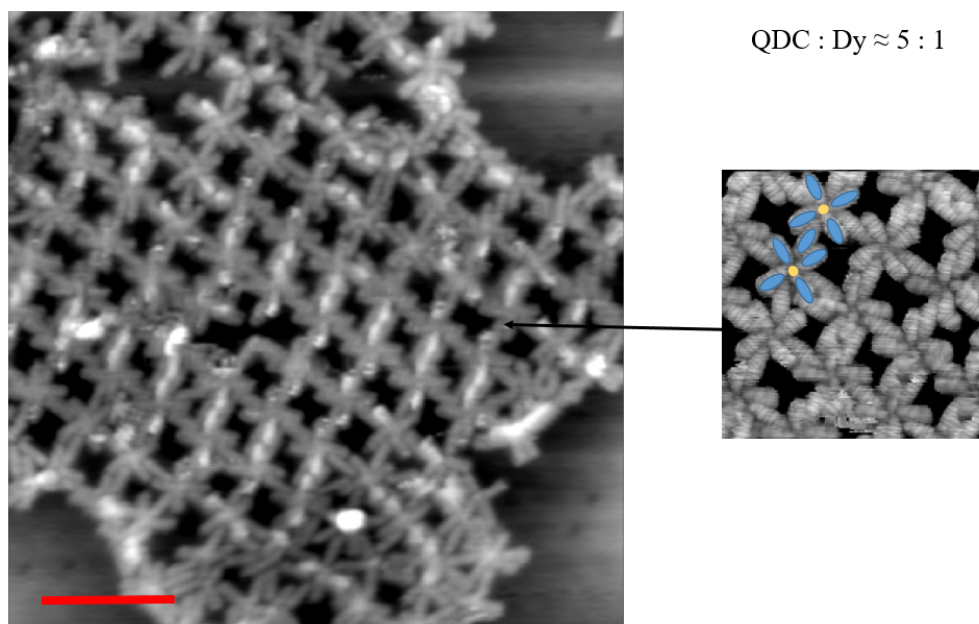


Figure 3.19: STM image of 0.001 ML of Dy and 0.1 ML of QDC deposited on gr/Ir(111) at room temperature. The structure is embedded between two ascending steps. Tunneling conditions:  $V_t = -3.3$  V,  $I_t = 50$  pA, 5 K, scalebar is 9 nm.

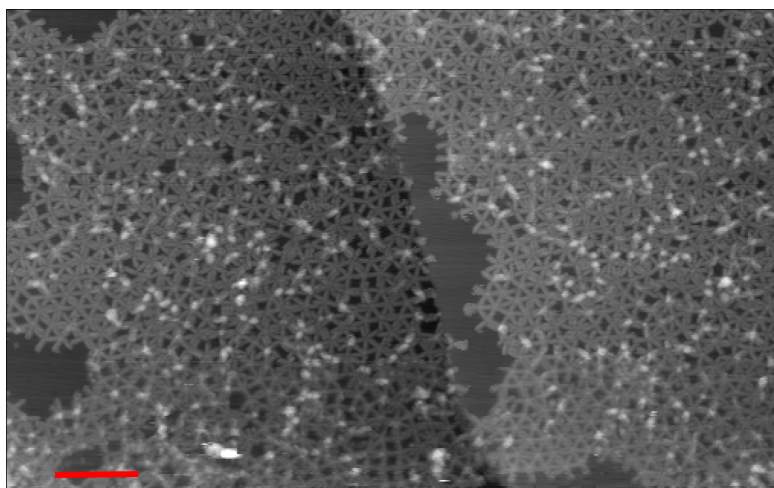


Figure 3.20: Large scale STM image of the  $\sim$ 5:1 structure covering approximately 70% of the graphene surface. Tunneling conditions:  $V_t = -2.8$  V,  $I_t = 28$  pA, 5 K, scalebar is 13 nm.



### 3.4.3 ZnTPyP

ZnTPyP molecules were deposited on gr/Ir(111) at room temperature without subsequent annealing. Figure 3.21 shows the molecular network on gr/Ir(111). The tunneling conditions are highly unstable and the appearance of ZnTPyP varies with changes in the tunnel junction (see also figure 3.22, left). The molecular structure with larger apparent height is interpreted as a second molecular layer. Bilayers of Co-TPP were also reported on Ag(111) [203].

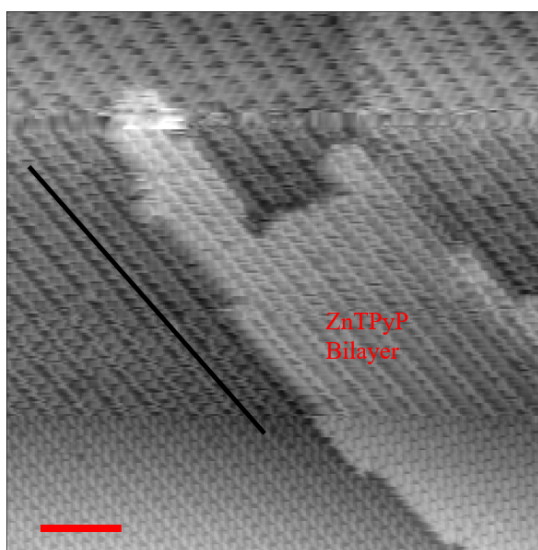


Figure 3.21: STM image of ZnTPyP deposited on gr/Ir(111). Tunneling conditions:  $V_t = -2.3$  V,  $I_t = 100$  pA, 77 K, scalebar is 10 nm. The black line indicates the direction of equivalent molecular units (same as figure 3.4)

Figure 3.22 shows STM images of the codeposition of Tb and ZnTPyP. Deposition at room temperature does not result in coordinated Tb atoms. Annealing before the Tb deposition removes all bilayers and some coordination structures are formed upon Tb deposition. The rhombic arrangement is seen on the corner of the island (large red rectangle on figure 3.22) with a few coordinated complexes within the molecular network indicated by smaller red squares. Increasing the quantity of terbium, or annealing the sample following the Tb deposition, aiming at a large portion of the surface covered by metal-organic complexes, only resulted in an increased number/size of clusters with minimal improvement, making the system unsuitable for ensemble measurements.

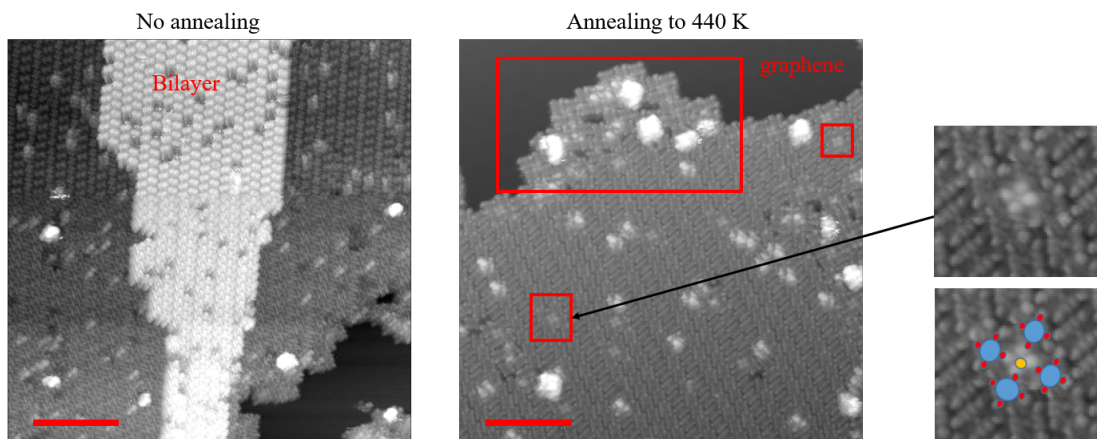


Figure 3.22: STM image of Tb and ZnTPyP deposited on gr/Ir(111). Left: deposition at room temperature, no annealing. Tunneling conditions:  $V_t = -2.0$  V,  $I_t = 60$  pA, 77 K, scalebar is 16 nm. Right: deposition at room temperature, followed by annealing to 440 K. Tunneling conditions:  $V_t = -2.5$  V,  $I_t = 50$  pA, 5 K, scalebar is 15 nm.

### 3.5 Summary

Table 3.1 shows a summary of all systems that we investigated. The NaCl substrate is not inert enough and tends to be dissolved by the BDA and QDC ligands. We did not deposit ZnTPyP on NaCl but expect similar coordination to Na atoms. The MgO exhibits strikingly different behaviours between the nitrogen-terminated ligands and the carboxylate-terminated ones: the nitrogen-terminated molecules show little adherence to the MgO surface whereas the carboxylate-terminated ligands showed strong interaction with little place for metal-organic coordination. Finally, graphene excluded the BDA ligand, as its catalytic power is insufficient for deprotonation. Although less convenient than on metallic surfaces, graphene seems to allow for the formation of metal-organic coordination structures with the nitrogen terminated ligands ZnTPyP and QDC. If they exist, the experimental parameters for a recipe giving large regular patches of a RE-ZnTPyP network are too narrow. RE-QDC form a metal-organic network with sufficient surface coverage and homogeneity to be investigated by spatially integrating techniques. The analysis of X-ray absorption measurements carried out on that system is the subject of the next chapter.

### 3.5 Summary

	NaCl/Ag(100)	MgO/Ag(100)	gr/Ir(111)
BDA	× Binds with Na	× No interaction with RE	× No deprotonation
ZnTPyP	(×) Probably binds with Na	× No surface adsorption	~ Narrow param. (440 K ann.)
QDC RT preparation	× Binds with Na	× No surface adsorption	✓ Coordination structure

Table 3.1: Summary of the ligand/substrate combinations.



## 4 Magnetic properties of metal-organic coordination complexes

X-ray absorption investigations of the metal-organic structures formed by rare earth atoms and QDC on graphene /Ir(111) were carried out at the X-Treme beamline [52]. The growth is described in section 3.4.2 of the previous chapter. Preliminary results on the analysis of the X-ray data are reported in this chapter.

In the gas phase, most rare earths are in the so-called divalent state: two electrons are in the  $5d6s$  shells and the  $4f$  occupation is noted  $4f^n$  (see figure 1.1). When embedded in a more strongly interacting environment, a third electron is often promoted from the  $4f$  to the  $5d6s$  shells, the  $4f$  occupancy becomes  $4f^{n-1}$  and the atom is said to be trivalent. The valence state of the rare earths on surfaces is determined by the hybridization with the environment and the binding energy, the promotion energy for a  $4f$  electron to the  $5d6s$  shell, and the intershell coupling [204].

Once the valency is set, we can determine the lowest multiplet  $J$  with Hund's rules and look at the effect of the ligand field as perturbations. In reference [64], it is shown that the shape of the  $4f$  charge distribution in a given crystal field can provide a way of determining which  $m_J$  will be favored along a given axis. The relative energy of the states within the lowest multiplet can then be rationalized with a qualitative estimation of the Coulomb repulsion between the electrons of the  $4f$  shell and the electrons of the ligands, meaning how well does the  $4f$  electrons spatial distributions 'fit' in the ligand field. The relevant distinction is whether the charge distribution is i) approximately spherical; ii) prolate (elongated along the  $z$ -axis), in which case it will strongly repel with an axial ligand field; iii) oblate (flat), where equatorial coordination will have larger repulsion.

The elements that we have investigated so far in the QDC metal-organic networks are Er and Dy, both in trivalent state ( $4f^{11}$  and  $4f^9$ , respectively). As a rule of thumb, for  $\text{Er}^{3+}$  the maximum  $m_J = 15/2$  is prolate and is the preferred state in an equatorial ligand field in SIM [205–208], while for  $\text{Dy}^{3+}$  the maximum  $m_J = 15/2$  is oblate and it is favored in axial crystal fields [11, 60, 209]. As an example, consider the inversion of the respective energetic ordering of the  $m_J$  states of  $\text{Er}^{3+}$  and  $\text{Dy}^{3+}$  depending on whether the ligand field is mostly equatorial as

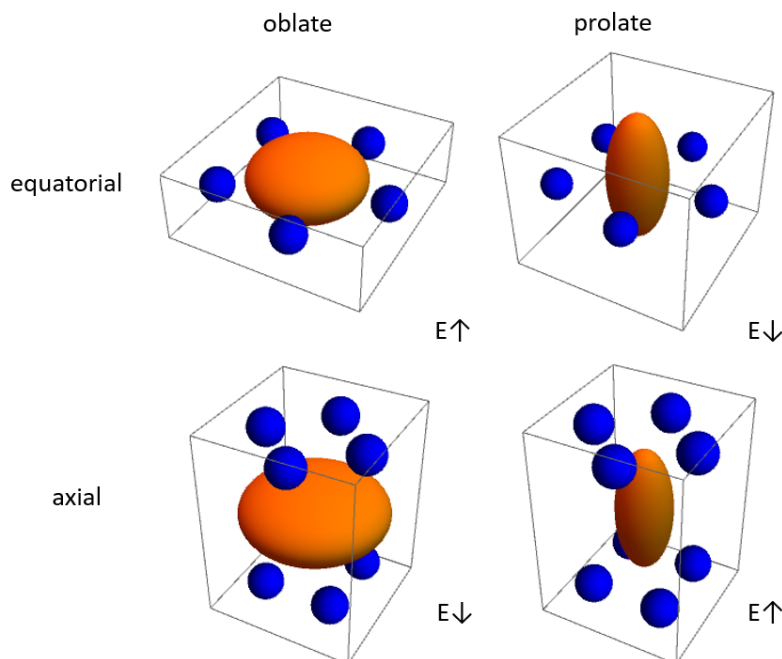


Figure 4.1: Illustration of the asphericity of the  $4f$  charge distribution. The  $4f$  charge distribution is pictured by the orange ellipsoid and the ligands are represented by the blue spheres. A prolate ion will have a lower energy ( $E \downarrow$ ) in an equatorial crystal field. Inversely, in an axial field the ion with oblate charge distribution will be able to occupy the free space minimizing the Coulomb repulsion with the ligands.

in reference [205] or axial [60]. This approach is illustrated in figure 4.1, where the effect of the asphericity of the  $4f$  distribution on the Coulomb repulsion with neighboring point charges is shown. The equatorial ligand field represents the laterally fivefold coordinated ion in the Ln-QDC network and the axial field represents an ion vertically bound in a phthalocyanine double decker.

In this chapter we investigate the effect of equatorial carbonitrile ligands on Er and Dy.

## 4.1 Experimental

The Ir(111) crystals are cleaned with successive cycles of sputtering (1.2-2 keV) and annealing (1400 K, 5 min). Graphene is then grown by heating the sample to 1350 K in a pressure of  $7 \times 10^{-7}$  mbar of ethylene for 100 s and cooling it down to 300 K in approximately 5 min. The graphene surface is then exposed to a Kentax effusion cell, containing a molecular powder of QDC, heated at 450 K while the sample is kept at room temperature (deposition time = 15 min, leading to approximately 70 % of the surface covered by the structure). The sample is then transferred to the XAS chamber and the rare earths (Dy, Er) are deposited from high purity rods with an  $e$ -beam evaporator and the sample kept at room temperature, before cooling it to

2.5 K and starting the X-ray absorption measurements. A sample, with coverage determined with STM at EPFL, was brought to PSI to calibrate the coverages of the samples grown at PSI. 1 ML on Dy is defined as one Dy atom per graphene unit cell and 1 ML of molecules is defined as the quantity of QDC that would cover the whole surface with the structure of figure 3.16. The optimal Dy/Er coverage should be approximately 0.005 ML and the optimal QDC coverage (probed at the nitrogen *K* edge) is 0.5 ML. With these coverages for QDC and RE the ratio QDC:RE is 5:1 and the surface is fully covered of a coordination complex made mostly of subunits of 5 QDC ligands for 1 rare earth atom (the second CN per QDC group is not bound to a rare earth atom).

The X-ray absorption signal is acquired in total electron yield mode (see section 2.2.2). All experimental spectra underwent background subtraction. The XAS are the sum of the right  $\sigma^+$  and left  $\sigma^-$  circular polarized absorption spectra and the XMCD is their difference, both recorded at a magnetic field of 5.5 T oriented parallel to the incoming photon beam. The XMLD spectra, acquired in grazing  $\theta = 60^\circ$  incidence ( $\theta$  is measured with respect to the surface normal), represent the difference between the vertical  $\sigma_v$  and horizontal  $\sigma_h$  linear polarization absorption spectra. The magnetization curves are acquired by recording the XMCD signal at an energy corresponding to maximum of the  $M_5$  absorption edge (indicated by a black arrow on each XMCD spectrum) while sweeping of the magnetic field at a rate of 2 T/min across the -6.8 T to 6.8 T range in grazing and normal incidence.

Atomic multiplet calculations to simulate the spectra are performed with the multiX software [78]. The main inputs are the electronic structure of the element and a list of point charges distributed in space, mimicking the crystal field.

## 4.2 Dy-QDC network

### 4.2.1 Dysprosium on surfaces

On many metallic substrates, Dy takes on a divalent configuration ( $4f^{10}$ ). It is trivalent on Pt(111) and divalent on Cu(111), Ag(100) and Ag(111) due to a relatively large promotion energy (energy required to promote a  $4f$  electron to the  $5d$  shell) [204]. The energy of the magnetic moment of Dy is roughly isotropic on these metal surfaces [204], there is a small in-plane anisotropy in clusters on Cu(111) where atoms become trivalent, and acquires a stronger in-plane anisotropy when single Dy ions are coordinated with carboxylate terminated ligands on Cu(111) [210]. Dy adsorbed on top of oxygen atoms on MgO/Ag(100) is a single atom magnet with out-of-plane anisotropy; its  $4f$  occupation depends on the film's thickness,  $4f^9$  being the most stable magnet [13, 173]. On graphene/Ir(111), Dy is divalent and is also a single atom magnet with long relaxation time of the order of at least 1000 s at 2.5 K and out-of-plane easy-axis [12, 211]. Dy was shown to favor five-fold coordination on graphene with carbonitrile terminated ligands in reference [142]. However, so far there is no report on the magnetic properties of Dy in such networks.

### 4.2.2 Results

Figure 4.2 shows the results of the X-ray absorption measurements at the Dy  $M_{4,5}$  edges for the network formed by Dy and QDC at the X-Treme beamline [52]. The shape of the XAS is indicative of a  $4f^9$  configuration [50]. The comparison of the XMCD and the magnetization curves in grazing and normal incidence shows a clear easy-plane magnetization parallel to the surface, as the XMCD signal at  $\theta = 0^\circ$  is smaller than the one at  $\theta = 60^\circ$ . The shape of the XMLD points towards a distribution of the  $4f$  charges that is prolate with respect to the axis normal to the surface, as opposed to the XMLD of  $\text{Dy}^{3+}$  with normal easy-axis, shown in reference [212]. Indeed the sign of the XMLD signal is dependent on the easy-magnetization axis as shown in appendix B and discussed further in the next sections, where the relationship between easy-axis, charge distribution and XMLD are explained. Finally, the magnetization curves acquired in grazing and normal incidence confirm the in-plane anisotropy and the fact that they are closed reveals the absence of hysteretic behavior within our experimental time resolution.

Multiplet simulations were carried out to gain further insight into the static properties of the system. We tried to reproduce the shape of all the spectra as well as the in-plane easy magnetization. For this, a crystal field with five equidistant surrounding charges representing the Dy-NC bonds, and one central charge below the  $\text{Dy}^{3+}$  atom are tried to fit the XAS, XMCD, XMLD, and magnetization curves. The comparison of the XAS of different pure  $m_J$  states of  $\text{Dy}^{3+}$  given in appendix in figure B.1 with the experimental XAS indicates a ground state that is between  $m_J = 3/2$  and  $m_J = 9/2$ . The crystal field given in figure 4.3 reproduces nicely the experimental results: all simulated spectra are shown in figure 4.2 (b), (d), (f), and the energy level scheme is shown in (h). As the symmetry axis of the equatorial ligands and the surface is normal to the surface, the projection along the  $z$ -axis normal to the surface is the most informative. The purer states with  $\langle J_z \rangle = \pm 7.44$  and  $\langle J_z \rangle = \pm 6.23$  are pushed to higher energy. The rest of the states are fairly mixed, below 50 meV. The ground state has  $\langle J_z \rangle = \pm 1.26$ . There are small differences between the simulated and measured spectra. Some uncertainty in the experimental data comes from the fact that the X-ray acquired backgrounds in the absence of Dy atoms were unsuitable for use: they did not match the backgrounds observed during the measurements of the spectra, meaning that change occurred between the background measurement and spectra acquisition. Backgrounds were interpolated before subtraction. The analysis is also preliminary and the existence of a better fitting crystal field is not excluded.



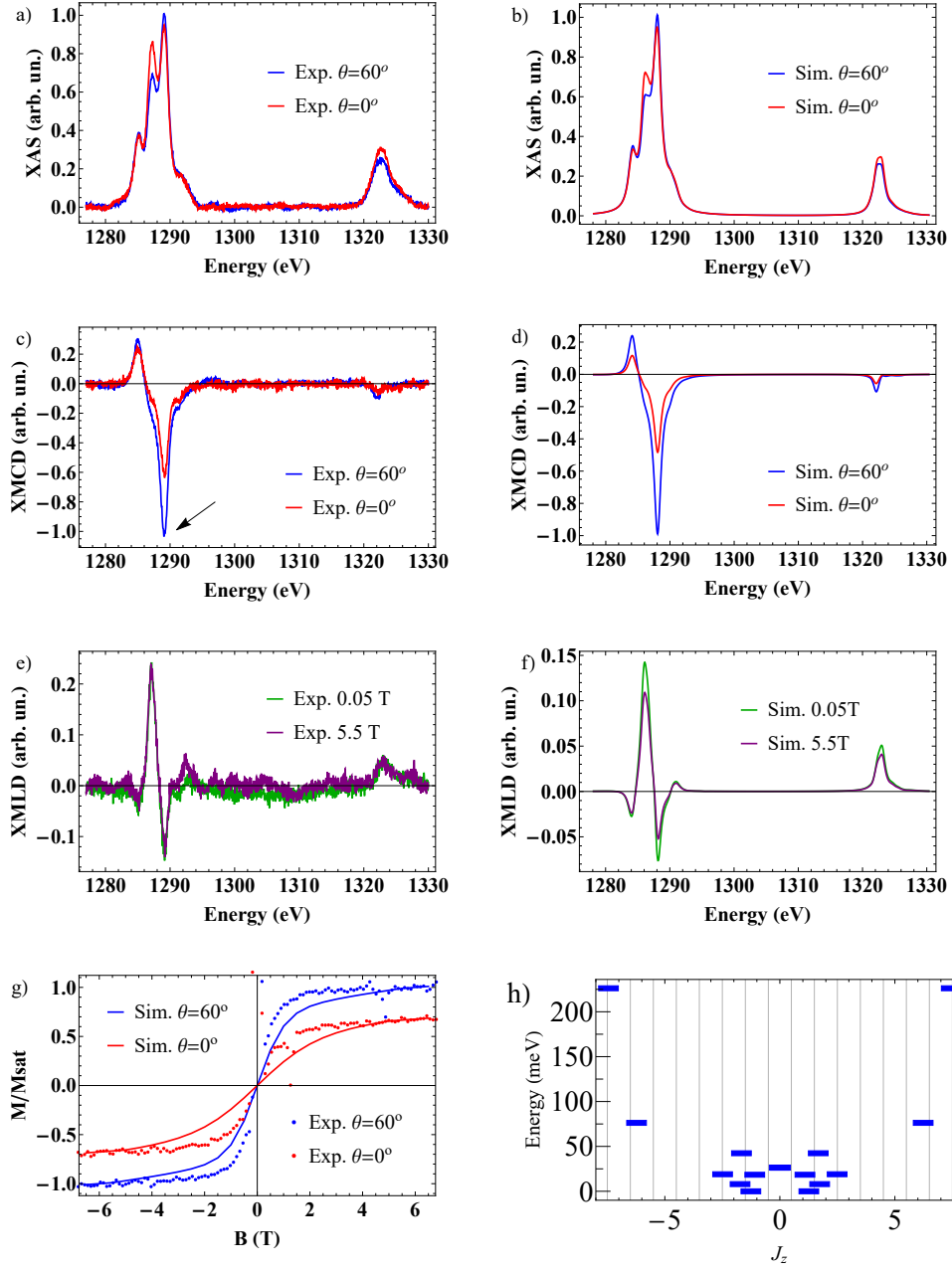


Figure 4.2: XAS (a,b) and XMCD (c,d) at 5.5 T, XMLD (e,f) at the indicated fields (parallel to the incident X-rays) of 0.5% ML Dy and 0.5 ML QDC in a Dy-QDC metal-organic structures at the  $M_{4,5}$  edges of Dy. The QDC and Dy coverages are close to the optimal ones, and roughly the entire surface is covered by the metal-organic network. g) Magnetization curves acquired with a sweeping-rate of 2 T/min (photon flux:  $4 \times 10^{-2} \text{ nm}^{-2} \text{ s}^{-1}$ ). The black arrow in (c) indicates the peak at which the magnetization curves have been acquired. All spectra are acquired/simulated at 2.5 K.

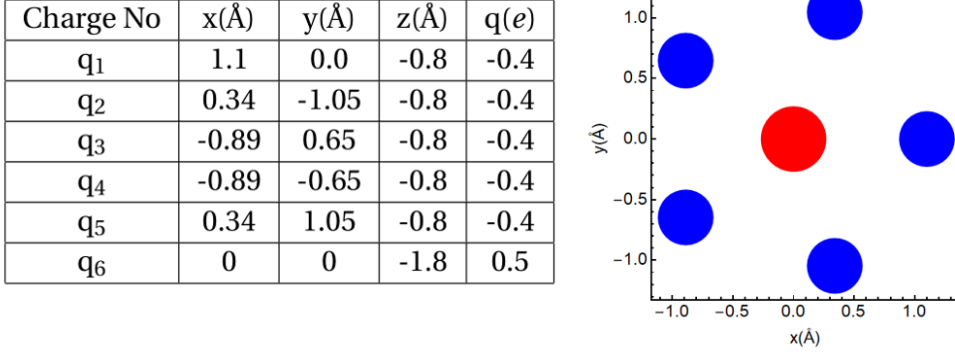


Figure 4.3: Spatial distribution of the charges around the dysprosium atoms. In the planar representation, red corresponds to positive and blue to negative charge; the size reflects the amount of charge.

### 4.3 Er-QDC network

#### 4.3.1 Erbium on surfaces

Erbium single atoms on metallic surfaces are trivalent ( $4f^{11}$ ) on Cu(111), Pt(111) and Ag(100), with large in-plane easy magnetization on Cu(111) contrasted with the out-of-plane easy-axis on Pt(111)[204, 213]. This was attributed to the  $4f$  charge distribution of states of the  $J = 15/2$  multiplet that is more oblate for small  $m_J$  and prolate for  $m_J = \pm 15/2$  (more on this in section 4.4). On Pt(111), the local density of states close to the Fermi level is dominated by the  $5d$  orbitals, responsible for localized and directional ligand field favoring the prolate charge distribution. In contrast, on Cu(111) the  $4s$  delocalized and isotropic (within the plane) states are more relevant to the local density of states on the surface, leading to a roughly flat charge density of the surface, favoring an oblate charge distribution. Erbium trimers are also known to exhibit magnetic hysteresis with out-of-plane easy axis on Cu(111), making them the smallest known bistable magnets on a metallic substrate [133], together with Fe trimers [132]. Erbium on graphene/Ir(111) is divalent ( $4f^{12}$ ) with  $J = 6$  as the lowest energy multiplet [211]. It has a strong in-plane anisotropy. Er single ion magnets were also self assembled on supported graphene where they align their easy magnetization axis perpendicular to the surface [200].

#### 4.3.2 Results

The Er-QDC coordination complex was investigated with X-ray spectroscopy of the  $M_{4,5}$  edges. Figure 4.4 shows the experimental results. The coverage is defined as for Dy. The XAS is consistent with a  $4f^{11}$  electronic configuration of  $\text{Er}^{3+}$  with total angular momentum  $J = 15/2$ . From the XMCD spectra at grazing ( $60^\circ$ ) and normal incidence we deduce a significant out-of-plane anisotropy at 5.5 T. The XMLD spectra are discussed in section 4.4. The magnetization

curve confirms the out-of-plane anisotropy but no hysteresis was detected, indicating a paramagnetic behavior.

We tried to reproduce the experimental spectra with multiplet simulations using a crystal field similar to the Dy one. Simulations confirm the  $4f^{11}$  configuration of Er adatoms. Looking at the XAS of different pure  $m_J$ , shown in figure B.2 of the appendix, we deduce a ground state dominated by  $m_J = \pm 13/2$  and  $m_J = \pm 11/2$ . The crystal field in figure 4.5 generates the level scheme of figure 4.4 (h). All spectra are in good agreement with experiments. The crystal field is more axial than for Dy, leading to states closer to the pure  $m_J$  ones. The obtained ground state has a total angular momentum of  $\langle J_z \rangle = \pm 6.42$ . Again there are small differences between the measured and simulated spectra. An additional source of discrepancy can possibly be attributed to the presence of Er atoms in different coordination environments.

### 4.3.3 Note on the point charges

Initially the charge configurations for simulation were chosen to represent as faithfully as possible the five nitrogen ligands and the underlying surface. Starting from there no acceptable fit to the experimental data was found. The condition of perfectly equatorial charges distributed in the same plane as the ion was then relaxed to allow for better adjustability of the energy level scheme for Dy. The ligand field fitting for Dy did not reproduce at all the experimental data of Er, this was already observed for instance for a variety of lanthanides on gr/Ir(111) [211], therefore we considered the two point charge distributions independently. As a consequence the point charges are rather taken as parameters for the simulations and no further information is inferred from their configuration.

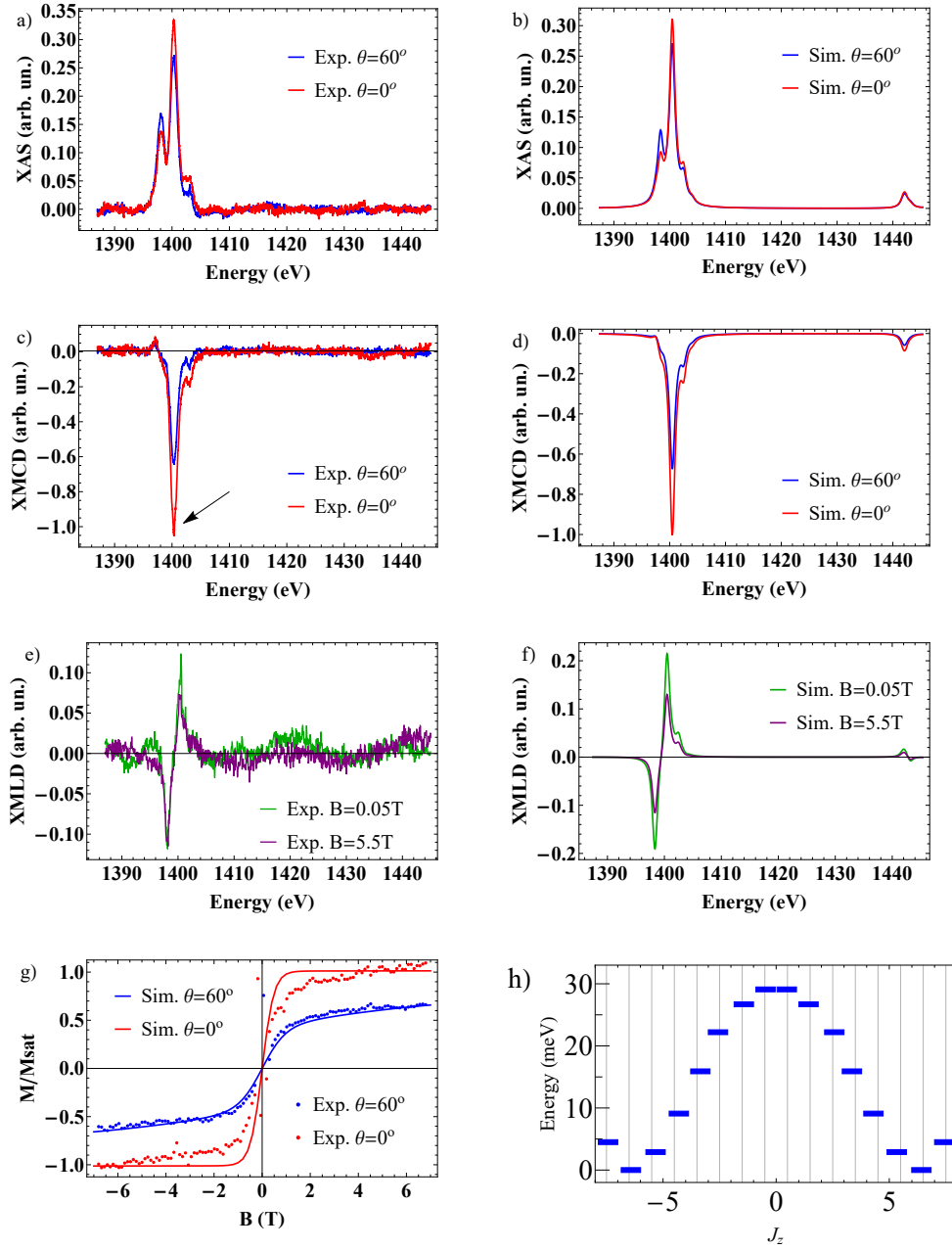


Figure 4.4: XAS (a,b) and XMCD (c,d) at 5.5 T, XMLD (e,f) at the indicated fields (parallel to the incident X-rays) of 0.4% ML Er and 0.5 ML QDC in a Er-QDC metal-organic structure at the  $M_{4,5}$  edges. Approximately 80 % of the surface is covered by coordinated Er. g) Magnetization curve acquired with a sweeping-rate of 2 T/min (photon flux:  $2.2 \times 10^{-2} \text{ nm}^{-2} \text{ s}^{-1}$ ). The black arrow in (c) indicates the peak at which the magnetization curves have been acquired. All spectra are acquired/simulated at 2.5 K.

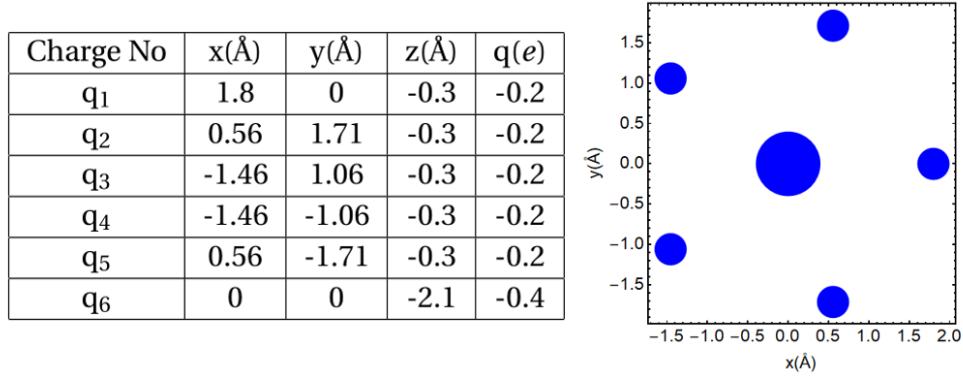


Figure 4.5: Spatial distribution of the charges around the erbium atoms. In the planar representation, blue corresponds to negative charges; the size reflects the amount of charge.

#### 4.4 Discussion

The energy of the pure  $m_J$  states in crystal fields can be rationalized by looking at the asphericity of the  $4f$  charge distributions of the  $J = 15/2$  multiplets of Dy and Er [64]. This information is contained in the angular part. Oblate states will undergo more Coulombic repulsion with equatorial neighbors, whereas prolate states will fit in an equatorial ligand field. Using the data of reference [214] we reproduced those angular distributions. The angular part of the  $4f$  charge distributions of trivalent Er and Dy are shown in figure 4.6.

Plotting the angular dependence  $\rho_{\theta,\phi}$  of the  $4f$  charge distribution clearly shows whether some states are prolate or oblate. For example, for Dy,  $m_J = 15/2$  is obviously oblate. However, for Er some of the angular distributions are harder to characterize by eye. For this reason, we tried to find a simple way to quantify the prolate vs. oblate nature of the  $4f$  orbitals. Assuming an unchanged radial charge distribution  $\rho_r$  of the  $4f$  shell from figure 2.7, we can compute the center of the electronic charge density in one octant (or equivalently one quadrant) due to the full rotational symmetry around the  $z$ -axis. The angle  $\alpha$  between the center of charge's position  $(\mu_x, \mu_z)$  and the  $z$ -axis indicates whether the charges are more distributed in the  $z$ -direction or in the  $xy$ -plane. This angle is defined as:

$$\alpha = \arctan \frac{\mu_z}{\mu_x}, \quad \text{where } \mu_j = \int_{x>0, y>0, z>0} j \rho(\mathbf{r}) dV, \quad j \in \{z, x\} \quad (4.1)$$

where  $\rho(\mathbf{r}) = \rho_r(r) \rho_{\theta,\phi}(\theta, \phi)$  is the electronic charge density. An angle of  $\pi/4$  corresponds to a spherical distribution of charges. An angle  $\alpha > \pi/4$  means that the charges are more distributed along the  $z$ -axis, corresponding to a prolate charge distribution. Conversely, an angle  $\alpha < \pi/4$  characterizes a charge distribution that is more spread in the  $xy$ -plane, i.e. that is oblate. See figure 4.7 for an illustrative example with the obviously oblate  $m_J = 15/2$  state of  $\text{Dy}^{3+}$ . The charge density is the product of the angular distribution identified by the red line

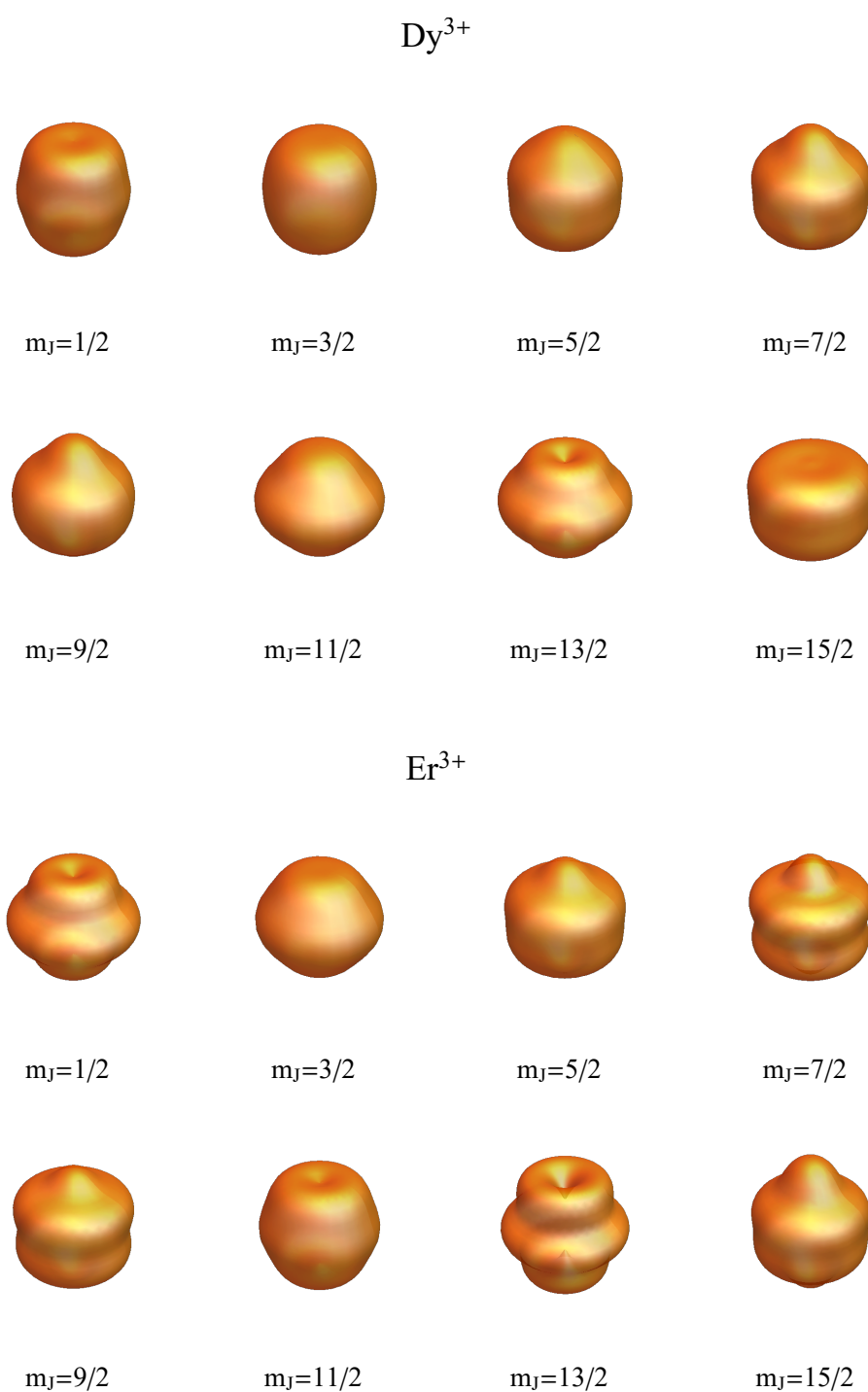


Figure 4.6: Angular dependence of the  $4f$  charge distribution of the different  $m_J$  states of the  $J = \frac{15}{2}$  multiplet of  $\text{Dy}^{3+}$  and  $\text{Er}^{3+}$ . Computed from reference [214].

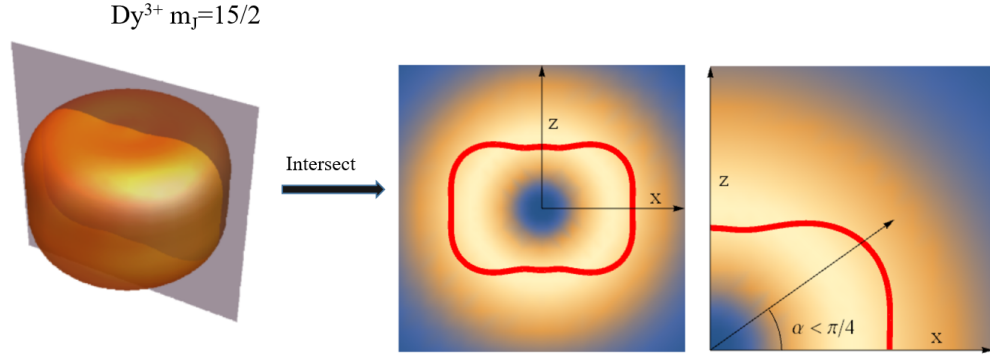


Figure 4.7: Computation of the average charge position for the most oblate  $m_J = 15/2$  state of  $\text{Dy}^{3+}$ . The thick red line represents the intersection of the angular part of the charge distribution with the  $xz$ -plane. The background color represents the radial part of the charge distribution (blue corresponds to zero electron density).

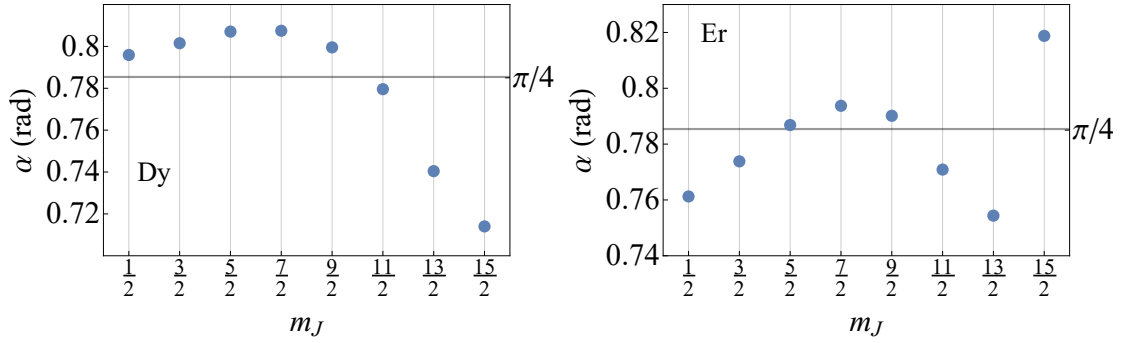


Figure 4.8: Value of the angle  $\alpha$  between the dipole moment and the  $z$ -axis for all  $m_J$  states of Dy and Er. The horizontal line is at  $\pi/4$ .

and the radial density shown as color gradient in the background.

The next step is to compute  $\alpha$  for all eigenstates of  $J_z$  for Er and Dy. The value of the angle for each  $m_J$  is given in figure 4.8. For Dy, all  $m_J < 11/2$  are slightly prolate. The other three states are oblate with a pronounced deviation from the spherical distribution in  $m_J = 13/2$  and  $m_J = 15/2$ . For Er, the situation is a bit more complicated but  $m_J = 15/2$  is clearly prolate and  $m_J = 1/2$  and  $m_J = 13/2$  seem to be more oblate. Note also that since the XMLD depends on the difference in charge spatial distribution in the two polarization directions, the XMLD spectra corresponding to the different  $m_J$  could reflect this change in angle. Indeed figure B.3 of the appendix shows an inversion in the shape of the XMLD spectrum for Dy as soon as  $\alpha$  crosses  $\pi/4$ . However, we do not observe such correlation in the variation of the XMLD spectra of Er as seen in figure B.4. The observed inversion of the Er spectra seem to be correlated with the magnitude of  $m_J$  rather than with  $\alpha$ .

The large deviation of  $\alpha$  from  $\pi/4$  for  $m_J = 13/2$  and  $m_J = 15/2$  of the Dy states is consistent with the energy level scheme of figure 4.2 (h) where the two states are pushed to energies

much higher than the other states. As expected, the equatorial coordination of Dy with the CN ligands does seem to favor the more prolate configurations, as a ground state with  $m_J > 11/2$  was excluded by analyzing the XAS spectra.

For Er, the highly prolate  $m_J = 15/2$  state did not appear to be the most favorable configuration. While one can still argue that the equatorial charges push the oblate low  $m_J$  to higher energy, the oblate  $m_J = 13/2$  ground state appears in contradiction with our simple approach consisting in identifying the charge distribution that minimizes the Coulomb repulsion. It could be that the substrate contributes non-negligibly to the electrostatic interactions, as the extremity of the  $4f$  charges of the  $m_J = 15/2$  state points outwards with respect to the origin (see figure 4.6), whereas the  $m_J = 13/2$  points inwards. Indeed, such details of the charge spatial distributions are not necessarily well captured by their parametrization via the angle  $\alpha$ .

We observe the inversion of the easy magnetization axis compared to single atoms on graphene, for both Dy and Er. The graphene surface offers an axial crystal field, that favors oblate states for both species and corresponds to in-plane easy-axis of magnetization for Er and to out-of-plane one for Dy [12, 211]. Addition of equatorial strong CN ligands changes the orientation of the easy-axis for both species. Note however, that ligands cannot be treated as fully equatorial and the surface needs to be taken in account, as, for example, the  $m_J = 15/2$  state of Er does not become the ground state. Overall, the effect of the five nitrile ligands appears to be comparable to the equatorial nitrogen in the single molecule magnets of reference [205] compared to the effect of axial crystal field of phthalocyanine double deckers [60] and metallocenes [215].

In this chapter, control of rare earth's easy-axis and anisotropy was achieved. The prolate/oblate nature of lanthanides charge distribution proved useful in this context. The results are still preliminary and could be bolstered with additional measurements. Confirmation of the trend could be provided for example with Tb centers, that should behave similarly to Dy, and with Tm, that should be affected by the carbonitrile ligands in the same way as Er. Although the magnetization loops are closed, spin-polarized STM investigations of the systems could be performed to see if spin-flip events are detectable. Indeed, the secondary electrons generated by the X-ray photons are known to affect the spin dynamics in XMCD measurements, so the present data do not necessarily exclude hysteretic behavior of the intrinsic system, i.e. without the perturbation of secondary electrons. The experimental sweeping rate also puts a lower bound to the detectable lifetime. For instance, despite being photon-limited, the Dy/NaCl system exhibits hysteresis using the same sweeping rate as here. Finally, the simple approach considering the shape (prolate/oblate) of the charge distribution is useful but does not account completely for the magnetism of the lanthanides in these systems. DFT studies can shed additional light on the magnetic properties of the Dy and Er atoms, as evidenced by studies of Dy and Er containing single molecule magnets [216–218].



## 5 Magnetic properties of rare-earth adatoms on NaCl thin films

As highlighted in chapter 2, single atom magnets undergo thermal diffusion when the temperature increases. For instance, on MgO Ho adatoms move from top-O to bridge adsorption sites at around 50 K [17]. It is therefore possible that the bistability of Ho adatoms is preserved above 50 K, provided that they are stabilized on the top-O site. This structural instability of single atom magnets was the main motivation of this thesis and we attempted to solve it with metal-organic networks incorporating the rare earth atoms in an immobile manner. A second attempt to obtain higher thermal stability of single atom magnets is the use of a different substrate with similar decoupling properties as MgO or graphene, but with a higher diffusion barrier for the species of interest. Here we address NaCl as such a decoupling layer and investigate with Ho, Dy, and Gd three RE atoms as candidates for single atom magnets. The use of NaCl as decoupling layer for single atom magnets has not been investigated yet. Due to its similar nature to MgO, NaCl also opens ways for comparison with the known Ho and Dy single atom magnets [1, 13]. This chapter is based on a manuscript currently in preparation for publication.

**Authors:** S. Reynaud, M. Pivetta, A. Singha, R. Baltic, F. Donati, F. Patthey, L. Persichetti, P. Gambardella, M. Blanco-Rey, A. Arnau, F. Delgado, S. Rusponi, and H. Brune.

**Author contribution:** H. Brune and S. Rusponi conceived the experiment. M. Pivetta, A. Singha, R. Baltic, F. Donati, L. Persichetti, P. Gambardella and S. Rusponi gathered the x-ray data. S. Reynaud and F. Patthey carried out the STM measurements. S. Reynaud carried out the analysis of all the data. M. Blanco-Rey, A. Arnau and F. Delgado performed the DFT calculations and wrote the DFT paragraphs. S. Rusponi and H. Brune supervised the project. At this stage, S. Reynaud, M. Pivetta, S. Rusponi and H. Brune contributed to the manuscript.

### 5.1 Introduction

Rare earth (RE) atoms adsorbed at surfaces [1, 12, 13, 98, 173] or in single ion molecular magnets [11, 14, 65, 219, 220] are the only known examples of single atoms showing long spin

lifetime. Concerning atoms at surfaces, so far only two rare earths have been reported to exhibit magnetic remanence: Ho on MgO/Ag(100) [1, 98], and Dy on MgO/Ag(100) [13, 173] as well as on graphene/Ir(111) [12]. Experimental results with rare earth atoms on metallic substrates made it clear that a decoupling layer is needed to prevent scattering events with the substrate phonons and electrons [132, 204, 213]. Understanding what makes these combinations of substrate and rare earth so special is key to identifying the ingredients required to make a single atom magnet, and to find systems with improved properties.

We report the magnetic properties of RE adatoms on NaCl thin films grown on Cu(111) and on Ag(111). The systems are investigated with synchrotron X-ray experiments at the EPFL-PSI X-Treme beamline[52], with the support of density functional theory simulation (DFT), scanning tunneling microscopy (STM), and multiplet simulations for X-ray spectra computation (see Methods 5.4). We show that on NaCl thin films Dy adatoms display long spin lifetime at 2.5 K, it is therefore a newly discovered single atom magnet, while Ho and Gd are paramagnetic. These results are interpreted on the basis of the magnetic energy level schemes resulting from the crystal field imposed by adsorption on the NaCl substrate, and on the properties of NaCl itself.

## 5.2 Results

We have carried out STM measurements in order to determine the adsorption site and therefore the symmetry of the crystal field experienced by the RE adatoms on NaCl. Figure 5.1(a) displays an STM image acquired on a bilayer of NaCl/Cu(111), in this case after Dy deposition. Dy and Ho atoms appear as protrusions with a typical apparent height of  $(120 \pm 10)$  pm, while a slightly larger apparent height of  $(135 \pm 10)$  pm is observed for Gd. The close-up in Fig. 5.1(b) shows the NaCl lattice atomically resolved with a few Dy adatoms (the depressions and smaller protrusion are attributed to adsorbates on the underlying Cu substrate). We define two primitive vectors describing the positions of the NaCl species resolved in the STM images as protrusions. Then, by construction, all the substrate atoms imaged as protrusion are located at  $(n, m)$  coordinates,  $(n, m) \in \mathbb{Z} \times \mathbb{Z}$ . Adatoms adsorbed on top of substrate atoms imaged as protrusion would have  $(n, m)$  coordinates as well, while  $(n + \frac{1}{2}, m + \frac{1}{2})$  coordinates would identify adsorption on top of the NaCl species which are imaged as depression. Finally, a bridge adsorption site, between two Na and two Cl atoms, would correspond to  $(n, m + \frac{1}{2})$  or  $(n + \frac{1}{2}, m)$  coordinates. All observed adsorption sites are summarized in Fig. 5.1(c), in which we have brought all the measured values back to  $n = 0, m = 0$ . Our analysis, carried out over 15 Dy, 15 Ho, and 8 Gd adatoms, reveals adsorption on top sites of the same nature for all three RE elements.

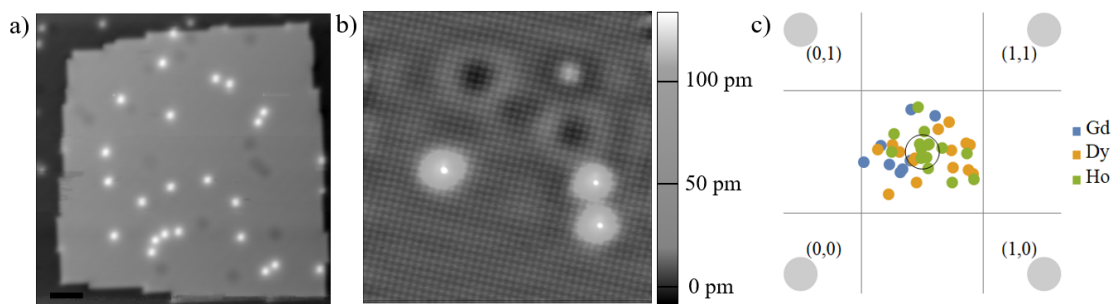


Figure 5.1: a) STM image showing Dy adatoms on a NaCl bilayer island and on the surrounding Cu(111) substrate,  $V_b = -2$  V,  $I_t = 70$  pA, length of the scalebar is 10 nm. b) Close up image on a bilayer NaCl displaying atomic resolution and individual Dy adatoms as protrusions. The non-monotonic color scale highlights the apex of each adatom,  $V_b = -2$  V,  $I_t = 50$  pA, length of the scalebar is 2 nm. c) Adsorption site of Dy, Ho and Gd adatoms with respect to the NaCl unit cell, the gray filled circles represent the substrate atoms resolved as protrusions and are identified by integer  $(n, m)$  values, the black open circle represents the substrate atoms images as depressions. The horizontal and vertical lines delimit the regions associated with each adsorption site.

Which substrate species is imaged as protrusion on NaCl ultrathin films can depend on the chemistry of the tip apex. While W tips have been reported to image Cl [221, 222], Cl-functionalized tips image Na [223] as protrusion. To determine if the RE adsorption site is top-Cl or top-Na, we have performed an experiment similar to the one carried out with Ca substitution in MgO layers [172, 224], this time using Mg as dopant for the growth of NaCl. Mg atoms are expected to replace Na atoms allowing identification of the species imaged as protrusions. This process indeed takes place, and the STM measurements demonstrate that in our experiments the Na atoms are resolved as protrusions (see Appendix 5.5).

To further support this finding, we have carried out DFT calculations to determine the RE adsorption site on NaCl (see Methods 5.4). Gd and Eu have been chosen to represent the investigated RE. More precisely,  $\text{Gd}(5p^6 6s^2 5d^1)$  and  $\text{Eu}(5p^6 6s^2 5d^0)$  were considered as valence configurations in the calculations. In these systems, the RE atoms feature a half-filled  $4f$  orbital, which is inert, and behave as trivalent  $\text{Gd}^{3+}$  and divalent  $\text{Eu}^{2+}$  species. This allows us to study the effect of the valency on the adsorption independently of multiplet effects. Note that inclusion of  $4f$  electrons in the valence band does not significantly modify the adsorption geometries and energies, meaning that we expect all atoms with a given valency to show similar binding properties. Therefore, we consider that  $\text{Gd}^{3+}$  and  $\text{Eu}^{2+}$  represent trivalent and divalent species, respectively.

As the experimental evidence points to adsorption at atop sites on a defect-free NaCl(100) surface, only top-Cl and top-Na sites were examined by DFT. The relative adsorption energies  $\Delta E_{ad}$  and relaxed structures are summarized in Table 5.1. For all the vdW functionals, physisorption on top-Cl is preferred to top-Na, the  $\Delta E_{ad}$  difference between those two sites

Table 5.1: Adsorption energy difference  $\Delta E_{ad}$  in eV between the top-Cl (most stable configuration) and top-Na sites as a function of the vdW functional for Gd and Eu. The distances in the relaxed structures for adsorption at the top-Cl site, shown here in Å, are represented in Fig. 5.2. The first and second nearest neighbor distances are  $d_1 = d(\text{RE} - \text{Cl})$  and  $d_2 = d(\text{RE} - \text{Na})$ , respectively. The  $b$  columns show the buckling of the topmost NaCl atomic plane with this sign convention:  $b < 0$  means that the atom under the RE lies below the surrounding atoms in the plane (see Fig. 5.2). For comparison, the buckling at clean NaCl(100) is in the 0.09-0.11 Å range for the studied functionals, with protruding Cl atoms.

vdW functional	Gd				Eu			
	$\Delta E_{ad}$	$d_1$	$d_2$	$b$	$\Delta E_{ad}$	$d_1$	$d_2$	$b$
D3	0.430	2.58	3.84	-0.10	0.081	2.75	4.11	0.16
D3(BJ)	0.370	2.59	3.87	-0.07	0.095	2.76	4.11	0.15
vdW-DF	0.331	2.69	4.03	0.08	0.168	2.91	4.33	0.32
optPBE	0.455	2.63	3.91	-0.04	0.269	2.82	4.16	0.16

being smaller for Eu than for Gd. For example, the D3(BJ) functional yields differences of 0.095 and 0.370 eV, respectively. This suggests a lower onset temperature of diffusion for Eu compared to Gd. The adsorption distances to the first and second nearest neighbors ( $d_1$  and  $d_2$ , respectively, defined in Fig. 5.2), support this interpretation, as their values are  $\sim 0.15$  Å smaller for Gd than for Eu at both adsorption sites. The other functionals follow a similar trend. Interestingly, the RE valency has a qualitative effect on the substrate relaxation upon adsorption: Gd and Eu induce a different buckling ( $b$ ) in the topmost NaCl atomic plane (see Fig. 5.2). In general, the Cl under the Gd atom lies  $\sim 0.10$  Å lower than the plane formed by the four surrounding Na atoms, whereas the Cl under the Eu atom lies  $\sim 0.15$  Å above it. For example, the exact heights for the D3(BJ) functional are  $b = -0.07$  and  $0.15$  Å, respectively. Considering that at the clean NaCl(100) the Cl atoms protrude by  $\sim 0.10$  Å, it is confirmed that the interaction with the divalent species is weaker. We find that bonding with the substrate occurs mainly via the delocalized electrons at the Fermi level, which are of  $s$  character for Eu (see Appendix 5.6). In the Gd case, the extra  $d$  electron also participates, contributing to create a stronger bond with the surface, which is consistent with the shorter Cl-Gd bond length. In summary, the investigated RE atoms chemisorb at top-Cl independent of their valency, with similar geometries, in agreement with the STM observations.

From the bonding point of view, top-Cl adsorption is coherent with top-O adsorption on MgO, which has been reported for all RE species investigated so far [172, 173, 224]. However, on NaCl we find this unique adsorption site, while on MgO there is coexistence of top-O and bridge adsorption sites, with relative abundances depending on the RE species and on the thickness of the MgO layer [172, 173, 224]. In particular, the highest proportion of RE adatoms on bridge sites is observed for films only 1 ML thick. The fact that on 2 ML NaCl we observe a single adsorption site indicates that this configuration is energetically favored already for the thinnest NaCl layers. Therefore, we expect the RE adsorption site to be exclusively top-Cl on thicker NaCl as well. This is also corroborated by the results of the DFT computations that

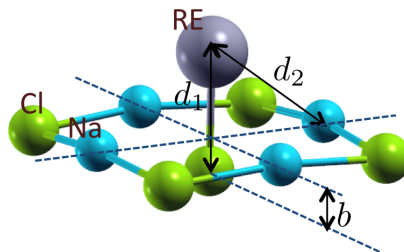


Figure 5.2: Definition of the distances  $d_1$ ,  $d_2$ ,  $b$  and  $b'$  for a RE atom physisorbed at top-Cl sites of NaCl(100). The bonds in this graph are artificially distorted and difference exaggerated to guide the eye. The actual DFT relaxed distances for RE = Gd and Cl are shown in Table 5.1. Color code: Cl in green, Na in blue, and RE in gray.

were carried out for a NaCl(100) slab of 6 ML.

The magnetic properties of the adsorbed RE atoms have been investigated by means of X-ray absorption experiments. For these measurements, thicker NaCl films were grown to ensure the absence of exposed bare metallic substrate regions. Figure 5.3 shows the results of measurements at the  $M_{4,5}$  edges of 0.019 ML Dy on 9 ML NaCl/Cu(111). The observed spectral shape indicates a  $4f^{10}$  configuration, with coexistence of  $4f^9$  species responsible for the third peak in the experimental XAS and XMCD spectra (full vertical line in Fig. 5.3(a, b)). However, this species is mainly associated with contaminated Dy atoms, as concluded from the increased intensity of the above-mentioned peak with sample aging [12, 211]. The  $4f^{10}$  configuration corresponds to the gas phase one, and to divalent Dy. The angular dependence of the XMCD intensity indicates a small out-of-plane anisotropy. Recording the XMCD signal at 1287 eV while sweeping the magnetic field gives an open hysteresis loop in normal incidence, see Fig. 5.3(c). The absence of remanence indicates quantum tunneling of the magnetization (QTM) at very low magnetic field. However, this QTM channel quickly gets inaccessible as the external magnetic field is turned on, resulting in slow dynamics at intermediate  $B$  fields up to about  $\pm 3$  T, as demonstrated by the butterfly-shaped loop. In particular, starting from zero field, we observe a non-constant magnetization decay with two steps, one below  $\pm 0.9$  T and the second at about  $\pm 3.2$  T, both suggesting level crossings at the respective fields. On the contrary, the grazing magnetization curve is closed within experimental resolution and does not show any specific feature, see Fig. 5.3(d).

To get insight into the magnetic ground state and in general into the energy level scheme responsible for the observed magnetic behavior, we performed multiplet calculations using the multiX code [78] in which the  $C_{4v}$  symmetric crystal field due to the top-Cl adsorption is described by an effective point charge approach. We focused at reproducing the out-of-plane anisotropy, the XMLD shape and behavior with respect to the magnetic field, the observed steps in the magnetization curves (indicative of change in the spin dynamics), and the existence of a tunneling channel close to zero field. In particular, the constraints imposed by the XMLD shape (see appendix C) allow us to exclude a  $m_J = \pm 8$  ground doublet and

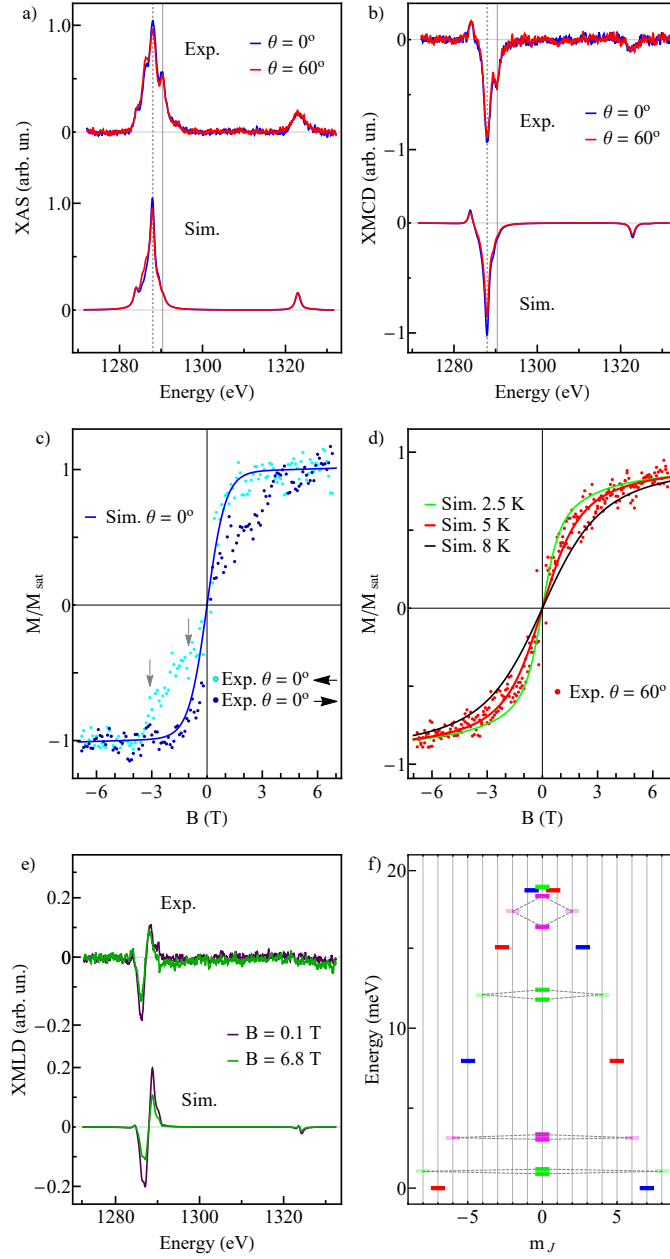


Figure 5.3: Measured data with simulated spectra of 0.019 ML Dy on 9 ML NaCl on Cu(111). The measurements are done at 2.5 K and the simulations are performed at different temperatures in (d) and at 5 K in all other panels. a) XAS, b) XMCD at the Dy  $M_{4,5}$  edges ( $B = 6.8$  T). c) Normal incidence magnetization curve acquired by recording the XMCD signal at 1287 eV (indicated by a dashed vertical line in b), field rate 2 T/min (flux  $1.5 \times 10^{-2}$  photons  $\text{nm}^{-2} \text{s}^{-1}$ ). The gray arrow indicate the position of the steps in the hysteresis. d) Grazing incidence magnetization curve with fits to determine the effective temperature. e) XMLD at the Dy  $M_{4,5}$  edges. f) Proposed energy level scheme in the  $J = 8$  multiplet explaining the observed data, the splittings of the split doublets are exaggerated for visibility (values are given in table 5.4).

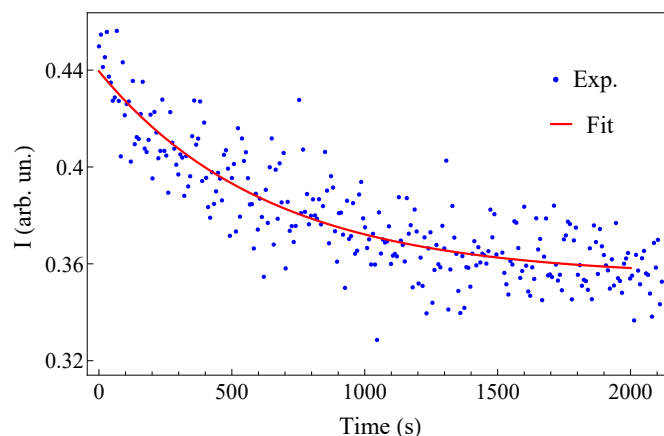


Figure 5.4: Decaying total yield signal difference between  $M_5$  edge 1287 eV and pre-edge 1280 eV at 0.3 T and 2.5 K, flux in the experiment is  $1 \times 10^{-2}$  photons  $s^{-1}$  nm $^{-2}$ .

point towards a  $m_J = \pm 7$  ground state. Note that, assuming the experimental temperature of  $T = 2.5$  K, multiplet calculations result in a too large magnetic susceptibility for  $B < 1$  T, both in grazing (see Fig. 5.3(d)) and normal (not shown) incidence. To find a better agreement, we used an effective temperature of the adatoms as fitting parameter. This approach is justified by the fact that in such experiments the photon energy is converted in secondary electrons and phonons. Spin-electron and spin-phonon scattering can put the adatom in an excited state characterized by a non-thermal population of the ground multiplet if relaxation processes are not efficient enough to allow the spin to thermalize to the bath (crystal) temperature. This process is known as phonon bottleneck [225–229]. Since our multiplet calculations are valid for the system at equilibrium, we focussed on the grazing incidence magnetization curve which shows negligible hysteresis. Our best fit is obtained for  $T = 5$  K and results in the energy level scheme shown in Fig. 5.3(e). The values are given in Appendix 5.2.

The obtained level scheme reflects a dominantly axial crystal field with some mixing induced by the  $C_{4v}$  crystal field symmetry, resulting in four families of the  $J_z$  eigenstates [71]. The  $m_J = \pm 7$  ground doublet is symmetry-protected against QTM. The butterfly shape of the magnetization curve is due to thermally-assisted QTM via the  $m_J = \pm 8$  and the  $m_J = \pm 6$  split doublets, found at relatively low energies. These states can be reached with  $\Delta m_J = \pm 1$  transitions resulting from spin scattering with phonons and secondary electrons. The crossing of  $m_J = \pm 7$  with  $m_J = \mp 8$  is responsible for the steps in the magnetization curve observed at  $B = \pm 0.9$  T, and the crossing of  $m_J = \pm 7$  with  $m_J = \mp 6$  for the one at  $\pm 3.2$  T. These crossings, involving states not mixed in  $C_{4v}$  symmetry, do not induce direct QTM, but they allow tunnel across the barrier mediated by  $\Delta m_J = \pm 1$  scattering processes.

In order to characterize the low field spin dynamics, we acquired the spin lifetime at different fields. To perform such measurements, the  $B$  field is first set to 6.8 T to saturate the sample magnetization and then reduced to the target value, where the difference in absorption at edge (1287 eV) and pre-edge (1280 eV), for a single polarization is acquired, as a function of

time. Although not being the XMCD signal, this quantity represents the dynamics of the Dy magnetization very well. The spin relaxation at 0.3 T is shown in Fig. 5.4, together with an exponential fit yielding a lifetime  $\tau = (550 \pm 100)$  s. We do not observe significant  $\tau$  variations in the 0.1 T to 0.5 T magnetic field range. The relaxation pathway and time are influenced by several factors, among which the adatom ground state and in general the energy level scheme, as well as the properties of the supporting substrate. Here, we find an energy scheme similar to the one obtained for Dy on graphene/Ir(111), which is also characterized by a  $4f^{10}$  electronic configuration, but by  $C_{6v}$ -symmetric crystal field [12, 211]. The ground  $m_J = \pm 7$  doublet is symmetry-protected from QTM in both cases, however, for Dy on NaCl the energy splitting between ground doublet and first excited state is too small to avoid thermal population and subsequent thermally-assisted QTM at very low  $B$ . The longer lifetime observed for Dy on graphene/Ir(111), of the order of 1000 s at 2.5 K, can be traced back to the higher stiffness of graphene and to the related lower density of phonon modes in the energy range of interest [178, 192], resulting in a reduced probability of reversal induced by spin-phonon scattering [230]. For Dy on top-O sites on MgO/Ag(100), both  $4f^9$  and  $4f^{10}$  occupations have been observed, depending on the MgO film thickness [173]. In the  $4f^{10}$  configuration, a  $m_J = \pm 8$  ground doublet well separated from the excited doublets has been deduced. These ground states are connected via QTM by the  $C_{4v}$  crystal field at  $B = 0$  T, resulting in very short lifetimes when approaching zero field. These differences in the energy schemes are well reflected in the shape of the magnetization curves for the two systems, in particular i) for Dy on MgO, direct QTM induces a very sharp butterfly-shaped hysteresis, and the absence of low-lying excited states is reflected by the lack of other steps in the magnetization curve [173] ; ii) for Dy on NaCl, the smoother butterfly shape arises from QTM via the first excited state, and the presence of level crossings is reflected by the steps in the magnetization curve at  $\pm 0.9$  T and  $\pm 3.2$  T.

To characterize further the crystal field generated by RE adsorption on NaCl, we have investigated the behavior of Ho adatoms. Figure 5.5 shows the results of X-ray absorption measurements at the  $M_{4,5}$  edges of 0.021 ML Ho on 8 ML NaCl/Cu(111). Comparison with XAS and XMCD spectra acquired on Ho adatoms on different surfaces allows us to identify the Ho electronic configuration as  $4f^{11}$  [204]. As for Dy, the presence of  $4f^{10}$  species, identified as contaminated Ho adatoms, is revealed by the relatively high intensity of the peak indicated with full vertical lines in Fig. 5.5(a,b). The XMCD spectra acquired at normal and grazing incidence reveal a very weak in-plane anisotropy. The magnetization curves recorded by acquiring the XMCD signal at 1342 eV are paramagnetic (Fig. 5.5(d)), showing that the magnetic relaxation time is shorter than the time-scale of the measurement. The XMLD spectra, being almost identical at 0.1 T and 6.8 T, point towards a strong crystal field allowing minimal modification of the level order when varying the magnetic field in the experimental range.

Further insight is gained by comparing the data with multiplet calculations. We focus on reproducing the spectral features of Ho shown in Fig. 5.5, with particular emphasis on the weak anisotropy, on the shape and intensity of the XMLD signal with its weak dependence *vs.* applied magnetic field, and on the shape of the magnetization curves. To describe the crystal field, we use effective point charges with  $C_{4v}$  symmetry, see Table 5.3 in Appendix. The



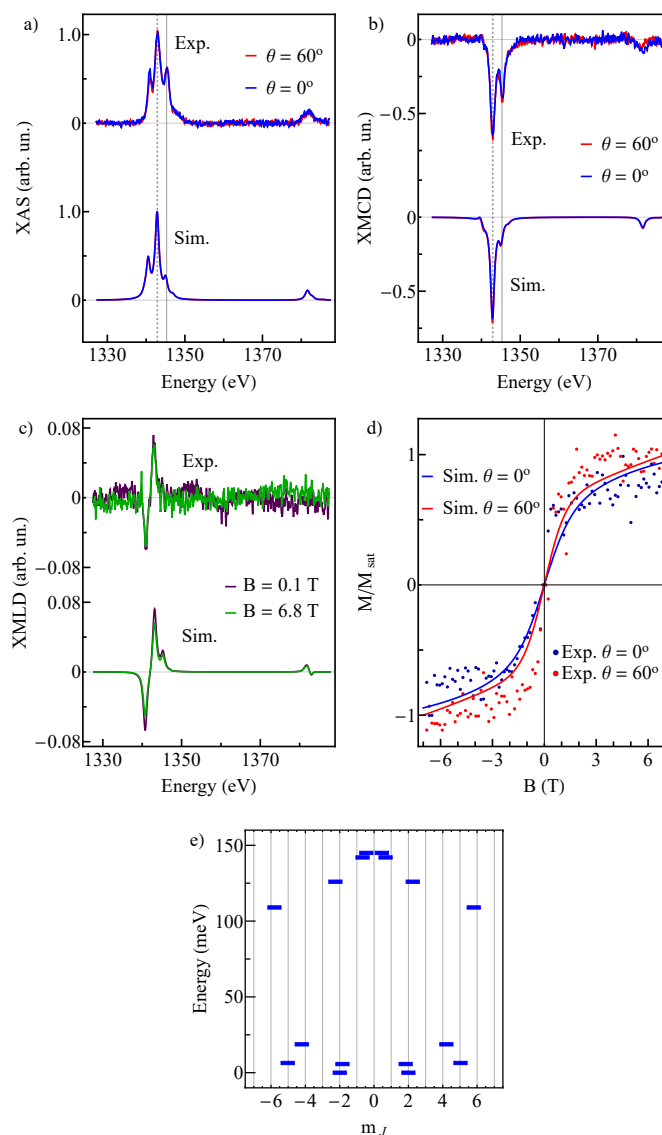


Figure 5.5: Measured XAS, XMCD, and XMLD together with multiplet simulations for 0.021 ML Ho on 8 ML NaCl on Cu(111) at 2.5 K. a) XAS, b) XMCD, c) XMLD at the Ho  $M_{4,5}$  edges ( $B = 6.8$  T). d) XMCD signal (peak at 1342 eV indicated by a dashed vertical line) recorded while sweeping the magnetic field at 2 T/min (flux  $1.9 \times 10^{-2}$  photons  $\text{nm}^{-2} \text{s}^{-1}$ ). The simulated magnetization curves are normalized with respect to the intensity of the peak at 1342 eV in the XMCD simulated at grazing and normal incidence. e) Proposed energy level scheme of the lowest Ho multiplet ( $J = \frac{15}{2}$ ) resulting from multiplet calculations.

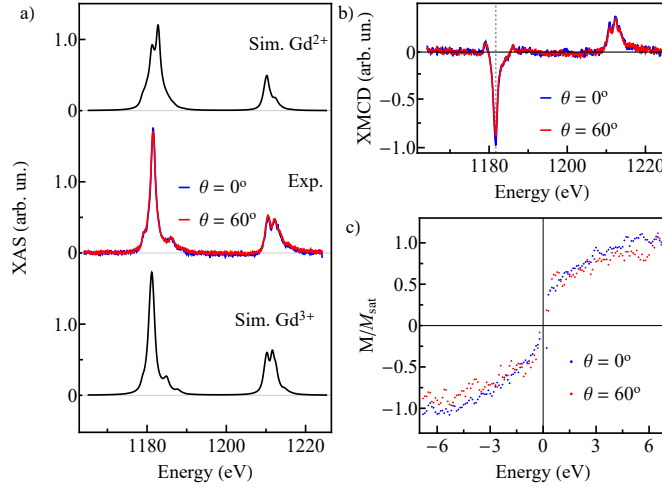


Figure 5.6: Measured data for 0.017 ML Gd deposited on 11 ML of NaCl on Ag(111) at the  $M_{4,5}$  edges of Gd. a) Experimental XAS with the simulation of the XAS of  $Gd^{3+}$  and  $Gd^{2+}$ . b) XMCD spectra, the dashed line indicates the peak at 1182 eV. c) Magnetization curve acquired by sweeping the field at 2 T/min (flux  $1.6 \times 10^{-2}$  photons  $nm^{-2} s^{-1}$ ).

resulting energy diagram is shown in Fig. 5.5(e). The Ho magnetization is poorly protected from reversal because of the strong mixing between eigenstates of the angular momentum operator in the entire magnetic field range used in our experiment.

Ho adsorbed on top-O site on MgO/Ag(100) in the  $4f^{10}$  electronic configuration has out-of-plane easy axis and remarkable magnetic stability [1, 98]. On the contrary, its  $4f^{11}$  counterpart, observed mainly on thicker MgO films, displays in-plane anisotropy [231]. The absence of well-defined anisotropy for Ho on NaCl is likely related to the combination of valency and stronger transverse crystal field terms.

As already discussed, on MgO/Ag(100) Dy and Ho are divalent or trivalent depending on the MgO film thickness, the general trend being to recover the free-atom valency on thicker MgO layers [173, 231]. In line with these results, we find that both Dy and Ho are divalent on the relatively thick NaCl films used in our X-ray experiments. This behavior was taken into account in our DFT calculations for the adsorption site, where we have chosen  $Eu^{2+}$  as prototype for divalent rare earths, while we used  $Gd^{3+}$  to represent trivalent adatoms [232, 233]. Nevertheless, we have carried out X-ray absorption measurements to confirm that this behavior is valid also for Gd adatoms on NaCl films. Figure 5.6 shows the XAS, XMCD and magnetization curves for 0.017 ML Gd adatoms adsorbed on 11 ML NaCl/Ag(111). The XAS indicates a  $4f^7$  trivalent configuration as corroborated by the comparison with simulations of free standing atoms in  $4f^7$  ( $Gd^{3+}$ ) and  $4f^8$  ( $Gd^{2+}$ ) electronic configuration. The XMCD spectra together with the magnetization curves reveal a tiny out-of-plane anisotropy. The absence of a well-defined magnetization easy axis is expected for Gd because of its isotropic nature as free atom with orbital angular momentum  $L = 0$ . However, a small anisotropy can be induced by appropriate crystal fields, as observed in molecular complexes [234–238].

## 5.3 Conclusions

In conclusion, NaCl proved to be a good supporting layer for protecting magnetization reversal of single atoms leading to a lifetime of at least 500 s for Dy at non-zero magnetic field. Although MgO was shown to have a more stabilizing effect, the uniqueness of electronic configuration and adsorption site for the three investigated rare earth elements makes NaCl a great system for ensemble characterization. For example, it represents an ideal benchmark for a systematic investigation of the effect of a  $C_{4v}$  crystal field across all rare earth atoms. In addition, different chloride salts such as KCl or CsCl could be used to take advantage of the different lattice parameters and electronegativity to tune the axial *vs.* transverse crystal field terms. On a different note, recent findings have shown that intra-atomic exchange coupling between the  $4f$  and the outer electronic shells can play a role in the spin dynamics of rare-earth single atoms [239]. Our DFT calculations in Appendix 5.6 indicate that for divalent species, represented by Eu, the outer shell is not polarized, while trivalent Gd displays clear polarization. Therefore it could be worth investigating other rare earth species expected to show magnetic anisotropy and with a tendency to be trivalent, such as Tb or Ce [232, 233], to explore the effect of intra-atomic exchange coupling on the spin dynamics.

## 5.4 Methods

### Sample preparation

The Cu(111) single crystal was prepared *in situ* by repeated sputtering (0.8 - 1.2 keV, 30 min) and annealing (720 - 750 K, 40 min) cycles. NaCl thin films were grown using an effusion cell heated at 770 K, on the substrate kept at room temperature. For the STM experiments, we used a nominal coverage of the order of 0.5 ML, resulting in regions of bare substrate coexisting with extended NaCl island 2 or 3 ML thick. For the synchrotron experiments, 8-11 ML of NaCl were grown, a coverage that ensures the absence of exposed bare metallic substrate. Rare earth atoms were deposited from high purity (99.9 %) thoroughly degassed rods using *e*-beam evaporators, on the substrate kept at approximately 10 K (STM) and 4 K (synchrotron experiments). The RE coverage is given in monolayers (ML), with one ML being one RE atom per NaCl surface unit cell. For the STM experiments we used coverages of the order of 0.1 % ML, while for synchrotron experiments the coverage was about 1 % ML.

### STM measurements

Scanning tunneling microscopy (STM) measurements were performed with a home-built STM, operating at 5 K [36]. The images were recorded in constant current mode using electrochemically etched W tips. The bias voltage  $V_t$  refers to the sample.

### DFT

In the density-functional theory (DFT) calculations, the NaCl(100) surface was modelled by a slab of 6 ML in a periodic supercell, leaving a vacuum space of 13 Å between slab images. The lateral periodicity was fixed to that of the NaCl crystal (5.64 Å), with rare earth (RE) adatoms

Gd and Eu forming a  $c(2 \times 2)$  superstructure. All the atomic positions were allowed to relax. As the experimental evidence points to adsorption at atop sites on a defect-free NaCl(100) surface, top-Cl and top-Na sites were examined by DFT. The geometry is shown in Fig. 5.8.

The spin-polarized DFT calculations were carried out in the projector augmented wave approach with plane wave basis sets, as implemented in VASP [240, 241]. Several van der Waals (vdW) functionals were used to address the weak interactions between the RE and the substrate. The functionals used in this work were: the DFT-D3 method of Grimme with zero damping (D3) [242] and the variant with Becke-Jonson damping [D3(BJ)] [243]; Dion's vdW-DF functional [244], self-consistently implemented [245, 246]; and the DF-based variations optPBE by Klimeš *et al.* [247, 248]. This allows us to cover different vdW formulations of the dispersion interactions, ranging from semiempirical (e.g., D3) to parameter-free non-local correlations (e.g., DF).

The convergence thresholds for the total energy and the forces on the atoms were  $10^{-7}$  eV and  $0.02 \text{ eV}\text{\AA}^{-1}$ , respectively. Partial state-occupancies in the self-consistency cycles were allowed with the Blöchl triangular method [249] and a 0.1 eV smearing width for the Fermi level ( $E_F$ ). The plane waves were constructed with a  $8 \times 8 \times 1$  sampling of the first Brillouin zone [250] and a 280 eV cut-off. Na( $2p^6 3s^1$ ), Cl( $2s^2 p^5$ ), Gd( $5p^6 6s^2 d^1$ ) and Eu( $5p^6 6s^2 d^0$ ) were considered as valence electrons in the calculations. We have checked that the inclusion of  $4f$  in the valence band does not significantly modify the adsorption geometries and energies. For this test, the strong correlation in the  $4f$  orbital was treated with the LDA+U method [251] in the Dudarev formulation [252] with values  $U = 7.5$  and  $3.5$  eV for Gd and Eu, respectively.

### **X-ray absorption measurements**

The X-ray absorption measurements were performed at the EPFL/PSI X-Treme beamline of the Swiss Light Source [52]. The experiments were carried out using both circularly ( $\sigma^+$ ,  $\sigma^-$ ) and linearly ( $\sigma^h$ ,  $\sigma^v$ ) polarized X-rays in the total electron yield (TEY) mode, at a sample temperature of 2.5 K. The XAS corresponds to  $(\sigma^+ + \sigma^-)$ , while XMCD and XMLD are defined as  $(\sigma^+ - \sigma^-)$  and  $(\sigma^h - \sigma^v)$ , respectively. The measurements were carried out at the  $M_{4,5}$  absorption edges of the RE species. Two incidence angles with respect to the surface normal have been used, namely normal incidence ( $\theta = 0^\circ$ ) and grazing incidence ( $\theta = 60^\circ$ ), in both cases the magnetic field was collinear with the incident X-rays. Background spectra in the energy range of interest were acquired for each NaCl/Cu(111) sample prior to the deposition of RE atoms, and were subtracted from the RE/NaCl/Cu(111) spectra to eliminate any contribution from the substrate. The magnetization curves were acquired by recording the maximum of the XMCD intensity as a function of the external magnetic field  $B$ .

### **Multiplet calculations**

Multiplet calculations of the RE XAS, XMCD and XMLD spectra were performed using the multiX software [78]. The crystal field generated by the interaction of the RE atom with the neighboring atoms of the NaCl/Cu(111) surface was modeled with point charges. The values used are reported in Appendix 5.8.

## 5.5 Identifying the species observed as a protrusion in atomically-resolved STM images on NaCl thin films

The literature reports that Cl atoms are imaged as protrusions in STM measurements on NaCl ultrathin films [221, 222], and that the Na atoms can appear as protrusion only with a functionalized tip [223]. To clarify what is the species we resolve in our measurements, we apply a method already used to discriminate between the Mg and O atoms in MgO using Ca doping [172, 224], this time by depositing Mg atoms on the NaCl layer with the aim of seeing some Mg atoms replacing Na ones. The result is shown in Fig. 5.7. In addition to the atomically resolved substrate species, other broad features, that we identify as Mg atoms, are visible. They appear as protrusions centered at the position of the resolved substrate atoms (as highlighted by the non-linear color-scale) and have an apparent height of 26 pm, compared to the corrugation of the substrate atoms of 7 pm. These results, implying that in our measurements the Na atoms are imaged as protrusions, are in line with our DFT calculations finding top-Cl as the most favorable absorption site for the RE atoms.

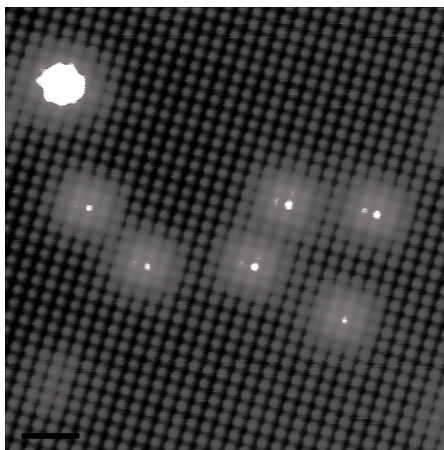


Figure 5.7: STM image of Mg deposited on NaCl bilayer on Cu(111),  $V_t = 1.2$  V,  $I_t = 85$  pA, length of the scalebar is 2 nm. The non-linear color scale highlights the Mg atom positions.

## 5.6 Additional DFT results

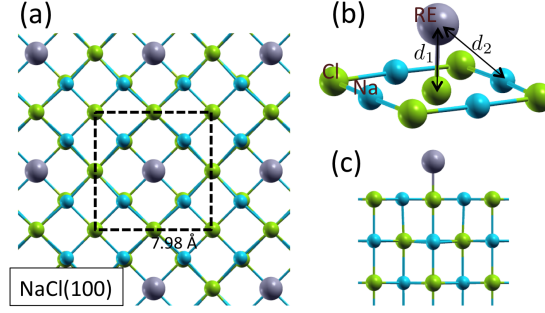


Figure 5.8: Top (a), detail (b) and side (c) views of the adsorption of RE atoms at the top-Cl sites of the 6 ML NaCl(100) film. The atomic positions shown here correspond to the D3(BJ) functional calculation for Gd. The  $c(2 \times 2)$  supercell for the DFT calculations is indicated with a dashed line. Colour code: Cl in green, Na in blue and RE in gray.

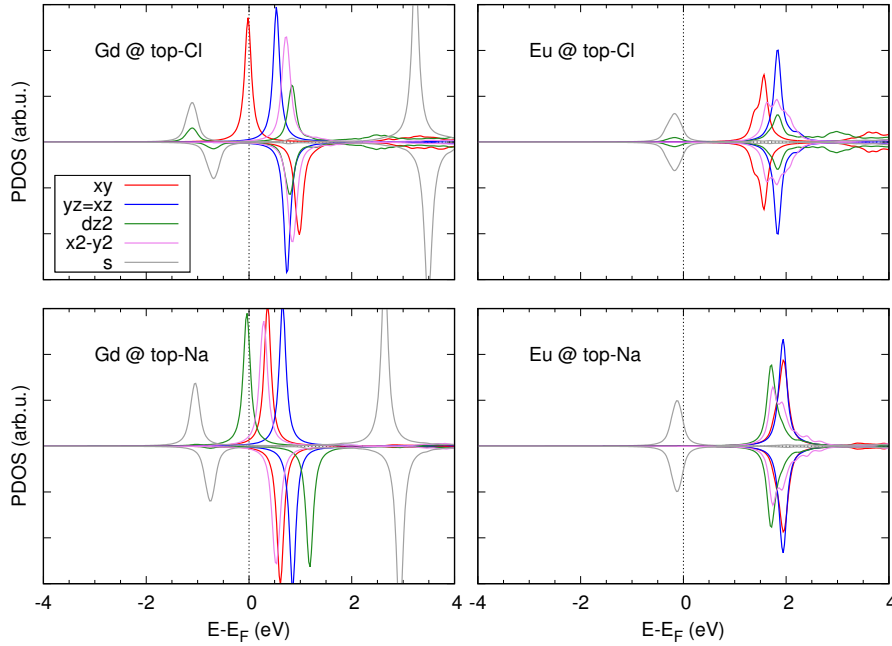


Figure 5.9: Projected densities of states PDOS (in arbitrary units) obtained with the D3(BJ) functional at the top-Cl and top-Na sites (other functionals, not shown, give similar curves). Physisorption in the stable top-Cl configuration occurs by hybridization of the RE(s) with the substrate, resulting in peaks at 1 eV for Gd(s) and 0.2 eV for Eu(s) below the Fermi level  $E_F$ . The Gd( $d_{xy}$ ) orbital pinned at the Fermi level is spin-polarized at the top-Cl site. Other Gd( $d$ ) states lie above  $E_F + 0.5$  eV. There is a 0.5 eV exchange splitting of the Gd(s) electrons, which lie at  $E_F - 1$  eV partially hybridized with Gd( $d_{z^2}$ ). At the top-Na site, it is the Gd( $d_{z^2}$ ) orbital pinned at the Fermi level that is spin-polarized, with empty Gd( $d$ ) states lying closer to  $E_F$  than in the top-Cl configuration.

## 5.7 Calibration of the NaCl film thickness

We calibrated the NaCl coverage combining room temperature STM measurements and XAS measurements at the Na K-edge. We prepared a sample displaying 25% of its surface covered mainly by NaCl islands. The NaCl growth starts with an initial double layer with islands of additional layers on top of it [179], a behaviour confirmed in our STM measurements. Subsequent XAS measurements allow us to make a correspondence between the coverage determined by STM and the edge jump at the Na K-edge. For thicker NaCl films, we estimated the number of NaCl layers from the intensity of the Na K-edge by comparing its height to the calibrated value. Figure 5.10 show a typical XAS spectrum acquired on a NaCl/Cu(111) film. Using the procedure outlined above, we deduce that this film corresponds to a nominal coverage of 9 ML of NaCl.

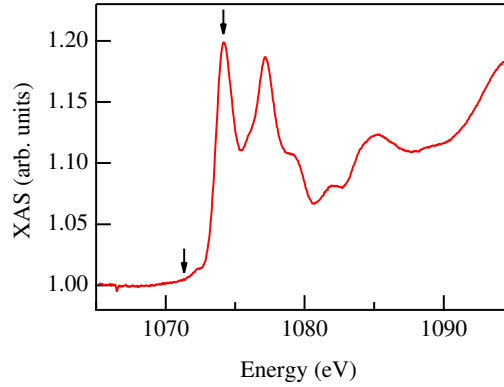


Figure 5.10: Normalized XAS spectrum acquired on 9 ML of NaCl on Cu(111) at the Na K-edge (room temperature,  $B = 0.1$  T). Arrows indicate the energy position for the determination of the edge jump height.

## 5.8 Crystal fields of holmium and dysprosium on NaCl/Cu(111)

The point charges listed in Tables 5.2 and 5.3, generating the CF, are used as input in the MultiX software and are the only free parameters of the simulations once the valency is set.

Table 5.2: Point charges used for the simulations of Dy on NaCl. The Dy atom is placed at the origin of the coordinate system. The xy plane is parallel to the surface.

Charge No	x(Å)	y(Å)	z(Å)	q(e)
q <sub>1</sub>	-2.7	0	-2.8	-1.75
q <sub>2</sub>	2.7	0	-2.8	-1.75
q <sub>3</sub>	0	2.7	-2.8	-1.75
q <sub>4</sub>	0	-2.7	-2.8	-1.75
q <sub>5</sub>	0	0	-2.8	0.31

Table 5.3: Point charges used for the simulations of Ho on NaCl. The Ho atom is placed at the origin of the coordinate system. The xy plane is parallel to the surface.

Charge No	x(Å)	y(Å)	z(Å)	q(e)
q <sub>1</sub>	-1.6	0	-1.2	2.9
q <sub>2</sub>	1.6	0	-1.2	2.9
q <sub>3</sub>	0	1.6	-1.2	2.9
q <sub>4</sub>	0	-1.6	-1.2	2.9
q <sub>5</sub>	0	0	-2.2	0.1

In figure 5.3 f), the zero field splitting of the Dy adatom split doublets were exaggerated for readability. The exact values are given in Tab. 5.4:

Table 5.4: Zero field splitting of the Dy doublets.

$m_J$	Energy (meV)
$\pm 8$	0.002
$\pm 6$	0.01
$\pm 4$	0.3



## 6 Conclusion

In this thesis we investigated the self-assembly of three molecular ligands (QDC, BDA, ZnTPyP) with rare earth atoms on three decoupling layers (MgO, NaCl, graphene). MgO and NaCl did not allow the coordination of rare earths with the molecules. Nitrogen-terminated ligands on MgO were not observed as the molecules either diffuse from the islands to the Ag(100) substrate or do not adsorb at all. On the contrary, BDA's interaction with MgO is too strong to allow binding to rare earth atoms. The propensity of NaCl to dissolve and form a coordination structure with the molecular ligands prevents formation of metal-organic networks on this substrate. Coordination complexes were produced with the nitrogen terminated ligands (QDC, ZnTPyP) on gr/Ir(111). We did not succeed in obtaining large gr/Ir(111) areas of graphene covered by the rare earth-ZnTPyP structure. However a rare earth-QDC metal-organic network was synthesized, covering a large portion of the gr/Ir(111) surface.

Magnetic properties of the Dy- and Er-QDC coordination complexes on gr/Ir(111) were measured with XAS, XMCD and XMLD spectroscopy. An inversion of the easy-axis of magnetization with respect to single atoms on gr/Ir(111) was observed for both species, from in-plane to out-of-plane for Er, and from out-of-plane to in-plane for Dy. Multiplet simulations and qualitative estimation of the electrostatic interaction were carried out to support the interpretation of experimental data and to gain further understanding of these systems.

In parallel, X-ray data of single Dy and Ho atoms on NaCl/Cu(111) and of single Gd atoms on NaCl/Ag(111) were analyzed and their interpretation was supported by multiplet calculations. STM measurements determined the adsorption site for each of the three species to be top-Cl. Dy exhibits long relaxation time at non-zero magnetic field, thanks to the decoupling effect of the NaCl layer.

In the future the preliminary results on gr/Ir(111) of chapter 4 should be completed with measurements on other lanthanides. Improved models could complete the basic investigation of the  $4f$  asphericity, possibly taking into account the intershell coupling of Dy and Er. Ligands with different geometry, see for example reference [141], could be interesting candidates for the formation of rare-earth based metal-organic structures on graphene as steric repulsion

## Chapter 6. Conclusion

---

could produce more regular networks. Deprotonation of the carboxylate group on graphene is an interesting challenge. While we briefly tried to deprotonate BDA on gr/Ru(0001), depositing larger ligands that could bear higher temperature before desorption is still an option. However, a surface with higher catalytic effect will also interact more strongly with the magnetic element: the sweet spot will be a substrate that has enough interaction with the carboxylate moieties to catalyze their deprotonation, but not so much as to perturb the magnetic moment of the rare earth atoms.

# A Inelastic electron tunneling spectroscopy on Dy-QDC

A more complete picture of the magnetic properties of lanthanides must include the intra-atomic exchange interaction between the  $4f$  and the  $5d6s$  shells [239]. Inelastic electron tunneling spectroscopy is a tool that can be used to investigate the properties of atomic-scale magnetic systems [253–255]. Many rare earth atoms on graphene/Ir(111) exhibit inelastic excitations at energies of the order of  $\sim 100$  meV due to intra-atomic exchange coupling [239]. In particular, Dy ( $4f^{10}$ ) adatoms on gr/Ir(111) exhibit a conductance step at  $\pm 90$  meV. We searched for the presence similar signatures in the rare earth atoms coordinated with molecular ligands described in chapter 3. In the Dy-QDC metal-organic structure, an inelastic step at approximately  $\pm 50$  meV was observed (figure A.1), but only on the fourfold coordinated Dy atoms. The reference spectra acquired on the surface were flat, excluding the contribution of junction artifacts. If the presence of the inelastic features is confirmed with further measurements the diminution of the exchange energy would indicate a reduction of the spin of the outer shell due to bonding with the surrounding ligands.

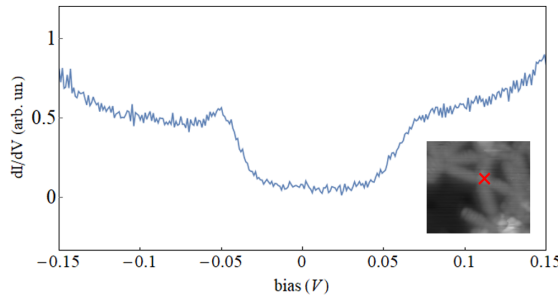


Figure A.1: STS spectra acquired on a fourfold coordinated Dy atom in a Dy-QDC/graphene/Ir(111) coordination complex ( $I_{set} = 50$  pA,  $V_{mod} = 9$  mV at 532 Hz). The displayed spectrum is an average of two spectra. Inset: STM image of the site of acquisition of the spectra. Tunneling conditions:  $V_t = -3$  V,  $I_t = 50$  pA, 5 K.



## B Tables of spectra for the simulations of Dy- and Er-QDC/gr/Ir(111)

In chapter 4, the constraints on the ground state of Dy ( $4f^9$ ) and Er( $4f^{11}$ ) were obtained by comparing with the XAS of some of the pure  $m_J$  states. By putting two artificial axial charges below Er and Dy atoms in the simulations, and by varying their distance to the atoms and their intensity, we could induce all  $m_J$  as ground states, except  $m_J = 13/2$  for Dy and  $m_J = 7/2$  and  $m_J = 9/2$  for Er. By simulating at 0 K we insure only the ground state is populated and therefore only the spectra generated by the ground state are seen in the simulations. We specifically looked at the peak at 1287 eV for Dy (figure 4.2 (a)) and the first peak at 1398 eV for Er (figure 4.4 (a)). The peaks are indicated by black arrows in the first simulated spectra of figures B.1 and B.2, where the simulated XAS of Dy and Er are shown, respectively.

In the discussion of chapter 4 we tried to find a correlation between the angle  $\alpha$  with the  $z$ -axis of the center of charge in an octant of a  $4f$  distribution and the shape of linear dichroism spectra of Dy and Er. For Dy, the inversion of XMLD is seen between the  $m_J = 9/2$  and  $m_J = 11/2$  in figure B.3, as  $\alpha$  crosses the  $\pi/4$  angle (see figure 4.8). However, we do not observe such a correlation for Er, as seen in figure B.4.

## Appendix B. Tables of spectra for the simulations of Dy- and Er-QDC/gr/Ir(111)

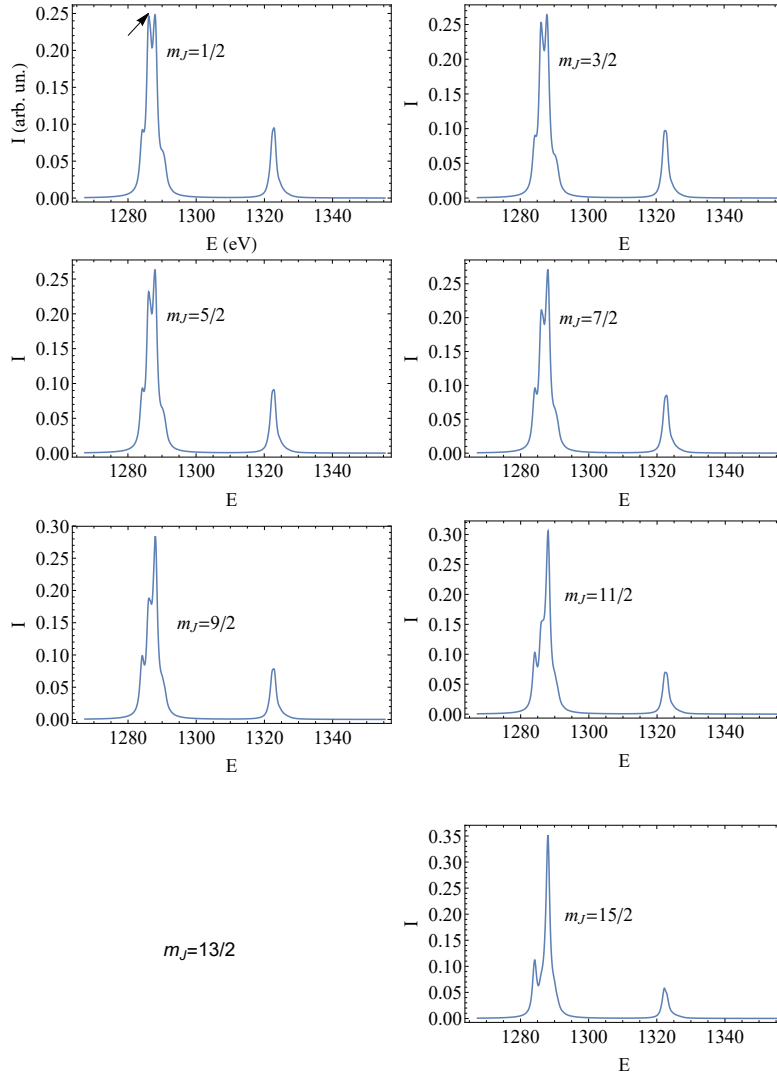


Figure B.1: Multiplier simulation of the XAS (sum of left and right handed polarizations) at 0 K with incidence  $\theta = 0^\circ$  of some  $m_J$  pure states of  $\text{Dy}^{3+}$  in a 5.5 T external magnetic field normal to the surface. We haven't found point charges leading to an  $m_J = 13/2$  state yet.

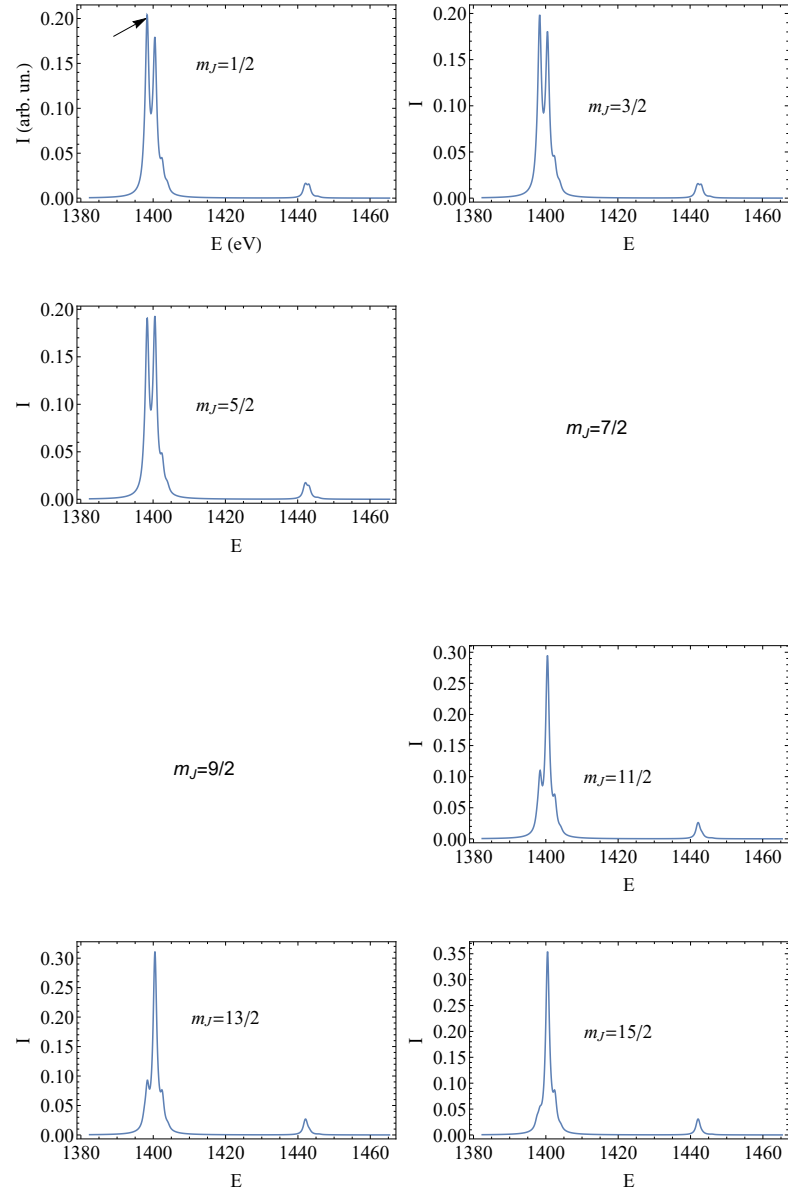


Figure B.2: Multiplet simulation of the XAS of some  $m_J$  pure states of  $\text{Er}^{3+}$ . We haven't found point charges leading to an  $m_J = 7/2$  and  $m_J = 9/2$  state yet.

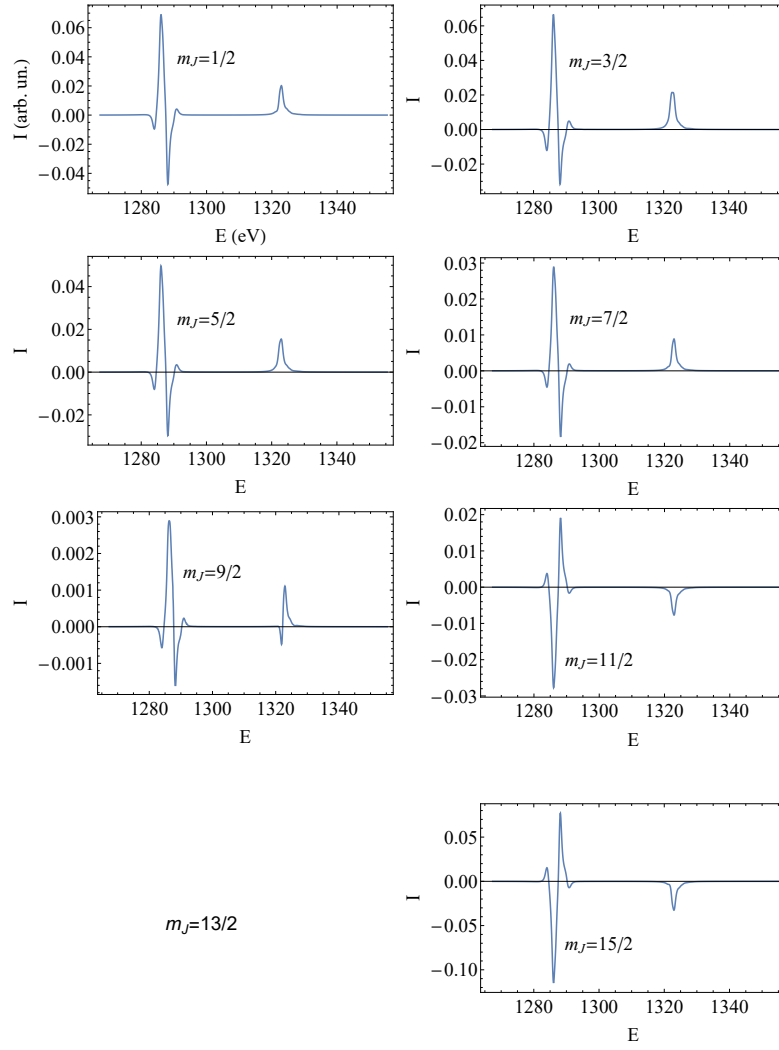


Figure B.3: Simulated XMLD (difference between the vertical and horizontal linearly polarized absorption spectra) spectra at  $\theta = 60^\circ$  for some  $m_J$  states of Dy.



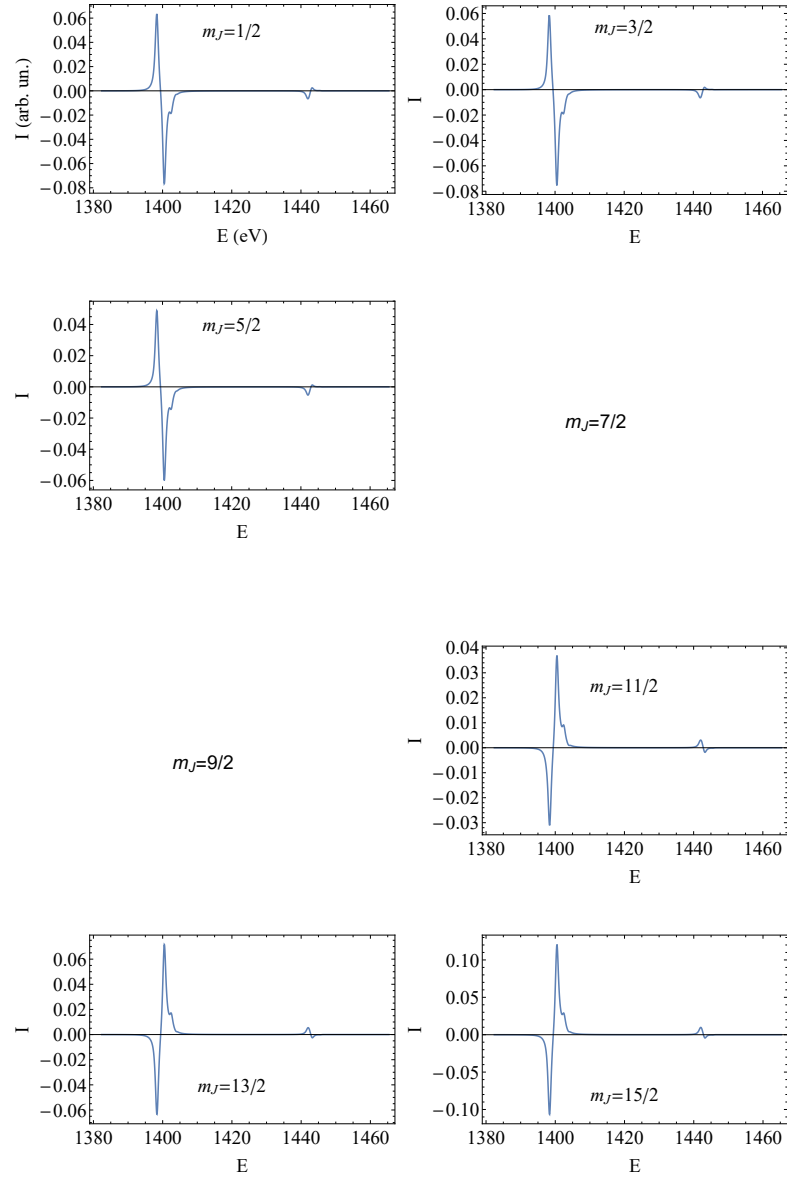


Figure B.4: Simulated XMLD spectra at  $\theta = 60^\circ$  for some  $m_J$  states of Er.



## C Determination of the ground state of Dy/NaCl/Cu(111)

Looking at the linearly polarized x-ray absorption spectra instead of considering the XMLD can help determine the ground state. This approach was used to find constraints in chapter 5. The two experimental spectra at 0.1 T for  $\sigma_v$  and  $\sigma_h$  are shown in figure C.1. Comparing them with the simulated spectra obtained from all the  $m_J$  states given in figure C.2, we deduce a dominance of the  $m_J = \pm 7$  state for the ground state. The highest peak in the  $\sigma_v$  absorption spectrum at 1286 eV is higher than the second one at 1288 eV (both indicated with a black arrow).  $m_J = 7$  spectrum is the only one that a discernible peak at 1288 eV while having a higher peak at 1286 eV. All pure  $m_J$  states are obtained using an artificial crystal field generated by two axial charges. The charges are aligned below the Dy atom. By varying their distance to the Dy atom and their intensity we were able to bring each  $m_J$  as ground states.

## Appendix C. Determination of the ground state of Dy/NaCl/Cu(111)

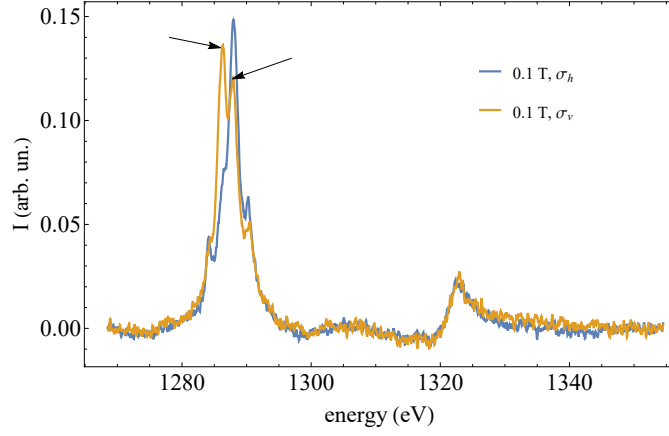


Figure C.1: Linear absorption spectra of 0.019 ML Dy on 9 ML NaCl on Cu(111) at  $\theta = 60^\circ$ . Temperature is 2.5 K.

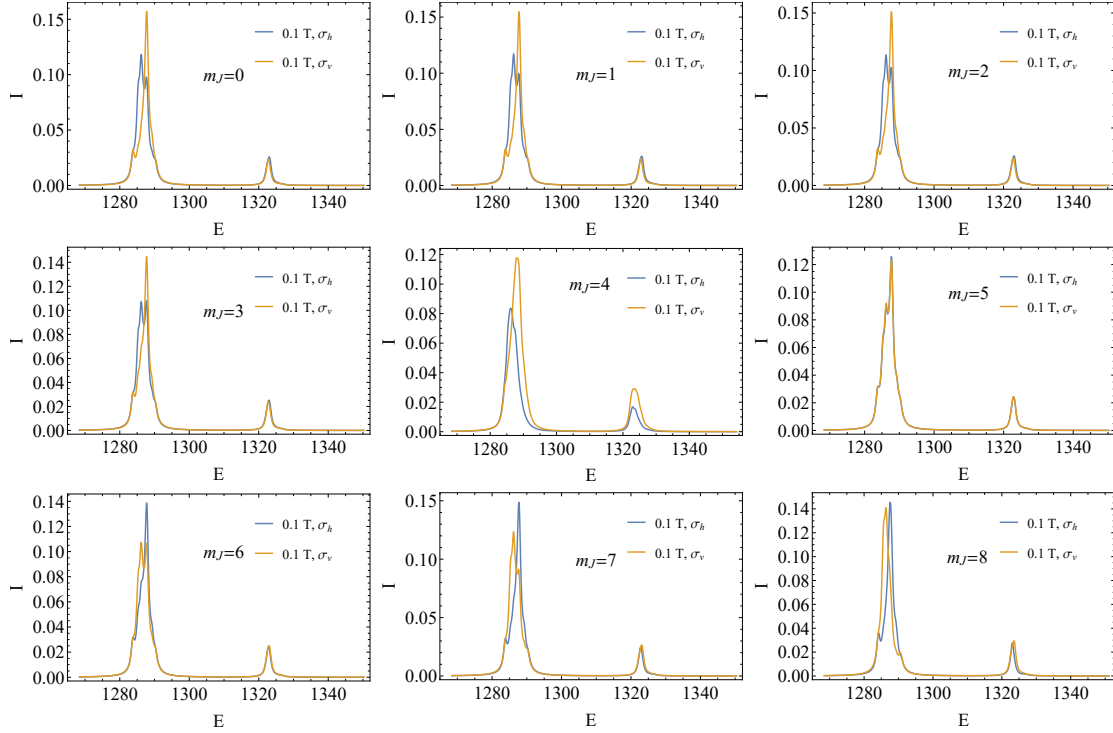


Figure C.2: Simulated linearly polarized x-ray absorption spectra at  $\theta = 60^\circ$  for the two polarizations for the  $m_J$  states of Dy ( $4f^{10}$ ) in the  $J = 8$ .

## D Gd/NaCl/Ag(111)

We carried out attempts to reproduce the x-ray data of Gd/NaCl/Ag(111) with multiplet simulations. It was difficult to affect the ordering of the  $m_J$  states of Gd with point charges. Instead we tried to extract information by applying the sum rules and looking at the magnetization curves. Gd has a half-filled  $4f^7$  shell with  $J = S = 7/2$  and  $L = 0$ . The sum rules applied to the XMCD spectra (figure 5.6) give  $\langle S_z \rangle = 5/2$  at 6.8 T. We can simulate the magnetization curve with a spin Hamiltonian (equation 2.15). Although Gd in the  $4f^7$  configuration cannot usually be treated with the spin Hamiltonian model, we only aimed at adding constraint on the energy level scheme for the multiplet simulation. We restricted ourselves to axial operators at first. Our simulation best fits the slope of the magnetization curve around 0 T when the ground state is  $m_J = 3/2$ . Taking in account the result of the sum rules, and the isotropy of Gd/NaCl/Ag(111), we found the Stevens coefficient of table D.1 that produce the magnetization curves shown in figure D.1. Accepting this fit, we then tried to reproduce the same energy level scheme (table D.2) with multiplet simulation. Even starting from a known energy scheme, we could not reproduce the desired energy levels with a point charge model. Most reasonable charge configuration only give sub-meV level splitting. As the charges get larger or closer to the Gd atom, other multiplets start to mix with the multiplet  $J = 7/2$ . We could not reproduce that energy level scheme in with point charges, and therefore could not simulate the spectra.

Table D.1: Stevens coefficient for the simulation of Gd/NaCl/Ag(111).

$B_0^2$	$B_0^4$	$B_0^6$
0.16349 eV	0.01738 eV	0.000502 eV

Table D.2: Energy level of the positive  $m_J$  states of Gd at  $B = 0$  T.

$m_J = 1/2$	$m_J = 3/2$	$m_J = 5/2$	$m_J = 7/2$
20 meV	0 meV	0.4 meV	20 meV

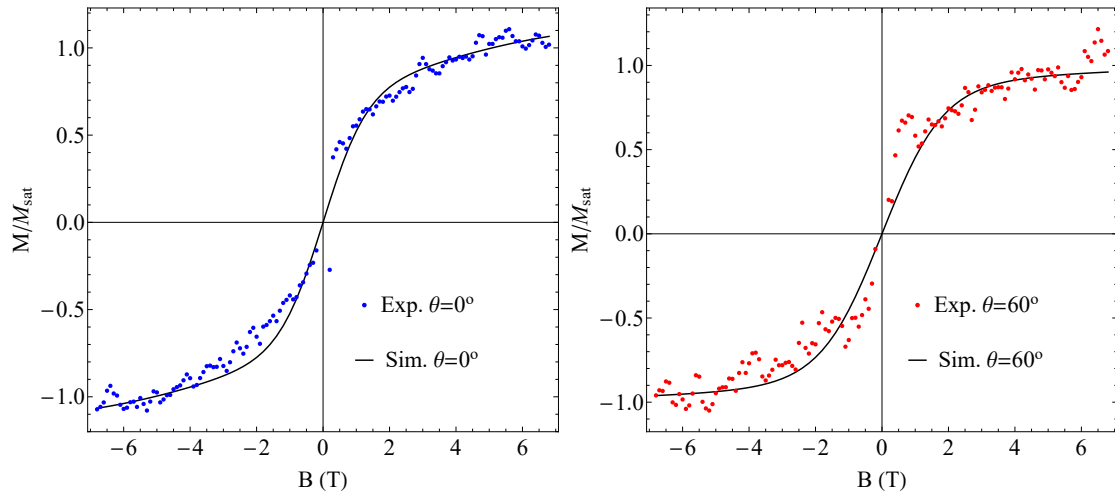


Figure D.1: Simulated magnetization curves superimposed on the experimental data of figure 5.6

## Bibliography

- [1] F. Donati, S. Rusponi, S. Stepanow, C. Wäckerlin, A. Singha, L. Persichetti, R. Baltic, K. Diller, F. Patthey, E. Fernandes, J. Dreiser, Ž. Šljivančanin, K. Kummer, C. Nistor, P. Gambardella, and H. Brune, *Magnetic remanence in single atoms*, Science **352**, 318–321 (2016).
- [2] N. Ishikawa, M. Sugita, T. Ishikawa, S.-y. Koshihara, and Y. Kaizu, *Lanthanide double-decker complexes functioning as magnets at the single-molecular level*, Journal of the American Chemical Society **125**, 8694–8695 (2003).
- [3] M. Urdampilleta, S. Klyatskaya, J.-P. Cleuziou, M. Ruben, and W. Wernsdorfer, *Supramolecular spin valves*, Nature Materials **10**, 502–506 (2011).
- [4] F. D. Natterer, K. Yang, W. Paul, P. Willke, T. Choi, T. Greber, A. J. Heinrich, and C. P. Lutz, *Reading and writing single-atom magnets*, Nature **543**, 226–228 (2017).
- [5] S. Thiele, F. Balestro, R. Ballou, S. Klyatskaya, M. Ruben, and W. Wernsdorfer, *Electrically driven nuclear spin resonance in single-molecule magnets*, Science **344**, 1135–1138 (2014).
- [6] N. Schlosser, G. Reymond, I. Protsenko, and P. Grangier, *Sub-poissonian loading of single atoms in a microscopic dipole trap*, Nature **411**, 1024–1027 (2001).
- [7] G. Binnig, H. Rohrer, C. Gerber, and E. Weibel, *Surface studies by scanning tunneling microscopy*, Physical Review Letters **49**, 57–61 (1982).
- [8] G. Binnig, H. Rohrer, C. Gerber, and E. Weibel,  *$7 \times 7$  reconstruction on Si(111) resolved in real space*, Physical Review Letters **50**, 120–123 (1983).
- [9] G. Binnig and H. Rohrer, *Scanning tunneling microscopy*, Physica B+C **127**, 37–45 (1984).
- [10] J. Luzon and R. Sessoli, *Lanthanides in molecular magnetism: so fascinating, so challenging*, Dalton Transactions **41**, 13556–13567 (2012).
- [11] F.-S. Guo, B. M. Day, Y.-C. Chen, M.-L. Tong, A. Mansikkamäki, and R. A. Layfield, *Magnetic hysteresis up to 80 kelvin in a dysprosium metallocene single-molecule magnet*, Science **362**, 1400–1403 (2018).

## Bibliography

---

- [12] R. Baltic, M. Pivetta, F. Donati, C. Wackerlin, A. Singha, J. Dreiser, S. Rusponi, and H. Brune, *Superlattice of single atom magnets on graphene*, Nano Letters **16**, 7610–7615 (2016).
- [13] A. Singha, P. Willke, T. Bilgeri, X. Zhang, H. Brune, F. Donati, A. J. Heinrich, and T. Choi, *Engineering atomic-scale magnetic fields by dysprosium single atom magnets*, Nature Communications **12**, 4179 (2021).
- [14] C. Wackerlin, F. Donati, A. Singha, R. Baltic, S. Rusponi, K. Diller, F. Patthey, M. Pivetta, Y. Lan, S. Klyatskaya, M. Ruben, H. Brune, and J. Dreiser, *Giant hysteresis of single-molecule magnets adsorbed on a nonmagnetic insulator*, Advanced Materials **28**, 5195–5199 (2016).
- [15] <https://sciencenotes.org/printable-periodic-table/>, Feb. 2022.
- [16] J. V. Barth, *Fresh perspectives for surface coordination chemistry*, Surface Science **603**, 1533–1541 (2009).
- [17] F. D. Natterer, F. Donati, F. Patthey, and H. Brune, *Thermal and magnetic-field stability of holmium single-atom magnets*, Physical Review Letters **121**, 027201 (2018).
- [18] L. Dong, Z. Gao, and N. Lin, *Self-assembly of metal–organic coordination structures on surfaces*, Progress in Surface Science **91**, 101–135 (2016).
- [19] E. Merzbacher, *The early history of quantum tunneling*, Physics Today **55**, 44–49 (2002).
- [20] E. L. Wolf, “Principles of electron tunneling spectroscopy: second edition”, in *International series of monographs on physics*, edited by J. Birman, S. F. Edwards, R. Friend, M. Rees, D. Sherrington, and G. Veneziano (Oxford science publications, Great Clarendon street, Oxford, 2011), pp. 2–5.
- [21] I. Giaever, *Energy gap in superconductors measured by electron tunneling*, Physical Review Letters **5**, 147–148 (1960).
- [22] I. Giaever, *Electron tunneling between two superconductors*, Physical Review Letters **5**, 464–466 (1960).
- [23] D. M. Eigler and E. K. Schweizer, *Positioning single atoms with a scanning tunnelling microscope*, Nature **344**, 524–526 (1990).
- [24] J. S. Foster, J. E. Frommer, and P. C. Arnett, *Molecular manipulation using a tunnelling microscope*, Nature **331**, 324–326 (1988).
- [25] G. P. Lopinski, D. J. Moffatt, D. D. M. Wayner, and R. A. Wolkow, *Determination of the absolute chirality of individual adsorbed molecules using the scanning tunnelling microscope*, Nature **392**, 909–911 (1998).
- [26] J. Bardeen, *Tunnelling from a many-particle point of view*, Physical Review Letters **6**, 57–59 (1961).
- [27] J. Tersoff and D. R. Hamann, *Theory and application for the scanning tunneling microscope*, Physical Review Letters **50**, 1998–2001 (1983).



- 
- [28] N. Garcia, C. Ocal, and F. Flores, *Model theory for scanning tunneling microscopy: application to Au(110) (1×2)*, Physical Review Letters **50**, 2002–2005 (1983).
- [29] J. Tersoff and D. R. Hamann, *Theory of the scanning tunneling microscope*, Physical Review B **31**, 805–813 (1985).
- [30] G. Binnig, N. Garcia, H. Rohrer, J. M. Soler, and F. Flores, *Electron-metal-surface interaction potential with vacuum tunneling: observation of the image force*, Physical Review B **30**, 4816–4818 (1984).
- [31] P. Echenique and M. Uranga, *Image potential states at surfaces*, Surface Science **247**, 125–132 (1991).
- [32] J. M. Blanco, F. Flores, and R. Pérez, *Stm-theory: image potential, chemistry and surface relaxation*, Progress in Surface Science **81**, 403–443 (2006).
- [33] N. D. Lang, *Spectroscopy of single atoms in the scanning tunneling microscope*, Physical Review B **34**, 5947–5950 (1986).
- [34] L. Bürgi, “Scanning tunneling microscopy as local probe of electron density, dynamics, and transport at metal surfaces”, PhD thesis (EPFL, 1999).
- [35] H. J. Reittu, *Fermi’s golden rule and bardeen’s tunneling theory*, American Journal of Physics **63**, 940–944 (1995).
- [36] R. Gaisch, J. Gimzewski, B. Reihl, R. Schlittler, M. Tschudy, and W. Schneider, *Low-temperature ultra-high-vacuum scanning tunneling microscope*, Ultramicroscopy **42-44**, 1621–1626 (1992).
- [37] L. Baumgarten, “X-ray absorption spectroscopy”, in *Scattering methods for condensed matter research: towards novel applications at future sources*, edited by M. Angst (Forschungszentrum Jülich GmbH, 2012), pp. 1056–1090.
- [38] B. T. Thole, G. van der Laan, and G. A. Sawatzky, *Strong magnetic dichroism predicted in the  $M_{4,5}$  x-ray absorption spectra of magnetic rare-earth materials*, Physical Review Letters **55**, 2086–2088 (1985).
- [39] G. van der Laan, B. T. Thole, G. A. Sawatzky, J. B. Goedkoop, J. C. Fuggle, J.-M. Esteve, R. Karnatak, J. P. Remeika, and H. A. Dabkowska, *Experimental proof of magnetic x-ray dichroism*, Physical Review B **34**, 6529–6531 (1986).
- [40] G. Schütz, W. Wagner, W. Wilhelm, P. Kienle, R. Zeller, R. Frahm, and G. Materlik, *Absorption of circularly polarized x rays in iron*, Physical Review Letters **58**, 737–740 (1987).
- [41] C. T. Chen, F. Sette, Y. Ma, and S. Modesti, *Soft-x-ray magnetic circular dichroism at the  $L_{2,3}$  edges of nickel*, Physical Review B **42**, 7262–7265 (1990).
- [42] B. T. Thole, R. D. Cowan, G. A. Sawatzky, J. Fink, and J. C. Fuggle, *New probe for the ground-state electronic structure of narrow-band and impurity systems*, Physical Review B **31**, 6856–6858 (1985).

## Bibliography

---

- [43] S. Imada and T. Jo, *Magnetic circular dichroism in core x-ray absorption spectra of rare-earths*, Journal of the Physical Society of Japan **59**, 3358–3373 (1990).
- [44] B. T. Thole, P. Carra, F. Sette, and G. van der Laan, *X-ray circular dichroism as a probe of orbital magnetization*, Physical Review Letters **68**, 1943–1946 (1992).
- [45] P. Carra, B. T. Thole, M. Altarelli, and X. Wang, *X-ray circular dichroism and local magnetic fields*, Physical Review Letters **70**, 694–697 (1993).
- [46] M. Altarelli, *Orbital-magnetization sum rule for x-ray circular dichroism: a simple proof*, Physical Review B **47**, 597–598 (1993).
- [47] T. Jo, *X-ray magnetic circular dichroism, symmetry and orbital magnetization*, Journal of the Physical Society of Japan **62**, 1814–1815 (1993).
- [48] J. S. Hans and C. Siegmann, “Magnetism from fundamentals to nanoscale dynamics, chapter 9”, in *Solid state sciences*, edited by M. C. P. F. K. von Klitzing R. Merlin H.-J. Queisser H. Störmer (Springer, Berlin, Heidelberg, 2006), p. 372.
- [49] R. Nakajima, “X-ray magnetic circular dichroism spectroscopy in transition metal thin films”, PhD thesis (STANFORD UNIVERSITY, Jan. 1998).
- [50] B. T. Thole, G. van der Laan, J. C. Fuggle, G. A. Sawatzky, R. C. Karnatak, and J.-M. Esteve, *3d x-ray-absorption lines and the  $3d^9 4f^{n+1}$  multiplets of the lanthanides*, Physical Review B **32**, 5107–5118 (1985).
- [51] C. Piamonteze, P. Miedema, and F. M. F. de Groot, *The accuracy of the spin sum rule in XMCD*, ACS Nano **190**, 012015 (2009).
- [52] C. Piamonteze, U. Flechsig, S. Rusponi, J. Dreiser, J. Heidler, M. Schmidt, R. Wetter, M. Calvi, T. Schmidt, H. Pruchova, J. Krempasky, C. Quitmann, H. Brune, and F. Nolting, *X-Treme beamline at SLS: X-ray magnetic circular and linear dichroism at high field and low temperature*, Journal of Synchrotron Radiation **19**, 661–674 (2012).
- [53] J. Stöhr, *Nexafs spectroscopy*, in Springer series on surface science, chapter 5, Vol. 5 (1992).
- [54] A. Zabala-Lekuona, J. M. Seco, and E. Colacio, *Single-molecule magnets: from  $Mn_{12}$ -ac to dysprosium metallocenes, a travel in time*, Coordination Chemistry Reviews **441**, 213984 (2021).
- [55] R. Sessoli, D. Gatteschi, A. Caneschi, and M. A. Novak, *Magnetic bistability in a metal-ion cluster*, Nature **365**, 141–143 (1993).
- [56] A. M. Ako, I. J. Hewitt, V. Mereacre, R. Clérac, W. Wernsdorfer, C. E. Anson, and A. K. Powell, *A ferromagnetically coupled  $Mn_{19}$  aggregate with a record  $S=83/2$  ground spin state*, Angewandte Chemie International Edition **45**, 4926–4929 (2006).
- [57] J. H. V. Vleck, *The theory of electric and magnetic susceptibilities*, Nature **130**, 490–491 (1932).
- [58] P. Bruno, *Tight-binding approach to the orbital magnetic moment and magnetocrystalline anisotropy of transition-metal monolayers*, Physical Review B **39**, 865–868 (1989).

- [59] F. Neese and D. A. Pantazis, *What is not required to make a single molecule magnet*, Faraday Discuss. **148**, 229–238 (2011).
- [60] N. Ishikawa, M. Sugita, T. Ishikawa, S.-y. Koshihara, and Y. Kaizu, *Mononuclear lanthanide complexes with a long magnetization relaxation time at high temperatures: a new category of magnets at the single-molecular level*, The Journal of Physical Chemistry B **108**, 11265–11271 (2004).
- [61] D. N. Woodruff, R. E. P. Winpenny, and R. A. Layfield, *Lanthanide single-molecule magnets*, Chemical Reviews **113**, 5110–5148 (2013).
- [62] A. Dey, P. Kalita, and V. Chandrasekhar, *Lanthanide(III)-based single-ion magnets*, ACS Omega **3**, 9462–9475 (2018).
- [63] A. J. Freeman and R. E. Watson, *Theoretical investigation of some magnetic and spectroscopic properties of rare-earth ions*, Physical Review **127**, 2058–2075 (1962).
- [64] J. D. Rinehart and J. R. Long, *Exploiting single-ion anisotropy in the design of f-element single-molecule magnets*, Chemical Sciences **2**, 2078–2085 (2011).
- [65] C. A. P. Goodwin, F. Ortu, D. Reta, N. F. Chilton, and D. P. Mills, *Molecular magnetic hysteresis at 60 kelvin in dysprosocenium*, Nature **548**, 439–442 (2017).
- [66] R. S. Dante Gatteschi and J. Villain, “Molecular nanomagnets”, in *Mesoscopic physics and nanotechnology* (Oxford university press, 2006).
- [67] K. W. H. Stevens, *Matrix elements and operator equivalents connected with the magnetic properties of rare earth ions*, Proceedings of the Physical Society. Section A **65**, 209–215 (1952).
- [68] W. Wernsdorfer and R. Sessoli, *Quantum phase interference and parity effects in magnetic molecular clusters*, Science **284**, 133–135 (1999).
- [69] N. Ishikawa, M. Sugita, T. Okubo, N. Tanaka, T. Iino, and Y. Kaizu, *Determination of ligand-field parameters and f-electronic structures of double-decker bis(phthalocyaninato)lanthanide complexes*, Inorganic Chemistry **42**, 2440–2446 (2003).
- [70] N. Ishikawa, T. Iino, and Y. Kaizu, *Determination of ligand-field parameters and f-electronic structures of hetero-dinuclear phthalocyanine complexes with a diamagnetic yttrium(iii) and a paramagnetic trivalent lanthanide ion*, The Journal of Physical Chemistry A **106**, 9543–9550 (2002).
- [71] C. Hübner, B. Baxevanis, A. A. Khajetoorians, and D. Pfannkuche, *Symmetry effects on the spin switching of adatoms*, Physical Review B **90**, 155134 (2014).
- [72] M. Marciani, C. Hübner, and B. Baxevanis, *General scheme for stable single and multiatom nanomagnets according to symmetry selection rules*, Physical Review B **95**, 125433 (2017).
- [73] T. Miyamachi, T. Schuh, T. Märkl, C. Bresch, T. Balashov, A. Stöhr, C. Karlewski, S. André, M. Marthaler, M. Hoffmann, M. Geilhufe, S. Ostanin, W. Hergert, I. Mertig, G. Schön, A. Ernst, and W. Wulfhekel, *Stabilizing the magnetic moment of single holmium atoms by symmetry*, Nature **503**, 242–246 (2013).

- [74] N. F. Chilton, D. Collison, E. J. L. McInnes, R. E. P. Winpenny, and A. Soncini, *An electrostatic model for the determination of magnetic anisotropy in dysprosium complexes*, Nature Communications **4**, 2551 (2013).
- [75] J. J. Baldoví, J. M. Clemente-Juan, E. Coronado, and A. Gaita-Ariño, *Molecular anisotropy analysis of single-ion magnets using an effective electrostatic model*, Inorganic Chemistry **53**, 11323–11327 (2014).
- [76] J. J. Baldoví, J. J. Borrás-Almenar, J. M. Clemente-Juan, E. Coronado, and A. Gaita-Ariño, *Modeling the properties of lanthanoid single-ion magnets using an effective point-charge approach*, Dalton Transactions **41**, 13705–13710 (2012).
- [77] S.-D. Jiang, B.-W. Wang, and S. Gao, “Molecular nanomagnets and related phenomena”, in *Advances in lanthanide single-ion magnets*, edited by S. Gao (Springer Berlin Heidelberg, Berlin, Heidelberg, 2015), pp. 111–141.
- [78] A. Uldry, F. Vernay, and B. Delley, *Systematic computation of crystal-field multiplets for x-ray core spectroscopies*, Physical Review B **85**, 125133 (2012).
- [79] M. Hutchings, “Point-charge calculations of energy levels of magnetic ions in crystalline electric fields”, in , Vol. 16, edited by F. Seitz and D. Turnbull, Solid state physics (Academic Press, 1964), pp. 227–273.
- [80] A. Scheie, *PyCrystalField: software for calculation, analysis and fitting of crystal electric field Hamiltonians*, Journal of Applied Crystallography **54**, 356–362 (2021).
- [81] C. G. W. K. Binnemans, “Rationalization of crystal field parametrization”, in *Handbook on the physics and chemistry of rare earths*, edited by L. E. Karl A. Gschneidner (Elsevier Science B. V., Amsterdam, 1996), p. 189.
- [82] H. A. Kramers, *Théorie générale de la rotation paramagnétique dans les cristaux*, Proceedings Koninklijke Akademie van Wetenschappen **33**, 959–972 (1930).
- [83] C. Karlewski, M. Marthaler, T. Märkl, T. Balashov, W. Wulfhekel, and G. Schön, *Magnetic adatoms as memory bits: a quantum master equation analysis*, Physical Review B **91**, 245430 (2015).
- [84] A. F. Otte, “Magnetism of a single atom”, PhD thesis (Leiden University, 2008).
- [85] J. Pescia, *Elementary theory of electron spin-lattice relaxation (theory and methods of T1 measurements)*, Journal of Structural Chemistry **9**, 1002–1022 (1969).
- [86] K. N. Shrivastava, *Theory of spin-lattice relaxation*, physica status solidi (b) **117**, 437–458 (1983).
- [87] S. Loth, C. P. Lutz, and A. J. Heinrich, *Spin-polarized spin excitation spectroscopy*, New Journal of Physics **12**, 125021 (2010).
- [88] M. Mannini, F. Pineider, C. Danieli, F. Totti, L. Sorace, P. Sainctavit, M.-A. Arrio, E. Otero, L. Joly, J. C. Cezar, A. Cornia, and R. Sessoli, *Quantum tunnelling of the magnetization in a monolayer of oriented single-molecule magnets*, Nature **468**, 417–421 (2010).

- [89] T. Fukuda, N. Shigeyoshi, T. Yamamura, and N. Ishikawa, *Magnetic relaxations arising from spin-phonon interactions in the nonthermally activated temperature range for a double-decker terbium phthalocyanine single molecule magnet*, *Inorganic Chemistry* **53**, 9080–9086 (2014).
- [90] A. Fort, A. Rettori, J. Villain, D. Gatteschi, and R. Sessoli, *Mixed quantum-thermal relaxation in Mn<sub>12</sub> acetate molecules*, *Physical Review Letters* **80**, 612–615 (1998).
- [91] D. A. Garanin and E. M. Chudnovsky, *Angular momentum in spin-phonon processes*, *Physical Review B* **92**, 024421 (2015).
- [92] D. Gatteschi and R. Sessoli, *Quantum tunneling of magnetization and related phenomena in molecular materials*, *Angewandte Chemie International Edition* **42**, 268–297 (2003).
- [93] R. Orbach and B. Bleaney, *Spin-lattice relaxation in rare-earth salts*, *Proceedings of the Royal Society of London. Series A. Mathematical and Physical Sciences* **264**, 458–484 (1961).
- [94] P. L. Scott and C. D. Jeffries, *Spin-lattice relaxation in some rare-earth salts at helium temperatures; observation of the phonon bottleneck*, *Physical Review* **127**, 32–51 (1962).
- [95] G. H. Larson and C. D. Jeffries, *Spin-lattice relaxation in some rare-earth salts. i. temperature dependence*, *Physical Review* **141**, 461–478 (1966).
- [96] G. H. Larson and C. D. Jeffries, *Spin-lattice relaxation in some rare-earth salts. ii. angular dependence, hyperfine effects, and cross relaxation*, *Physical Review* **145**, 311–324 (1966).
- [97] F. Donati, S. Rusponi, S. Stepanow, L. Persichetti, A. Singha, D. M. Juraschek, C. Wäckerlin, R. Baltic, M. Pivetta, K. Diller, C. Nistor, J. Dreiser, K. Kummer, E. Velez-Fort, N. A. Spaldin, H. Brune, and P. Gambardella, *Unconventional spin relaxation involving localized vibrational modes in Ho single-atom magnets*, *Physical Review Letters* **124**, 077204 (2020).
- [98] F. D. Natterer, F. Donati, F. Patthey, and H. Brune, *Thermal and magnetic-field stability of holmium single-atom magnets*, *Physical Review Letters* **121**, 027201 (2018).
- [99] H. Brune, M. Giovannini, K. Bromann, and K. Kern, *Self-organized growth of nanostructure arrays on strain-relief patterns*, *Nature* **394**, 451–453 (1998).
- [100] F. Silly, M. Pivetta, M. Ternes, F. Patthey, J. P. Pelz, and W.-D. Schneider, *Creation of an atomic superlattice by immersing metallic adatoms in a two-dimensional electron sea*, *Physical Review Letters* **92**, 016101 (2004).
- [101] A. T. N'Diaye, S. Bleikamp, P. J. Feibelman, and T. Michely, *Two-dimensional Ir cluster lattice on a graphene moiré on Ir(111)*, *Physical Review Letters* **97**, 215501 (2006).
- [102] M. Pivetta, S. Rusponi, and H. Brune, *Direct capture and electrostatic repulsion in the self-assembly of rare-earth atom superlattices on graphene*, *Physical Review B* **98**, 115417 (2018).
- [103] J. Barth, *Transport of adsorbates at metal surfaces: from thermal migration to hot precursors*, *Surface Science Reports* **40**, 75–149 (2000).

## Bibliography

---

- [104] J. Weckesser, J. V. Barth, and K. Kern, *Direct observation of surface diffusion of large organic molecules at metal surfaces: PVBA on Pd(110)*, The Journal of Chemical Physics **110**, 5351–5354 (1999).
- [105] J. V. Barth, *Molecular architectonic on metal surfaces*, Annual Review of Physical Chemistry **58**, 375–407 (2007).
- [106] J. V. Barth, J. Weckesser, C. Cai, P. Günter, L. Bürgi, O. Jeandupeux, and K. Kern, *Building supramolecular nanostructures at surfaces by hydrogen bonding*, Angewandte Chemie International Edition **39**, 1230–1234 (2000).
- [107] T. Yokoyama, S. Yokoyama, T. Kamikado, Y. Okuno, and S. Mashiko, *Selective assembly on a surface of supramolecular aggregates with controlled size and shape*, Nature **413**, 619–621 (2001).
- [108] J. V. Barth, J. Weckesser, G. Trimarchi, M. Vladimirova, A. De Vita, C. Cai, H. Brune, P. Günter, and K. Kern, *Stereochemical effects in supramolecular self-assembly at surfaces: 1-D versus 2-D enantiomorphic ordering for PVBA and PEBA on Ag(111)*, Journal of the American Chemical Society **124**, 7991–8000 (2002).
- [109] J. V. Barth, J. Weckesser, N. Lin, A. Dmitriev, and K. Kern, *Supramolecular architectures and nanostructures at metal surfaces*, Applied Physics A **76**, 645–652 (2003).
- [110] M.-C. Blüm, E. Čavar, M. Pivetta, F. Patthey, and W.-D. Schneider, *Conservation of chirality in a hierarchical supramolecular self-assembled structure with pentagonal symmetry*, Angewandte Chemie International Edition **44**, 5334–5337 (2005).
- [111] J. Liu, P. Ruffieux, X. Feng, K. Müllen, and R. Fasel, *Cyclotrimerization of arylalkynes on Au(111)*, Chemical Communications **50**, 11200–11203 (2014).
- [112] T. A. Jung, R. R. Schlittler, and J. K. Gimzewski, *Conformational identification of individual adsorbed molecules with the STM*, Nature **386**, 696–698 (1997).
- [113] W. Auwärter, A. Weber-Bargioni, S. Brink, A. Riemann, A. Schiffrin, M. Ruben, and J. V. Barth, *Controlled metalation of self-assembled porphyrin nanoarrays in two dimensions*, ChemPhysChem **8**, 250–254 (2007).
- [114] K. Diller, A. Singha, M. Pivetta, C. Wäckerlin, R. Hellwig, A. Verdini, A. Cossaro, L. Floreano, E. Vélez-Fort, J. Dreiser, S. Rusponi, and H. Brune, *Magnetic properties of on-surface synthesized single-ion molecular magnets*, RSC Advances **9**, 34421–34429 (2019).
- [115] N. Lin, A. Dmitriev, H. Spillmann, P. Messina, M. Lingenfelder, S. Stepanow, J. V. Barth, and K. Kern, *Supramolecular engineering of metal-organic networks at surfaces*, AIP Conference Proceedings **696**, 144–149 (2003).
- [116] A. Dmitriev, H. Spillmann, N. Lin, J. V. Barth, and K. Kern, *Modular assembly of two-dimensional metal–organic coordination networks at a metal surface*, Angewandte Chemie International Edition **42**, 2670–2673 (2003).

- [117] M. A. Lingenfelder, H. Spillmann, A. Dmitriev, S. Stepanow, N. Lin, J. V. Barth, and K. Kern, *Towards surface-supported supramolecular architectures: tailored coordination assembly of 1,4-Benzenedicarboxylate and Fe on Cu(100)*, Chemistry – A European Journal **10**, 1913–1919 (2004).
- [118] S. Stepanow, N. Lin, and J. V. Barth, *Modular assembly of low-dimensional coordination architectures on metal surfaces*, Journal of Physics: Condensed Matter **20**, 184002 (2008).
- [119] P. Gambardella, S. Stepanow, A. Dmitriev, J. Honolka, F. M. F. de Groot, M. Lingenfelder, S. S. Gupta, D. D. Sarma, P. Bencok, S. Stanescu, S. Clair, S. Pons, N. Lin, A. P. Seitsonen, H. Brune, J. V. Barth, and K. Kern, *Supramolecular control of the magnetic anisotropy in two-dimensional high-spin Fe arrays at a metal interface*, Nature Materials **8**, 189–193 (2009).
- [120] S. Clair, S. Pons, H. Brune, K. Kern, and J. V. Barth, *Mesoscopic metallosupramolecular texturing by hierarchic assembly*, Angewandte Chemie International Edition **44**, 7294–7297 (2005).
- [121] N. Lin, S. Stepanow, F. Vidal, K. Kern, M. S. Alam, S. Strömsdörfer, V. Dremov, P. Müller, A. Landa, and M. Ruben, *Surface-assisted coordination chemistry and self-assembly*, Dalton Transactions, 2794–2800 (2006).
- [122] S. Stepanow, N. Lin, D. Payer, U. Schlickum, F. Klappenberger, G. Zoppellaro, M. Ruben, H. Brune, J. V. Barth, and K. Kern, *Surface-assisted assembly of 2D metal–organic networks that exhibit unusual threefold coordination symmetry*, Angewandte Chemie International Edition **46**, 710–713 (2007).
- [123] Q. Sun, L. Cai, H. Ma, C. Yuan, and W. Xu, *On-surface construction of a metal–organic sierpiński triangle*, Chemical Communications **51**, 14164–14166 (2015).
- [124] D. Écija, J. I. Urgel, A. C. Papageorgiou, S. Joshi, W. Auwärter, A. P. Seitsonen, S. Klyatskaya, M. Ruben, S. Fischer, S. Vijayaraghavan, J. Reichert, and J. V. Barth, *Five-vertex archimedean surface tessellation by lanthanide-directed molecular self-assembly*, Proceedings of the National Academy of Sciences **110**, 6678–6681 (2013).
- [125] G. Lyu, Q. Zhang, J. I. Urgel, G. Kuang, W. Auwärter, D. Ecija, J. V. Barth, and N. Lin, *Tunable lanthanide-directed metallosupramolecular networks by exploiting coordinative flexibility through ligand stoichiometry*, Chemical Communications **52**, 1618–1621 (2016).
- [126] D. Écija, J. I. Urgel, A. P. Seitsonen, W. Auwärter, and J. V. Barth, *Lanthanide-directed assembly of interfacial coordination architectures—from complex networks to functional nanosystems*, Accounts of Chemical Research **51**, 365–375 (2018).
- [127] J. I. Urgel, B. Cirera, Y. Wang, W. Auwärter, R. Otero, J. M. Gallego, M. Alcamí, S. Klyatskaya, M. Ruben, F. Martín, R. Miranda, D. Ecija, and J. V. Barth, *Surface-supported robust 2D lanthanide-carboxylate coordination networks*, Small **11**, 6358–6364 (2015).

## Bibliography

---

- [128] S. Stepanow, M. Lingenfelder, A. Dmitriev, H. Spillmann, E. Delvigne, N. Lin, X. Deng, C. Cai, J. V. Barth, and K. Kern, *Steering molecular organization and host–guest interactions using two-dimensional nanoporous coordination systems*, *Nature Materials* **3**, 229–233 (2004).
- [129] M. Pivetta, G. E. Pacchioni, U. Schlickum, J. V. Barth, and H. Brune, *Formation of Fe cluster superlattice in a metal-organic quantum-box network*, *Physical Review Letters* **110**, 086102 (2013).
- [130] P. Gambardella, A. Dallmeyer, K. Maiti, M. C. Malagoli, W. Eberhardt, K. Kern, and C. Carbone, *Ferromagnetism in one-dimensional monatomic metal chains*, *Nature* **416**, 301–304 (2002).
- [131] M. Mannini, F. Pineider, P. Saintavit, C. Danieli, E. Otero, C. Sciancalepore, A. M. Talarico, M.-A. Arrio, A. Cornia, D. Gatteschi, and R. Sessoli, *Magnetic memory of a single-molecule quantum magnet wired to a gold surface*, *Nature Materials* **8**, 194–197 (2009).
- [132] M. Steinbrecher, A. Sonntag, M. d. S. Dias, M. Bouhassoune, S. Lounis, J. Wiebe, R. Wiesendanger, and A. A. Khajetoorians, *Absence of a spin-signature from a single Ho adatom as probed by spin-sensitive tunneling*, *Nature Communications* **7**, 10454 (2016).
- [133] A. Singha, F. Donati, C. Wäckerlin, R. Baltic, J. Dreiser, M. Pivetta, S. Rusponi, and H. Brune, *Magnetic hysteresis in Er trimers on Cu(111)*, *Nano Letters* **16**, 3475–3481 (2016).
- [134] S. Voss, M. Burgert, M. Fonin, U. Groth, and U. Rüdiger, *A comparative study on the deposition of Mn<sub>12</sub> single molecule magnets on the Au(111) surface*, *Dalton Transactions*, 499–505 (2008).
- [135] M. Mannini, F. Bertani, C. Tudisco, L. Malavolti, L. Poggini, K. Misztal, D. Menozzi, A. Motta, E. Otero, P. Ohresser, P. Saintavit, G. G. Condorelli, E. Dalcanele, and R. Sessoli, *Magnetic behaviour of TbPc<sub>2</sub> single-molecule magnets chemically grafted on silicon surface*, *Nature Communications* **5**, 4582 (2014).
- [136] L. Margheriti, D. Chiappe, M. Mannini, P.-E. Car, P. Saintavit, M.-A. Arrio, F. B. de Mongeot, J. C. Cezar, F. M. Piras, A. Magnani, E. Otero, A. Caneschi, and R. Sessoli, *X-ray detected magnetic hysteresis of thermally evaporated terbium double-decker oriented films*, *Advanced Materials* **22**, 5488–5493 (2010).
- [137] S. Stepanow, J. Honolka, P. Gambardella, L. Vitali, N. Abdurakhmanova, T.-C. Tseng, S. Rauschenbach, S. L. Tait, V. Sessi, S. Klyatskaya, M. Ruben, and K. Kern, *Spin and orbital magnetic moment anisotropies of monodispersed bis(phthalocyaninato)terbium on a copper surface*, *Journal of the American Chemical Society* **132**, 11900–11901 (2010).
- [138] A. Cornia and M. Mannini, “Single-molecule magnets on surfaces”, in *Molecular nano-magnets and related phenomena*, edited by S. Gao (Springer Berlin Heidelberg, Berlin, Heidelberg, 2015), pp. 293–330.



- [139] J. I. Urgel, M. Schwarz, M. Garnica, D. Stassen, D. Bonifazi, D. Eciija, J. V. Barth, and W. Auwärter, *Controlling coordination reactions and assembly on a Cu(111) supported boron nitride monolayer*, Journal of the American Chemical Society **137**, 2420–2423 (2015).
- [140] J. Li, L. Solianyik, N. Schmidt, B. Baker, S. Gottardi, J. C. Moreno Lopez, M. Enache, L. Monjas, R. van der Vlag, R. W. A. Havenith, A. K. H. Hirsch, and M. Stöhr, *Low-dimensional metal–organic coordination structures on graphene*, The Journal of Physical Chemistry C **123**, 12730–12735 (2019).
- [141] A. Kumar, K. Banerjee, A. S. Foster, and P. Liljeroth, *Two-dimensional band structure in honeycomb metal–organic frameworks*, Nano Letters **18**, 5596–5602 (2018).
- [142] D. Moreno, B. Cirera, S. O. Parreiras, J. I. Urgel, N. Giménez-Agulló, K. Lauwaet, J. M. Gallego, J. R. Galán-Mascarós, J. I. Martínez, P. Ballester, R. Miranda, and D. Écija, *Dysprosium-directed metallosupramolecular network on graphene /Ir(111)*, Chemical Communications **57**, 1380–1383 (2021).
- [143] H. Walch, J. Dienstmaier, G. Eder, R. Gutzler, S. Schlögl, T. Sirtl, K. Das, M. Schmittl, and M. Lackinger, *Extended two-dimensional metal–organic frameworks based on thiolate–copper coordination bonds*, Journal of the American Chemical Society **133**, 7909–7915 (2011).
- [144] Z. Shi and N. Lin, *Self-assembly of a two-dimensional bimetallic coordination framework and dynamic control of reversible conversions to homo-metallic hydrogen-bond arrays*, ChemPhysChem **11**, 97–100 (2010).
- [145] H. Tsuruta, T. Imamoto, and K. Yamaguchi, *Evaluation of the relative lewis acidities of lanthanoid(iii) compounds by tandem mass spectrometry*, Chemical Communications, 1703–1704 (1999).
- [146] M. Uphoff, G. S. Michelitsch, R. Hellwig, K. Reuter, H. Brune, F. Klappenberger, and J. V. Barth, *Assembly of robust holmium-directed 2D metal–organic coordination complexes and networks on the Ag(100) surface*, ACS Nano **12**, 11552–11560 (2018).
- [147] J. Heintz, C. Durand, H. Tang, and R. Coratger, *Control of the deprotonation of terephthalic acid assemblies on Ag(111) studied by DFT calculations and low temperature scanning tunneling microscopy*, Physical Chemistry Chemical Physics **22**, 3173–3183 (2020).
- [148] B. Quiroga Argañaraz, L. J. Cristina, L. M. Rodríguez, A. Cossaro, A. Verdini, L. Floreano, J. D. Fuhr, J. E. Gayone, and H. Ascolani, *Ubiquitous deprotonation of terephthalic acid in the self-assembled phases on Cu(100)*, Physical Chemistry Chemical Physics **20**, 4329–4339 (2018).
- [149] S. Stepanow, T. Strunskus, M. Lingenfelder, A. Dmitriev, H. Spillmann, N. Lin, J. V. Barth, C. Wöll, and K. Kern, *Deprotonation-driven phase transformations in terephthalic acid self-assembly on Cu(100)*, The Journal of Physical Chemistry B **108**, 19392–19397 (2004).

## Bibliography

---

- [150] T. Schmitt, L. Hammer, and M. A. Schneider, *Evidence for on-site carboxylation in the self-assembly of 4,4-biphenyl dicarboxylic acid on Cu(111)*, The Journal of Physical Chemistry C **120**, 1043–1048 (2016).
- [151] N. Zhu, T. Osada, and T. Komeda, *Supramolecular assembly of biphenyl dicarboxylic acid on Au(111)*, Surface Science **601**, 1789–1794 (2007).
- [152] U. Schlickum, R. Decker, F. Klappenberger, G. Zoppellaro, S. Klyatskaya, W. Auwärter, S. Neppel, K. Kern, H. Brune, M. Ruben, and J. V. Barth, *Chiral kagomé lattice from simple ditopic molecular bricks*, Journal of the American Chemical Society **130**, 11778–11782 (2008).
- [153] S. Klyatskaya, F. Klappenberger, U. Schlickum, D. Kühne, M. Marschall, J. Reichert, R. Decker, W. Krenner, G. Zoppellaro, H. Brune, J. V. Barth, and M. Ruben, *Surface-confined self-assembly of di-carbonitrile polyphenyls*, Advanced Functional Materials **21**, 1230–1240 (2011).
- [154] M. Pivetta, G. E. Pacchioni, E. Fernandes, and H. Brune, *Temperature-dependent self-assembly of nc-ph5-cn molecules on cu(111)*, The Journal of Chemical Physics **142**, 101928 (2015).
- [155] U. Schlickum, R. Decker, F. Klappenberger, G. Zoppellaro, S. Klyatskaya, M. Ruben, I. Silanes, A. Arnau, K. Kern, H. Brune, and J. V. Barth, *Metal-organic honeycomb nanomeshes with tunable cavity size*, Nano Letters **7**, 3813–3817 (2007).
- [156] D. Kühne, F. Klappenberger, R. Decker, U. Schlickum, H. Brune, S. Klyatskaya, M. Ruben, and J. V. Barth, *High-quality 2D metal-organic coordination network providing giant cavities within mesoscale domains*, Journal of the American Chemical Society **131**, 3881–3883 (2009).
- [157] G. E. Pacchioni, M. Pivetta, and H. Brune, *Competing interactions in the self-assembly of NC-Ph<sub>3</sub>-CN molecules on Cu(111)*, The Journal of Physical Chemistry C **119**, 25442–25448 (2015).
- [158] F. Klappenberger, D. Kühne, W. Krenner, I. Silanes, A. Arnau, F. J. García de Abajo, S. Klyatskaya, M. Ruben, and J. V. Barth, *Tunable quantum dot arrays formed from self-assembled metal-organic networks*, Physical Review Letters **106**, 026802 (2011).
- [159] T. Sirtl, S. Schlögl, A. Rastgoo-Lahrood, J. Jelic, S. Neogi, M. Schmittel, W. M. Heckl, K. Reuter, and M. Lackinger, *Control of intermolecular bonds by deposition rates at room temperature: hydrogen bonds versus metal coordination in trinitrile monolayers*, Journal of the American Chemical Society **135**, 691–695 (2013).
- [160] N. Schmidt, J. Li, S. Gottardi, J. C. Moreno-Lopez, M. Enache, L. Monjas, R. van der Vlag, R. W. A. Havenith, A. K. H. Hirsch, and M. Stöhr, *Comparing the self-assembly of sexiphenyl-dicarbonitrile on graphite and graphene on Cu(111)*, Chemistry – A European Journal **25**, 5065–5070 (2019).
- [161] J. M. Gottfried, *Surface chemistry of porphyrins and phthalocyanines*, Surface Science Reports **70**, 259–379 (2015).

- [162] G. Rojas, X. Chen, C. Bravo, J.-H. Kim, J.-S. Kim, J. Xiao, P. A. Dowben, Y. Gao, X. C. Zeng, W. Choe, and A. Enders, *Self-assembly and properties of nonmetalated tetraphenyl-porphyrin on metal substrates*, The Journal of Physical Chemistry C **114**, 9408–9415 (2010).
- [163] F. Buchner, E. Zillner, M. Röckert, S. Gläsel, H.-P. Steinrück, and H. Marbach, *Substrate-mediated phase separation of two porphyrin derivatives on Cu(111)*, Chemistry – A European Journal **17**, 10226–10229 (2011).
- [164] M. Eichberger, M. Marschall, J. Reichert, A. Weber-Bargioni, W. Auwärter, R. L. C. Wang, H. J. Kreuzer, Y. Pennec, A. Schiffrin, and J. V. Barth, *Dimerization boosts one-dimensional mobility of conformationally adapted porphyrins on a hexagonal surface atomic lattice*, Nano Letters **8**, 4608–4613 (2008).
- [165] Z. Shi and N. Lin, *Self-assembly fabrication of two-dimensional nano-networks of porphyrin-based molecules*, in 2010 3rd international nanoelectronics conference (inec) (2010), pp. 991–991.
- [166] W. Auwärter, A. Weber-Bargioni, A. Riemann, A. Schiffrin, O. Gröning, R. Fasel, and J. V. Barth, *Self-assembly and conformation of tetrapyrrolyl-porphyrin molecules on Ag(111)*, The Journal of Chemical Physics **124**, 194708 (2006).
- [167] D. M. Roessler and W. C. Walker, *Electronic spectrum and ultraviolet optical properties of crystalline MgO*, Physical Review **159**, 733–738 (1967).
- [168] V. E. Henrich, G. Dresselhaus, and H. J. Zeiger, *Energy-dependent electron-energy-loss spectroscopy: application to the surface and bulk electronic structure of MgO*, Physical Review B **22**, 4764–4775 (1980).
- [169] S. Schintke, S. Messerli, M. Pivetta, F. Patthey, L. Libioulle, M. Stengel, A. De Vita, and W.-D. Schneider, *Insulator at the ultrathin limit: MgO on Ag(001)*, Physical Review Letters **87**, 276801 (2001).
- [170] M. J. L. Sangster, G. Peckham, and D. H. Saunderson, *Lattice dynamics of magnesium oxide*, Journal of Physics C **3**, 1026–1036 (1970).
- [171] J. Pal, M. Smerieri, E. Celasco, L. Savio, L. Vattuone, and M. Rocca, *Morphology of monolayer MgO films on Ag(100): switching from corrugated islands to extended flat terraces*, Physical Review Letters **112**, 126102 (2014).
- [172] E. Fernandes, F. Donati, F. Patthey, S. Stavrič, Ž. Šljivančanin, and H. Brune, *Adsorption sites of individual metal atoms on ultrathin MgO(100) films*, Physical Review B **96**, 045419 (2017).
- [173] F. Donati, M. Pivetta, C. Wolf, A. Singha, C. Wäckerlin, R. Baltic, E. Fernandes, J.-G. de Groot, S. L. Ahmed, L. Persichetti, C. Nistor, J. Dreiser, A. Barla, P. Gambardella, H. Brune, and S. Rusponi, *Correlation between electronic configuration and magnetic stability in dysprosium single atom magnets*, Nano Letters **21**, 8266–8273 (2021).

## Bibliography

---

- [174] I. G. Rau, S. Baumann, S. Rusponi, F. Donati, S. Stepanow, L. Gragnaniello, J. Dreiser, C. Piamonteze, F. Nolting, S. Gangopadhyay, O. R. Albertini, R. M. Macfarlane, C. P. Lutz, B. A. Jones, P. Gambardella, A. J. Heinrich, and H. Brune, *Reaching the magnetic anisotropy limit of a 3d metal atom*, Science **344**, 988–992 (2014).
- [175] S. Baumann, F. Donati, S. Stepanow, S. Rusponi, W. Paul, S. Gangopadhyay, I. G. Rau, G. E. Pacchioni, L. Gragnaniello, M. Pivetta, J. Dreiser, C. Piamonteze, C. P. Lutz, R. M. Macfarlane, B. A. Jones, P. Gambardella, A. J. Heinrich, and H. Brune, *Origin of perpendicular magnetic anisotropy and large orbital moment in Fe atoms on MgO*, Physical Review Letters **115**, 237202 (2015).
- [176] M. Uphoff, “Atomistic investigations and control of novel quantum materials: lanthanide-organic nano-architectures at well-defined substrates and the iron silicide (110) facet”, PhD thesis (TUM, 2019).
- [177] I. S. Messaoudi, A. Zaoui, and M. Ferhat, *Band-gap and phonon distribution in alkali halides*, physica status solidi (b) **252**, 490–495 (2015).
- [178] G. Raunio and S. Rolandson, *Lattice dynamics of NaCl, KCl, RbCl, and RbF*, Physical Review B **2**, 2098–2103 (1970).
- [179] J. Repp, G. Meyer, and K.-H. Rieder, *Snell’s law for surface electrons: refraction of an electron gas imaged in real space*, Physical Review Letters **92**, 036803 (2004).
- [180] M. Pivetta, F. Patthey, M. Stengel, A. Baldereschi, and W.-D. Schneider, *Local work function moiré pattern on ultrathin ionic films: NaCl on Ag(100)*, Physical Review B **72**, 115404 (2005).
- [181] F. Matthaei, S. Heidorn, K. Boom, C. Bertram, A. Safiei, J. Henzl, and K. Morgenstern, *Coulomb attraction during the carpet growth mode of NaCl*, Journal of Physics: Condensed Matter **24**, 354006 (2012).
- [182] H.-C. Ploigt, C. Brun, M. Pivetta, F. Patthey, and W.-D. Schneider, *Local work function changes determined by field emission resonances: NaCl-Ag(100)*, Physical Review B **76**, 195404 (2007).
- [183] J. Repp, G. Meyer, S. M. Stojković, A. Gourdon, and C. Joachim, *Molecules on insulating films: scanning-tunneling microscopy imaging of individual molecular orbitals*, Physical Review Letters **94**, 026803 (2005).
- [184] J. Repp, G. Meyer, F. E. Olsson, and M. Persson, *Controlling the charge state of individual gold adatoms*, Science **305**, 493–495 (2004).
- [185] N. Li, H. Wang, D.-L. Song, C. Li, R. Li, S.-M. Hou, Y.-F. Wang, and R. Berndt, *Charging single Co atoms on ultrathin NaCl films*, Dalton Transactions **45**, 16566–16569 (2016).
- [186] C. Chen, P. Ding, M. Mura, Y. Chen, Y. Sun, L. N. Kantorovich, H. Gersen, F. Besenbacher, and M. Yu, *Formation of hypoxanthine tetrad by reaction with sodium chloride: from planar to stereo*, Angewandte Chemie International Edition **57**, 16015–16019 (2018).
- [187] D. Skomski, S. Abb, and S. L. Tait, *Robust surface nano-architecture by alkali-carboxylate ionic bonding*, Journal of the American Chemical Society **134**, 14165–14171 (2012).

- [188] D. Skomski and S. L. Tait, *Ordered and robust ionic surface networks from weakly interacting carboxyl building blocks*, The Journal of Physical Chemistry C **117**, 2959–2965 (2013).
- [189] J. Hieulle, D. Peyrot, Z. Jiang, and F. Silly, *Engineering two-dimensional hybrid nacl–organic coordinated nanoarchitectures on metal surfaces*, Chemical Communications **51**, 13162–13165 (2015).
- [190] C. Wäckerlin, C. Iacovita, D. Chylarecka, P. Fesser, T. A. Jung, and N. Ballav, *Assembly of 2D ionic layers by reaction of alkali halides with the organic electrophile 7,7,8,8-tetracyano-p-quinodimethane (TCNQ)*, Chemical Communications **47**, 9146–9148 (2011).
- [191] P. R. Wallace, *The band theory of graphite*, Physical Review **71**, 622–634 (1947).
- [192] M. Endlich, A. Molina-Sánchez, L. Wirtz, and J. Kröger, *Screening of electron-phonon coupling in graphene on Ir(111)*, Physical Review B **88**, 205403 (2013).
- [193] J. Maultzsch, S. Reich, C. Thomsen, H. Requardt, and P. Ordejón, *Phonon dispersion in graphite*, Physical Review Letters **92**, 075501 (2004).
- [194] M.-L. B. J. Wintterlin, *Graphene on metal surfaces*, Surface Science **603**, 1841–1852 (2009).
- [195] F. Donati, L. Gagnaniello, A. Cavallin, F. D. Natterer, Q. Dubout, M. Pivetta, F. Patthey, J. Dreiser, C. Piamonteze, S. Rusponi, and H. Brune, *Tailoring the magnetism of Co atoms on graphene through substrate hybridization*, Physical Review Letters **113**, 177201 (2014).
- [196] S. Rusponi, M. Papagno, P. Moras, S. Vlaic, M. Etzkorn, P. M. Sheverdyaeva, D. Pacilé, H. Brune, and C. Carbone, *Highly anisotropic dirac cones in epitaxial graphene modulated by an island superlattice*, Physical Review Letters **105**, 246803 (2010).
- [197] M. Endlich, S. Gozdzik, N. Néel, A. L. da Rosa, T. Frauenheim, T. O. Wehling, and J. Kröger, *Phthalocyanine adsorption to graphene on Ir(111): evidence for decoupling from vibrational spectroscopy*, The Journal of Chemical Physics **141**, 184308 (2014).
- [198] L. Gagnaniello, F. Paschke, P. Erler, P. Schmitt, N. Barth, S. Simon, H. Brune, S. Rusponi, and M. Fonin, *Uniaxial 2D superlattice of Fe<sub>4</sub> molecular magnets on graphene*, Nano Letters **17**, 7177–7182 (2017).
- [199] F. Donati, Q. Dubout, G. Autès, F. Patthey, F. Calleja, P. Gambardella, O. V. Yazyev, and H. Brune, *Magnetic moment and anisotropy of individual Co atoms on graphene*, Physical Review Letters **111**, 236801 (2013).
- [200] J. Dreiser, G. E. Pacchioni, F. Donati, L. Gagnaniello, A. Cavallin, K. S. Pedersen, J. Bendix, B. Delley, M. Pivetta, S. Rusponi, and H. Brune, *Out-of-plane alignment of Er(trensai) easy magnetization axes using graphene*, ACS Nano **10**, 2887–2892 (2016).
- [201] J. M. MacLeod and F. Rosei, *Molecular self-assembly on graphene*, Small **10**, 1038–1049 (2014).

## Bibliography

---

- [202] W. Zhang, A. Nefedov, M. Naboka, L. Cao, and C. Wöll, *Molecular orientation of terephthalic acid assembly on epitaxial graphene: NEXAFS and XPS study*, Physical Chemistry Chemical Physics **14**, 10125–10131 (2012).
- [203] F. Buchner, I. Kellner, W. Hieringer, A. Görling, H.-P. Steinrück, and H. Marbach, *Ordering aspects and intramolecular conformation of tetraphenylporphyrins on Ag(111)*, Physical Chemistry Chemical Physics **12**, 13082–13090 (2010).
- [204] A. Singha, R. Baltic, F. Donati, C. Wäckerlin, J. Dreiser, L. Persichetti, S. Stepanow, P. Gambardella, S. Rusponi, and H. Brune, *4f Occupancy and magnetism of rare-earth atoms adsorbed on metal substrates*, Physical Review B **96**, 224418 (2017).
- [205] P. Zhang, L. Zhang, C. Wang, S. Xue, S.-Y. Lin, and J. Tang, *Equatorially coordinated lanthanide single ion magnets*, Journal of the American Chemical Society **136**, 4484–4487 (2014).
- [206] S.-D. Jiang, B.-W. Wang, H.-L. Sun, Z.-M. Wang, and S. Gao, *An organometallic single-ion magnet*, Journal of the American Chemical Society **133**, 4730–4733 (2011).
- [207] K. R. Meihaus and J. R. Long, *Magnetic blocking at 10 K and a dipolar-mediated avalanche in salts of the bis( $\eta_8$ -cyclooctatetraenide) complex  $[\text{Er}(\text{COT})_2]^-$* , Journal of the American Chemical Society **135**, 17952–17957 (2013).
- [208] J. J. Le Roy, I. Korobkov, and M. Murugesu, *A sandwich complex with axial symmetry for harnessing the anisotropy in a prolate erbium(III) ion*, Chemical Communications **50**, 1602–1604 (2014).
- [209] P. Zhang, Y.-N. Guo, and J. Tang, *Recent advances in dysprosium-based single molecule magnets: structural overview and synthetic strategies*, Coordination Chemistry Reviews **257**, 1728–1763 (2013).
- [210] S. O. Parreiras, D. Moreno, B. Cirera, M. A. Valbuena, J. I. Urgel, M. Paradinas, M. Panighel, F. Ajejas, M. A. Niño, J. M. Gallego, M. Valvidares, P. Gargiani, W. Kuch, J. I. Martínez, A. Mugarza, J. Camarero, R. Miranda, P. Perna, and D. Écija, *Tuning the magnetic anisotropy of lanthanides on a metal substrate by metal–organic coordination*, Small **17**, 2102753 (2021).
- [211] R. Baltic, F. Donati, A. Singha, C. Wäckerlin, J. Dreiser, B. Delley, M. Pivetta, S. Rusponi, and H. Brune, *Magnetic properties of single rare-earth atoms on graphene/Ir(111)*, Physical Review B **98**, 024412 (2018).
- [212] M. Studniarek, C. Wäckerlin, A. Singha, R. Baltic, K. Diller, F. Donati, S. Rusponi, H. Brune, Y. Lan, S. Klyatskaya, M. Ruben, A. P. Seitsonen, and J. Dreiser, *Understanding the superior stability of single-molecule magnets on an oxide film*, Advanced Science **6**, 1901736 (2019).
- [213] F. Donati, A. Singha, S. Stepanow, C. Wäckerlin, J. Dreiser, P. Gambardella, S. Rusponi, and H. Brune, *Magnetism of Ho and Er atoms on close-packed metal surfaces*, Physical Review Letters **113**, 237201 (2014).

- [214] J. Sievers, *Asphericity of 4f-shells in their Hund's rule ground states*, Zeitschrift für Physik B Condensed Matter **45**, 289–296 (1982).
- [215] C. A. P. Goodwin, D. Reta, F. Ortu, N. F. Chilton, and D. P. Mills, *Synthesis and electronic structures of heavy lanthanide metallocenium cations*, Journal of the American Chemical Society **139**, 18714–18724 (2017).
- [216] D. Aravena and E. Ruiz, *Shedding light on the single-molecule magnet behavior of mononuclear Dy<sup>III</sup> complexes*, Inorganic Chemistry **52**, 13770–13778 (2013).
- [217] A. J. Brown, D. Pinkowicz, M. R. Saber, and K. R. Dunbar, *A trigonal-pyramidal erbium(III) single-molecule magnet*, Angewandte Chemie International Edition **54**, 5864–5868 (2015).
- [218] G. Cucinotta, M. Perfetti, J. Luzon, M. Etienne, P.-E. Car, A. Caneschi, G. Calvez, K. Bernot, and R. Sessoli, *Magnetic anisotropy in a dysprosium/dota single-molecule magnet: beyond simple magneto-structural correlations*, Angewandte Chemie International Edition **51**, 1606–1610 (2012).
- [219] N. Ishikawa, M. Sugita, and W. W., *Quantum tunneling of magnetization in lanthanide single-molecule magnets: bis (phthalocyaninato)terbium and bis (phthalocyaninato) dysprosium anions*, Angew. Chem. Int. Ed **44**, 2931–2935 (2005).
- [220] C. A. Gould, K. R. McClain, J. M. Yu, T. J. Groshens, F. Furche, B. G. Harvey, and J. R. Long, *Synthesis and magnetism of neutral, linear metallocene complexes of terbium(II) and dysprosium(II)*, J. Am. Chem. Soc. **141**, 12967 (2019).
- [221] J. Repp, S. Fölsch, G. Meyer, and K.-H. Rieder, *Ionic films on vicinal metal surfaces: Enhanced binding due to charge modulation*, Physical Review Letters **86**, 252–255 (2001).
- [222] W. Hebenstreit, J. Redinger, Z. Horozova, M. Schmid, R. Podlucky, and P. Varga, *Atomic resolution by stm on ultra-thin films of alkali halides: experiment and local density calculations*, Surface Science **424** (1999).
- [223] Z. Li, K. Schouteden, V. Iancu, E. Janssens, P. Lievens, C. Van Haesendonck, and J. I. Cerdá, *Chemically modified STM tips for atomic-resolution imaging of ultrathin NaCl films*, Nano Research **8**, 2223–2230 (2015).
- [224] E. Fernandes, “Adsorption sites of metal atoms on MgO thin films and rotational quantum state spectroscopy of physisorbed H<sub>2</sub>”, PhD thesis (EPFL, 2017).
- [225] J. H. Van Vleck, *Paramagnetic relaxation and the equilibrium of lattice oscillators*, Physical Review **59**, 724–729 (1941).
- [226] K. W. H. Stevens, *The theory of paramagnetic relaxation*, Reports on Progress in Physics **30**, 189–226 (1967).
- [227] A. M. Stoneham, *The phonon bottleneck in paramagnetic crystals*, Proceedings of the Physical Society **86**, 1163–1177 (1965).
- [228] J. C. Gill, *The establishment of thermal equilibrium in paramagnetic crystals*, Report on Progress in Physics **38**, 91–150 (1975).

## Bibliography

---

- [229] I. Chiorescu, W. Wernsdorfer, A. Müller, H. Bögge, and B. Barbara, *Butterfly hysteresis loop and dissipative spin reversal in the  $S = 1/2$ ,  $V_{15}$  molecular complex*, Physical Review Letters **84**, 3454–3457 (2000).
- [230] P. Politi, A. Rettori, F. Hartmann-Boutron, and J. Villain, *Tunneling in mesoscopic magnetic molecules*, Physical Review Letters **75**, 537–540 (1995).
- [231] T. Bilgeri, “Quantum dynamics in individual surface spins”, PhD thesis (EPFL, 2021).
- [232] G. Meyer, *Reduced halides of the rare-earth elements*, Chemical Reviews **88**, 93–107 (1988).
- [233] A. Delin, L. Fast, B. Johansson, J. M. Wills, and O. Eriksson, *Method for calculating valence stability in lanthanide systems*, Physical Review Letters **79**, 4637–4640 (1997).
- [234] M. J. Martinez-Pérez, S. Cardona-Serra, C. Schlegel, F. Moro, P. J. Alonso, H. Prima-García, J. M. Clemente-Juan, M. Evangelisti, A. Gaita-Ariño, J. Sesé, J. van Slageren, E. Coronado, and F. Luis, *Gd-based single-ion magnets with tunable magnetic anisotropy: molecular design of spin qubits*, Physical Review Letters **108**, 247213 (2012).
- [235] Y.-C. Chen, Y.-Y. Peng, J.-L. Liu, and M.-L. Tong, *Field-induced slow magnetic relaxation in a mononuclear Gd(III) complex*, Inorganic Chemical Communications **107**, 107449 (2019).
- [236] J. Mayans and A. Escuer, *Correlating the axial zero field splitting with the slow magnetic relaxation in Gd(III) SIMs*, Chemical Communications **57**, 721–724 (2021).
- [237] T. K. Ghosh, S. Maity, J. Mayans, and A. Ghosh, *Family of isomeric  $\text{Cu}^{\text{II}}\text{-Ln}^{\text{III}}$  ( $\text{Ln} = \text{Gd}$ ,  $\text{Tb}$ , and  $\text{Dy}$ ) complexes presenting field-induced slow relaxation of magnetization only for the members containing  $\text{Gd}^{\text{III}}$* , Inorganic Chemistry **60**, 438–448 (2021).
- [238] J. López-Cabrelles, L. Escalera-Moreno, Z. Hu, H. Prima-García, G. M. Espallargas, A. Gaita-Ariño, and E. Coronado, *Near isotropic  $D_{4d}$  spin qubits as nodes of a Gd(III)-based metal–organic framework*, Inorganic Chemistry **60**, 8575–8580 (2021).
- [239] M. Pivetta, F. Patthey, I. Di Marco, A. Subramonian, O. Eriksson, S. Rusponi, and H. Brune, *Measuring the intra-atomic exchange energy in rare-earth adatoms*, Physical Review X **10**, 031054 (2020).
- [240] G. Kresse and J. Hafner, *Ab initio molecular dynamics for liquid metals*, Physical Review B **47**, 558–561 (1993).
- [241] G. Kresse and D. Joubert, *From ultrasoft pseudopotentials to the projector augmented-wave method*, Physical Review B **59**, 1758–1775 (1999).
- [242] S. Grimme, J. Antony, S. Ehrlich, and H. Krieg, *A consistent and accurate ab initio parametrization of density functional dispersion correction (DFT-D) for the 94 elements H-Pu*, Journal of Chemical Physics **132**, 154104 (2010).
- [243] S. Grimme, S. Ehrlich, and L. Goerigk, *Effect of the damping function in dispersion corrected density functional theory*, Journal of Computational Chemistry **32**, 1456–1465 (2011).



- 
- [244] M. Dion, H. Rydberg, E. Schröder, D. C. Langreth, and B. I. Lundqvist, *Van der Waals density functional for general geometries*, Physical Review Letters **92**, 246401 (2004).
- [245] T. Thonhauser, V. R. Cooper, S. Li, A. Puzder, P. Hyldgaard, and D. C. Langreth, *Van der Waals density functional: self-consistent potential and the nature of the van der Waals bond*, Physical Review B **76**, 125112 (2007).
- [246] G. Román-Pérez and J. M. Soler, *Efficient implementation of a van der Waals density functional: application to double-wall carbon nanotubes*, Physical Review Letters **103**, 096102 (2009).
- [247] J. Klimeš, D. R. Bowler, and A. Michaelides, *Chemical accuracy for the van der Waals density functional*, Journal of Physics: Condensed Matter **22**, 022201 (2009).
- [248] J. Klimeš, D. R. Bowler, and A. Michaelides, *Van der Waals density functionals applied to solids*, Physical Review B **83**, 195131 (2011).
- [249] P. E. Blöchl, O. Jepsen, and O. K. Andersen, *Improved tetrahedron method for Brillouin-zone integrations*, Physical Review B **49**, 16223–16233 (1994).
- [250] H. J. Monkhorst and J. D. Pack, *Special points for Brillouin-zone integrations*, Physical Review B **13**, 5188–5192 (1976).
- [251] V. I. Anisimov, F. Aryasetiawan, and A. I. Lichtenstein, *First-principles calculations of the electronic structure and spectra of strongly correlated systems: the LDA+U method*, Journal of Physics: Condensed Matter **9**, 767–808 (1997).
- [252] S. L. Dudarev, G. A. Botton, S. Y. Savrasov, C. J. Humphreys, and A. P. Sutton, *Electron-energy-loss spectra and the structural stability of nickel oxide: an LSDA+U study*, Physical Review B **57**, 1505–1509 (1998).
- [253] A. J. Heinrich, J. A. Gupta, C. P. Lutz, and D. M. Eigler, *Single-atom spin-flip spectroscopy*, Science **306**, 466–469 (2004).
- [254] N. Lorente and J.-P. Gauyacq, *Efficient spin transitions in inelastic electron tunneling spectroscopy*, Physical Review Letters **103**, 176601 (2009).
- [255] F. D. Novaes, N. Lorente, and J.-P. Gauyacq, *Quenching of magnetic excitations in single adsorbates at surfaces: Mn on CuN/Cu(100)*, Physical Review B **82**, 155401 (2010).



# Sébastien Reynaud

Date of birth: 14.08.1992  
Nationality: Swiss  
Email: s-reynaud@hotmail.com

## EDUCATION

---

<b>EPFL</b> Doctoral assistant at the Laboratory of Nanostructures at Surfaces – Magnetism and metal-organic self-assembly of rare-earth atoms on decoupling layers	Lausanne, CH 2018–Present
<b>EPFL</b> M.S. physics – Minor in computational sciences	Lausanne, CH 2015–2018
<b>University of Nottingham</b> Third year abroad with the Swiss exchange program	Nottingham, UK 2014–2015
<b>EPFL</b> B. S. physics	Lausanne, CH 2012–2015
<b>Collège St-Michel</b> Maturité Gymnasiale	Fribourg, CH 2008–2012

## EXPERIENCE

---

<b>Teaching assistant</b> <i>Physics III-IV for physicists</i>	2015-2021
<b>Teaching assistant</b> <i>Physics I-II for physicists</i>	2015-2017
<b>Teaching assistant</b> <i>Physics I</i>	Autumn 2013
<b>Teaching assistant</b> <i>Physics II</i>	2016-2017

## SKILLS

---

- **Software:** Haskell, Mathematica, Matlab, Python, C++
- **Experimental:** UHV laboratory

## LANGUAGES

---

- **French:** Mother tongue
- **English:** Good knowledge
- **German:** Intermediate

## PROJECTS

---

- Master thesis:  
Self-assembly of  $3d-4f$  dimers on graphene
- Master project:  
On-the-fly ab initio semiclassical dynamics of floppy molecules: Resonance Raman spectra of ammonia  
Poster presentation at WATOC 2017, Munich
- Bachelor:  
Simulation of SQUID measurements with finite size samples